This is to certify that the
dissertation entitled

Model-Based Control of Electro-Pneumatic Intake and Exhaust Valve Actuators for IC Engines

presented by

Jia Ma

has been accepted towards fulfillment
of the requirements for the

Ph. D. degree in Mechanical Engineering

Harold J. Schock
Major Professor's Signature

January 21, 2008
Date

MODEL-BASED CONTROL OF ELECTRO-PNEUMATIC INTAKE AND EXHAUST VALVE ACTUATORS FOR IC ENGINES

By

Jia Ma

A DISSERTATION

Submitted to
Michigan State University
in partial fulfillment of the requirements
for the degree of

DOCTOR OF PHILOSOPHY

Department of Mechanical Engineering

2008

ABSTRACT

MODEL-BASED CONTROL OF ELECTRO-PNEUMATIC INTAKE AND EXHAUST VALVE ACTUATORS FOR IC ENGINES

By

Jia Ma

Variable valve actuation of Internal Combustion (IC) engines is capable of significantly improving their performance. Variable valve actuation can be divided into two main categories: variable valve timing with cam shaft(s) and camless valve actuation. For camless valve actuation, research has been centered in electro-magnetic, electro-hydraulic, and electro-pneumatic valve actuators. This research addresses the detailed modeling and control of a novel electronically controlled, pneumatic-hydraulic valve actuator (EPVA) for both the intake and exhaust valves of an IC engine. The valve actuator's main function is to provide variable valve timing, lift and duration of the intake and exhaust valves of an IC engine. A system dynamics analysis is provided and followed by a mathematical model. This modeling approach uses Newton's law, mass conservation and thermodynamic principles. A control oriented model was developed to reduce computational throughput for real-time model-based control implementation. Simulated model responses were found to be in satisfactory agreement with experimental results. For intake valves, an on-line model reference adaptive system identification technique was employed to estimate system parameters required for closed-loop adaptive control; and an adaptive valve lift control strategy was developed to reduce both transient and steady-state lift tracking error. Unlike the intake valves, the exhaust valve opens against an in-cylinder pressure that is a function of the engine operational conditions with cycle-to-cycle combustion variations. This pressure disturbance slows down the valve actuator response and increases the variation of valve lift and opening delay. The developed control strategy utilizes model based predictive tech-

niques to overcome the randomly varying in-cylinder pressure against which the exhaust valve opens. Both intake and exhaust valve control strategies were performed on a Ford 5.4 liter 3-valve V8 engine head at different operating conditions. Experimental results were used to validate the control strategies.

To My Parents

ACKNOWLEDGMENTS

First, I thank my advisor Dr. Harold Schock for his continuous support of the Ph.D. program. Dr. Schock was always there to listen and to give advices. Four years ago, he had the foresight to initiate the actuator control project, a topic of great importance today. He provided me great opportunities to work independently and to meet my ever expanding experimental equipment requirements as well as to collaborate with a well trained and intelligent team. He taught me how to express my ideas and gave me plenty of room to experiment on them. He always had confidence in me even when I was frustrated. He showed me the need to be persistent to reach any goal. His efforts made the Automotive Research Experiment Station (ARES) at Michigan State University my wonderful research home for the past three and a half years.

Special thanks go to my co-advisor, Dr. Guoming Zhu, who is most responsible for helping me complete the writing of this dissertation as well as the challenging research that lies behind it. Dr. Zhu has been a friend and mentor. He taught me how to write academic papers and how to approach research problems in different ways. He brought out the good ideas in me and made me a better engineering researcher. He showed tremendous patience in helping building and debugging the control system hardware. He was always there to meet and discuss my ideas, to proofread and markup my papers and chapters, and to ask me challenging questions to help me think through my problems. Without his encouragement and constant guidance, I could not have finished this dissertation.

I also thank the research associates and graduate students at ARES, MSU for their generous help to my work whenever it was needed. Thanks to Tom Stuecken for bright ideas and suggestions regarding how to modify the mechanical experimental setups, as well as machining and installing the mechanical system. Thanks to Andy Fedewa and Joshua Bedford for participating in a number of important discussions and assisting me in the experiments. Thanks to Mulyanto Poort for the aid in the C programming and Andrew Hartsig for performing the WAVETM simulation of the engine. Thanks to David Hung

with Visteon Cooperation for his extensive contribution to this project and wholehearted support to my career. Their support and effort made it viable for me to complete this work. Let me also say 'thank you' to Edward Timm, Andreas Petrou Panayi, Kimberly Sarbo and Melissa Jopke at ARES for being delightful colleagues who made the work environment more pleasant and fun.

Besides my advisors and co-workers, I would like to thank the rest of my thesis committee: Dr. Ranjan Mukherjee, Dr. Brian Feeney and Dr. Hassan Khalil who asked me good questions, gave insightful comments, reviewed my work and accommodated on the defense time on a short notice. My additional appreciation goes to Dr. Feeney who believed in me and supported me through the good and bad times in my Ph.D. program.

During the course of this research work at ARES, MSU (2004 - 2007), I was supported by the U.S. Department of Energy, National Energy Technology Laboratory, Energy Efficiency and Renewable Energy Division. I want to express my gratitude toward them for sponsoring the project and to Samuel Taylor, the project manager, for his project management and encouragement.

Last, but not least, I thank my mother, Rongzhu Gu, and father, Yiwei Ma, for giving me life in the first place, for educating me with aspects from both arts and sciences, for unconditional support and encouragement to pursue my career interests, even when the interests went beyond boundaries of language, field and geography, and for everlasting faith in me.

TABLE OF CONTENTS

LIST OF TABLES

LIST OF FIGURES

CHAPTER 1

Introduction

1.1 Motivation and Literature Review

In a camless valvetrain of an internal combustion (IC) engine, the motion of each valve is controlled by an independent actuator. There is no camshaft or other mechanisms coupling the valve motion to the crankshaft, contradicted to a conventional valvetrain. This makes it possible to control the valve events, i.e. timing, lift and duration, independent of crankshaft position. Various studies have shown that an engine equipped with variable valve actuation (VVA) allows the reduction of IC engine pumping losses, deactivation of selected cylinder(s), flame speed regulation by manipulating in-cylinder turbulence, and control of the internal residual gas recirculation (RGR) and NOx emissions.. These benefits contribute to a considerable potential engine performance improvement, fuel economy improvement and emission reduction . J.W.G.Turner et al. studied the strategies of camless valvetrain implementation [8]. Research has been conducted on different types of valve actuators, including electromagnetic, hydraulic and pneumatic actuators. Chihaya Sugimotoet et al. [1], Mark A.Theobald et al. [11] and F.Pischinger et al. [4] developed electromagnetic actuators. H.P.Lenz et al. [6] developed a hydraulic actuator. W.E.Richeson et al. presented a pneumatic actuator incorporated with a permanent magnet control latch in [17]. The advantages and disadvantages of a pneumatic actuator over a hydraulic actuator were ad-

dressed by John P.Watson and Russell J.Wakeman [14]. In their article, a pneumatic valve actuator with a physical motion stopper was presented and the simulations of the valve actuation system were shown. In [3], James E.Bobrow and Brian W.McDonell modeled a variable valve timing engine and discussed an engine control strategy. In order to provide an insight into the pneumatic actuator design and the control requirements, mathematical modeling was developed for a variety of actuation systems. In [7], J.M.Tressler et al. analyzed and modeled the dynamics of a pneumatic system consisting of a double-acting or single-acting cylinder and servovalve. A mathematical model of a pneumatic force actuator was presented by Edmond Richer and Yildirim Hurmuzlu in [16].

A significant amount of research has been conducted to demonstrate the advantage of variable valve actuation over the traditional cam-based valve-train of both gasoline and diesel engines. The investigation of intake valve timing control of a Spark Ignited (SI) engine was conducted in [5]. It was found that at low and partial load conditions, engine pumping loss was reduced between 20% and 80% due to throttless operation. Fuel consumption was improved up to 10% at idle. Through simulation and experiments, reference [13] shows that SI engine efficiency can be improved up to 29% due to Variable Valve Timing (VVT), compared to a classic (throttled) engine. The engine torque output is also improved by up to 8% at low speed with wide open throttle. Research carried out in [10] demonstrates how VVT and VVL (Variable Valve Lift) affect the partial load fuel economy of a light-duty diesel engine. In this study, the indicated and brake-specific fuel consumptions were improved up to 6% and 19% respectively. The operation of an Otto-Atkinson cycle engine by late intake valve closing to have a larger expansion ratio than compression ratio was studied in [2]. A significant improvement of CO and NOx was obtained. Reference [18] also shows that the operational range of a Homogeneously Charged Compression Ignition (HCCI) engine can be expanded to operate at both high and low load through the adoption of VVT and VVL. The advantages of VVT and VVL engines lead to the development of engine optimization over its operational range. For example, reference [12] presented the VVT and VVL optimization methodology for an I4 2.0L camless ZETEC engine at

various operational conditions including cold starts, cylinder deactivation, full load, idle and transient operations.

Electronically controlled pneumatic/hydraulic valve actuators (EPVA) can be used to replace the traditional camshaft in an internal combustion engine. The EPVA is capable of varying valve lift height, valve timing and valve open duration as desired in a variable valve timing engine. In addition, the EPVA is designed to extract the maximum work from the air flow by incorporating a hydraulic latch mechanism to reduce the power consumption. A hydraulic damper mechanism is also added to produce a desirable slow and smooth seating velocity when the valve returns to the seat. This research is targeted to develop closed loop control strategies for both EMVA intake and exhaust valves to accurately regulate valve opening timing, lift and duration. For intake valves, an adaptive feedforward control scheme is developed to improve steady state and transient response performance; and for exhaust valves, model based predictive feedforward control strategy is employed to compensate the cycle-to-cycle varying in-cylinder pressure disturbance. Both control strategies were validated on the EPVA test bench using a Ford 3 valve 5.4 L V8 engine head.

1.2 Scope of Work and Content of Thesis

The thesis is organized as follows. In chapter 2, mathematical models were developed to better understand the valve dynamics and to be used for control strategy development. A system dynamics analysis is provided in Section I followed by a mathematical model in Section II. This modeling approach uses the Newton's law, mass conservation and thermodynamic principles. The air compressibility and liquid compressibility in the hydraulic latch are modeled. The discontinuous nonlinearity of the compressible flow due to choking is carefully considered. Provision is made for the nonlinear motion of the mechanical components due to the physical constraints. Validation experiments were performed on a Ford 5.4 liter 4-valve V8 engine head with different air supply pressures and different solenoid pulse inputs. Experimental results are presented in Section III. The chapter ends with a

few conclusions.

Chapter 3 proposed an adaptive valve lift and timing control schemes for an electro-pneumatic valve actuator (EPVA) to improve both transient and steady state response performances. A control oriented electro-pneumatic valve model was developed in section I. An adaptive parameter identification scheme was developed based upon this model to construct a feedforward control in the next section. A PI (Proportional and Integral) closed-loop control strategy of valve lift and timing tracking was integrated with the feedforward control based upon the adaptive parameter identification. In Section III, the control algorithms were implemented in a prototype controller on an EPVA valve test bench using a 5.4 liter 3-valve V8 engine head. The adaptive parameter identification convergence was demonstrated during the EPVA bench tests and the closed-loop lift control algorithm was also evaluated by simulations. In Section IV, the detailed closed-loop intake valve lift, opening timing and closing timing control schemes were addressed. The conclusions were presented in Section V.

Unlike the intake valve, the exhaust valve opens against an in-cylinder pressure that varies as a function of the engine operational conditions with cycle-to-cycle combustion variations. This pressure disturbance slows down the valve actuator response and as a result, it increases the variation of valve opening delay. In fact, this disturbance makes it difficult to maintain repeatable valve opening timing and lift. As a result, unrepeatable valve lift affects the closing timing control which is critical for RGR control. Therefore, addresses the exhaust valve lift control strategies in a way different from that of intake valve. In chpter 4, the level two dynamic model of the exhaust valve, along with the in-cylinder pressure model, is reviewed in Section I. The feedforward and closed-loop control strategies are discussed in Section II where a model-based predictive control technique was used to estimate the solenoid actuation timing for a desired valve lift. This estimation is used as a feedforward control, along with a PI closed loop control, to improve the exhaust valve lift repeatability. Then, the simulation validation results of the closed-loop exhaust valve lift control are shown in Section III. The real time exhaust valve lift control algorithm

is depicted in Section IV, followed by the conclusions in section V.

The valve model, intake and exhaust valve control strategies were developed from chapter 2 to 4. In chapter 5, the developed closed-loop intake and exhaust lift control systems are validated with experiments. Section I describes the EPVA experimental setup including both the mechanical system and the modular control system hardware configurations. Section II shows the real-time control results, along with data analysis for the lift and timing control of intake valves with concluding remarks. Finally, Section III presents the closed loop control test results for the exhaust valve lift control with concluding remarks. Images in this dissertation are presented in color.

CHAPTER 2

Mathematical Modeling

2.1 Introduction

In this chapter, a physics oriented nonlinear mathematical model of the electro-pneumatic valve actuator. It provides an insight to the mechanical system and help to develop control cetraria.

2.2 System Dynamics

The EPVA consists of two solenoids, two spool valves, two port valves, an actuator piston, an actuator cylinder and a hydraulic latch/damper system. An actuator piston pushes the back of the poppet valve stem, causing the valve to open. Solenoid-controlled spool valves are used to control the flow of the air that enters and exits the actuator cylinder. In order to reduce the energy consumption, EPVA uses a hydraulic latch which allows the actuator to extract the full expansion work out of the air that is drawn into the actuator cylinder. Meanwhile, the actuator is still capable of holding the valve in an open position to obtain full variation of valve open duration. A hydraulic damping mechanism is added to provide a slow seating velocity for the valve. According to the events taking place in the actuator cylinder, the system dynamics are divided into three stages: air charging, expansion and dwell, and air discharging stage. Figure 2.6 illustrates their equivalent stages on the valve

lift profile.

2.2.1 Air Charging Stage

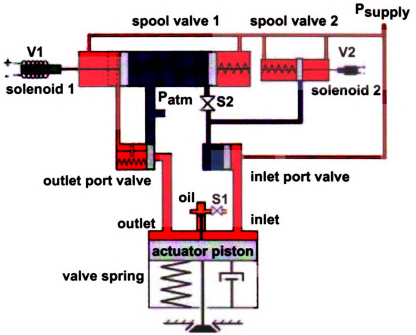

Figure 2.1. System dynamics at the air charging stage

Figure 2.1 depicts the system dynamics when the actuator cylinder is at the air charging stage. The red color represents the high pressure (supply pressure) air, the blue color represents the low pressure (atmospheric pressure) air, the yellow color represents the oil in the hydraulic latch/damper. $S1$ and $S2$ are two check valves that are corresponding to solenoid 1 and solenoid 2. When a solenoid is energized, its corresponding check valve is able to function as a one-way flow valve. When that solenoid is deactivated, then the check valve is held off its seat allowing two way flow. Green is an energized solenoid while blue is an de-energized solenoid.

During the charging stage, solenoid 1 is energized pushing the spool valve 1 slightly to the right. In this spool valve position, the high pressure air is sent to two places, the

left of the outlet port valve and the right of the inlet port valve. The low pressure air is sent to the left of the inlet port valve. Therefore, the high pressure air closes the outlet port valve and opens the inlet port valve. The supply air now charges the cylinder, the actuator piston starts moving down and opens the poppet valve. Although the right side of the outlet port valve is then subject to high pressure air, it remains closed due to the area difference between the two sides of the port valve. The check valve $S1$ is activated at the moment when solenoid 1 is energized. This only allows the oil to flow down the passage and prevents it from returning to the reservoir. The oil supply pressure is the same as the air supply pressure.

2.2.2 Expansion and Dwell Stage

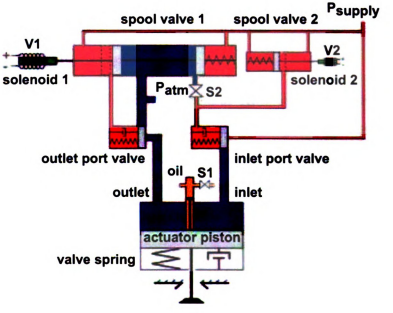

Figure 2.2. System dynamics at the expansion and dwell stage

In the expansion and dwell stage as shown in Figure 2.2, solenoid 2 is energized as well. The time delay between the activation of two solenoids is usually chosen from $2ms$ to $5ms$ depending on the desired valve lift height. The spool valve 2 is pushed slightly

to the left so that the high pressure air can be sent to the left of the inlet port valve through the second spool valve. The check valve $S2$ is activated at the same time when solenoid 2 is energized to prevent the high pressure air from escaping to the atmosphere through the first spool valve. The inlet port valve is closed due to its area difference at two sides. Meanwhile, solenoid 1 remains energized, therefore, the outlet port valve remains closed. The air that was drawn into the actuator cylinder during the previous (air charging) stage is able to expand completely. The actuator piston and poppet valve both reach their maximum displacement. The high pressure oil (yellow color) trapped in the hydraulic latch (check valve $S1$ is still on) balances the valve spring force and keeps the poppet valve open at its maximum lift height as long as it is needed. This is also called energy saving mode. It allows the system to extract the full expansion work from the air which has entered the cylinder without losing the capability to vary the valve open duration.

2.2.3 Air Discharging Stage

In the air discharging stage, the air leaves the actuator cylinder and the valve returns to its seat. As displayed in Figure 2.3, both solenoids are de-energized. Consequently, both check valves, $S1$ and $S2$, are de-activated. The air flow and the oil flow can travel in two directions. Since both solenoids are off, the springs inside the two spool valves can return the spools to their original positions. The high pressure air is then sent to both sides of the inlet port valve. The area difference between two sides of this port valve causes it to remain closed. Meanwhile, the low pressure air is on both sides of the outlet port valve. Because the oil in the hydraulic latch is now able to flow back up to its reservoir, there is no resistance for the valve spring to return the actuator piston. The actuator piston comes back and the volume of the air in the actuator cylinder is then reduced. This results in an increase of the air pressure in the actuator cylinder and an increase of the air pressure at the right side of the outlet port valve. Therefore, the outlet port valve is pushed open, the air in the actuator cylinder is able to discharge and its pressure decreases immediately. The poppet valve now returns to the seat. The hydraulic damper starts to function when

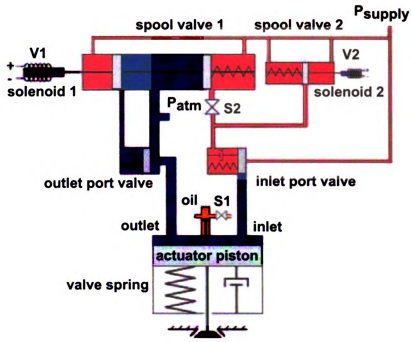

Figure 2.3. System dynamics at the air discharging stage

the poppet valve moves close to its seat. Due to the decreasing flow area where the oil leaves the passage, the velocity of the valve is reduced greatly to provide a smooth return.

2.3 Mathematical Modeling

The purpose of this section is to derive governing equations of the individual components of the pneumatic/hydraulic valve actuator, which consists of the actuator piston, the hydraulic latch/damper, the inlet and outlet port valves, two solenoids and two spool valves as displayed in Figure 2.1. These equations were used to simulate the behavior of the valve under different sets of operating conditions.

2.3.1 Actuator Piston

In this section, energy conservation, mass conservation and Newton's second law were used to determine the following variables: the rate change of the gas pressure inside of the cylinder chamber $\dot{P}_p$, the rate change of density of the gas $\dot{\rho}_p$ and the acceleration of the actuator piston $\ddot{y}$. A sudden reduction in pressure occurs at the inlet port when it opens. This causes the air flow to expand in an explosive fashion. The flow is choked and the pressure at the port stays constant. The difference between the cylinder pressure and the supply pressure decreases as the pressure in the cylinder chamber builds up over time. The air then becomes unchoked and flows through the inlet with decreasing pressure. The flow exiting the outlet switches between a choked and unchoked pattern as well for the same reason. This discontinuous nonlinearity of the flow has to be taken into consideration in the actuator piston model. As shown in Figure 2.4, considering the control volume above the actuator piston in the cylinder chamber including the inlet and outlet, the first law of thermodynamics can be written as:

$$\dot{Q} - \dot{W} + \dot{m}_i(h_i + \frac{v_i^2}{2}) - \dot{m}_e(h_e + \frac{v_e^2}{2}) = \frac{\partial E}{\partial t} \tag{2.1}$$

where,

- $\dot{Q}$ is the heat transfer rate into the control volume
- $\dot{W}$ is the work rate delivered by the control volume to the actuator piston
- $\dot{m}_i$ is the mass flow rate entering the control volume
- $\dot{m}_e$ is the mass flow rate exiting the control volume
- $\dot{h}_i$ is the enthalpy of the gas entering the cylinder chamber
- $\dot{h}_e$ is the enthalpy of the gas exiting the cylinder chamber
- $\frac{\partial E}{\partial t}$ is the rate of change of the total energy of the control volume.

- Evaluation of $\dot{W}$

The rate of the work done on the actuator piston by the control volume is:

$$\dot{W} = A_p P_p \dot{y} \tag{2.2}$$

where, A_p is the area of the actuator piston, P_p is the pressure of the control volume (the pressure on the actuator piston) and $\dot{y}$ is the velocity of the actuator piston movement.

- Evaluation of $h_i + \frac{v_i^2}{2}$ and $h_e + \frac{v_e^2}{2}$

The supply air entering the cylinder chamber from the inlet can be viewed as a gas coming from a reservoir. The gas in the reservoir has zero velocity, therefore, its enthalpy is stagnation enthalpy of the inlet supply air h_{in}. For the same reason, the air leaving the cylinder chamber from the outlet can be viewed as a gas leaving a reservoir, which is the control volume inside the chamber. Hence, the enthalpy of the air leaving the chamber can be represented by the stagnation enthalpy of the air in the actuator cylinder h_p.

$$h_i + \frac{v_i^2}{2} = h_{in} = C_p T_{in} \tag{2.3}$$

$$h_e + \frac{v_e^2}{2} = h_p = C_p T_p \tag{2.4}$$

Treating air as an ideal gas, we have:

$$P = \rho R T \tag{2.5}$$

Replacing T_p in Equation (2.4) with $\frac{P_p}{R\rho_p}$:

$$h_e + \frac{v_e^2}{2} = \frac{C_p P_p}{R\rho_p} \tag{2.6}$$

where,

- T_{in} is the temperature of the air at the inlet which equals to the ambient temperature $T_{atm} = 295K$
- C_p is the specific heat of the air at constant pressure
- R is the gas constant of the air

- ρ_p is the density of the air in the cylinder chamber above the actuator piston

- P_p is the pressure of the air in the cylinder chamber above the actuator piston

- T_p is the temperature of the air in the cylinder chamber above the actuator piston

- Evaluation of $\dot{m}_i$ and $\dot{m}_e$

In order to draw the equations for the mass flow rate when the air flow enters the inlet or leaves the outlet, we need to consider two cases, choked and unchoked gas flow. The proof of the derivation of the mass flow equation is shown by J. M. Tressler et al. in [7]. We assume that the gas flow in the valve actuator is adiabatic ($\dot{Q} = 0$) for now, and a term proportional to $\dot{W}$ will be subtracted from the total power that is delivered to the actuator piston to compensate the heat loss [16]. We also assume that the flow is isentropic everywhere except across normal shock waves.

Considering the mass flow rate $\dot{m}_i$ at the inlet, the flow patten depends on the cylinder pressure P_p and the supply pressure P_{supply} as follows:

$$\dot{m}_i = \gamma_{in}\sqrt{\frac{k}{RT_{in}}}P_{supply}A_{in} \tag{2.7}$$

If $P_p > 0.53P_{supply}$, the unchoked case:

$$\gamma_{in} = \sqrt{\frac{2}{k-1}}\left(\frac{P_p}{P_{supply}}\right)^{\frac{k+1}{2k}}\left[\left(\frac{P_p}{P_{supply}}\right)^{\frac{1-k}{k}} - 1\right]^{\frac{1}{2}} \tag{2.8}$$

If $P_p \leq 0.53P_{supply}$, the choked case:

$$\gamma_{in} = 0.58 \tag{2.9}$$

where, $k = \frac{C_p}{C_v}$ is the specific heat ratio, C_v is the specific heat of air at constant volume. A_{in} is the area of the inlet. Since the port valves open and close very fast, the effective flow area A_{in} can be approximated as:

$$A_{in} = \pi r_1^2, w > 0 \tag{2.10}$$

$$A_{in} = 0, w = 0 \tag{2.11}$$

where, r_1 is the inner radius of the inlet port valve. We can derive the mass flow rate $\dot{m}_e$ equation similarly as follows:

$$\dot{m}_e = \gamma_{out}\sqrt{\frac{k}{RT_p}}P_p A_{out} \tag{2.12}$$

If $P_{out} > 0.53P_p$, the unchoked case:

$$\gamma_{out} = \sqrt{\frac{2}{k-1}}\left(\frac{P_{out}}{P_p}\right)^{\frac{k+1}{2k}}\left[\left(\frac{P_{out}}{P_p}\right)^{\frac{1-k}{k}} - 1\right]^{\frac{1}{2}} \tag{2.13}$$

If $P_{out} \leq 0.53P_p$, the choked case:

$$\gamma_{out} = 0.58 \tag{2.14}$$

where, A_{out} is the area of the outlet, it follows the same expression as A_{in} except that it is dependent on z. The A_{out} expression can be given as below:

$$A_{out} = \pi r_1^2, z > 0 \tag{2.15}$$

$$A_{out} = 0, z = 0 \tag{2.16}$$

where, r_1 is the outer radius of the outlet port valve.

- Evaluation of $\frac{\partial E}{\partial t}$

The rate of change of the total energy of the control volume is the summation of the rate of change of the internal energy, the kinetic energy and the potential energy. The kinetic and potential energy of the control volume are negligible. Hence, the change of the total energy is approximated as the rate of change of the internal energy:

$$\frac{\partial E}{\partial t} = \frac{\partial U}{\partial t} = \frac{d}{dt}(mC_v T_p) \tag{2.17}$$

m is the mass of air in the control volume and C_v is the specific heat of air at constant volume. The expression for $\dot{m}$ is:

$$\dot{m} = \rho_p A_p \dot{y} \tag{2.18}$$

Expanding Equation (2.17), and using Equation (2.18) and Equation (2.5) results in:

$$\frac{\partial E}{\partial t} = \frac{A_p C_v}{R}(P_p \dot{y} + \dot{P}_p y) \tag{2.19}$$

The expression for $\dot{P}_p$ can be derived by substituting Equation (2.2), (2.3), (2.6), (2.7), (2.12) and (2.19) into Equation (2.1):

$$\dot{P}_p = \frac{1}{A_p y}[C_{din} A_{in}(w) P_{supply} \gamma_{in} \sqrt{k^3 R T_{in}} \\ -C_{dout} A_{out}(z) \gamma_{out} \sqrt{\frac{k^3 P_p^3}{\rho_p}}] - \alpha_p k \frac{P_p \dot{y}}{y} \tag{2.20}$$

where, C_{din} and C_{dout} are the flow discharge coefficients at the inlet and outlet. α_p is multiplied by the rate change of work $\dot{W}$ because it is assumed that part of the work is dissipated as heat loss from the system. α_p is chosen to be between 0 to 1 depending on the actual heat loss during the process. This formulation is studied by Edmond Richer and Yildirim Hurmuzlu in [16].

Applying the law of mass conservation to the control volume above the actuator piston in the cylinder results in:

$$\dot{m}_i - \dot{m}_e = A_p(\rho_p \dot{y} + \dot{\rho}_p y) \tag{2.21}$$

Replacing $\dot{m}_i$ and $\dot{m}_e$ by Equation (2.7) and (2.12) to obtain the expression for $\dot{\rho}_p$:

$$\dot{\rho}_p = \frac{1}{A_p y}[C_{din} A_{in}(w) \gamma_{in} P_{supply} \sqrt{\frac{k}{R T_{in}}} \\ -C_{dout} A_{out}(z) \gamma_{out} \sqrt{k P_p \rho_p}] - \frac{\rho_p \dot{y}}{y} \tag{2.22}$$

Now we invoke Newton's second law to obtain the $\ddot{y}$ equation:

$$M\ddot{y} + C_f \dot{y} + K_p(y + \delta_p) = A_p P_p + A_{cap} P_{oil} \\ -(A_p + A_{cap}) P_{atm} \tag{2.23}$$

$$M = M_{piston} + M_{valve} + \frac{1}{3} M_{spring} + M_{cap}$$

where,

- M_{piston} is the mass of the actuator piston

- M_{valve} is the mass of the intake valve

- M_{spring} is the mass of the valve spring. The effective spring mass equals one third of the total spring mass [15]

- M_{cap} is the mass of the cap on the top of the valve stem

- A_{cap} is the area of the cap on the top of the actuator piston stem

- $A_p = \pi r_p^2 - \pi r_{oil}^2$ with r_p as the radius of the actuator piston and r_{oil} as the radius of the oil passage

- C_f is the damping coefficient approximating the energy dissipation due to the friction

- K_p is the stiffness of the valve spring

- δ_p is the preload of the valve spring

Rearranging Equation (2.23):

$$\ddot{y} = \frac{1}{M}[A_p P_p + A_{oil} P_{oil} - (A_p + A_{oil}) P_{atm} - C_f \dot{y} - K_p(y + \delta_p)] \tag{2.24}$$

2.3.2 Hydraulic Latch/Damper

Another mechanism that has a direct impact on the dynamics of the actuator piston is the hydraulic latch/damper. The compressibility of the fluid in the hydraulic latch is considered and the mechanism of adjusting the valve seating velocity is modeled in detail. Figure 2.5)illustrates this function. The oil sits on the top of the actuator piston stem with the supply pressure as the back pressure. Fluid enters or exits through area A_{oilin}/A_{oilout}. When the air that is drawn in at the air charging stage is fully expanded in the actuator cylinder, the actuator piston reaches to its maximum displacement. The check valve $S1$ is activated by solenoid 1 to prevent the oil from returning. (Recall system dynamics at the air charging stage, and expansion and dwell stage.) The pressurized oil is trapped in

the passage and keeps the actuator piston at the maximum displacement until solenoid 1 is turned off. (Recall the air discharging stage). Hence, this hydraulic latch provides an adjustable valve open duration. Another function of this mechanism is to provide a low seating velocity for the valve. When the actuator piston approaches the original position, the cap on the top of the stem will partially block the exit area A. The actuator piston encounters a large resistant force due to the reduced flow area, which decreases the velocity tremendously. The smaller the area A, the lower the valve velocity.

Figure 2.6shows a valve lift profile with the solenoid action chart. The solenoid itself has about $2ms$ to $3ms$ delay upon activation. These delays were not shown in this chart. As was explained earlier, one valve cycle consists of three stages: air charging, expansion and dwell, and air discharging stage. They will be called stage I, stage II and stage III in this section. Solenoid 1 is on at the beginning of stage I and off at the end of stage II. Solenoid 2 turns on before stage II. Solenoid 2 runs on the same frequency and the same duty cycle as solenoid 1 with a time delay. Both inlet and outlet are closed during the overlap of solenoid 1 and 2. The oil is modeled as an incompressible flow at stage I and III, while in stage II it is modeled as a compressible flow under high pressure with high incompressibility. The slight compressibility is what causes the volume change in the oil passage, hence the swing on the top of the valve lift profile.

- Stage I Air Charging (Incompressible Flow Model)

$$q_{oil} = C_{d_{oilin}} A_{oilin} \sqrt{\frac{P_{supply} - P_{oil}}{\rho_{oil}}} = A_{cap}\dot{y} \tag{2.25}$$

Therefore, the pressure of the oil at air charging stage is:

$$P_{oil} = P_{supply} - (\frac{A_{cap}\dot{y}}{C_{d_{oilin}} A_{oilin}})^2 \rho_{oil} \tag{2.26}$$

where,

- q_{oil} is the volumetric flow rate of the fluid

- $C_{d_{oilin}}$ is the discharge coefficient as the fluid enters the passage

- A_{oilin} is the area where the fluid enters the passage (it is calculated later)

- P_{supply} is the air supply pressure

- P_{oil} is the oil pressure and is at the same pressure as air supply

- ρ_{oil} is the density of the fluid

• Stage II Expansion and Dwell (Compressible Flow Model)

The state equation $PV^c = K = constant$ is used here by choosing c very large to represent the high level of incompressibility.

$$P_{oillock}V^c = P_iV_i^c \tag{2.27}$$

Substituting $V = A_{cap}y$ and $V_i = A_{cap}y_i$ into Equation (2.27) to obtain:

$$P_{oillock} = \frac{P_iy_i^c}{y^c} \tag{2.28}$$

Where,

- $P_{oillock}$ is the pressure of the oil at the dwell (lock) stage

- y_i is the maximum valve displacement

- V_i is the volume of the fluid at the maximum valve displacement y_i

- P_i is the oil pressure P_{oil} at the peak valve lift height y_i

• Stage III Air Discharging (Incompressible Flow Model)

Similarly, the equation of motion for stage III was obtained as follows:

$$q_{oil} = C_{d_{oilout}}A_{oilout}\sqrt{\frac{P_{oil} - P_{supply}}{\rho_{oil}}} = A_{cap}\dot{y} \tag{2.29}$$

Rearrange Equation (2.29):

$$P_{oil} = P_{supply} + (\frac{A_{cap}\dot{y}}{C_{d_{oilout}}A_{oilout}})^2\rho_{oil} \tag{2.30}$$

where,

- $C_{d_{oilout}}$ is the discharge coefficient as the fluid exits the passage

- A_{oilout} is the area where the fluid exits the passage A_{oilin}=A_{oilout}=A

Evaluation of A:

$$A = 2\pi r_{pass}^2 + (A_{oil} - A_{cap}), y \leq p_1 \tag{2.31}$$

$$A = 2\pi(\frac{y}{2})^2 + (A_{oil} - A_{cap}), y < p_1 \tag{2.32}$$

The variables r_{pass}, A_{oil}, A_{cap} and p_1 are shown in Figure 2.5. The seating velocity is largely reduced while the stem enters the area where $y < p_1$. By adjusting p_1, we can alter its timing of entering the region where $y < p_1$ and consequently the slope of the response.

2.3.3 Inlet Port Valve

As illustrated in Figure 2.7) the inlet port valve is modeled as a mass-spring-damper system driven by the air flow from the spool valve with pressure P_{cupR} and the supply with pressure P_{supply}. P_{cupR} alternates between atmosphere and supply pressure which is regulated by the spool valve. Due to the difference between the areas on which P_{cupR} and P_{supply} act, the port valve remains closed when P_{cupR} equals P_{supply} and the supply air pushes it open when P_{cupR} reaches atmosphere pressure. The supply air is treated as a stagnant flow with constant pressure. We obtain the equation of motion by Newton's second law as below:

$$\begin{gathered} m_{cR}\ddot{w} + C_{cR}\dot{w} + K_{cR}w = P_{supply}A_{inlet} - P_{cupR}A_{cR} \\ 0 \leq w \leq w_{max}, A_{inlet} = \pi r_2^2 - \pi r_1^2, A_{cR} = \pi r_2^2 \end{gathered} \tag{2.33}$$

- m_{cR} is the mass of the inlet port valve

- C_{cR} is the damping coefficient compensating for the friction loss of the valve

- K_{cR} is the spring constant

- w, $\dot{w}$, $\ddot{w}$ are the displacement, velocity and the acceleration of the inlet port valve

- w_{max} is the maximum distance which the inlet port valve is allowed to travel. The discontinuous nonlinearity in the port valve dynamics caused by this physical limitation was considered.

- r_2 is the outer radius of the inlet and outlet port valve (see Figure 2.4)).

Rearranging Equation (2.33) to obtain expression for $\ddot{w}$:

$$\ddot{w} = \frac{1}{m_{cR}}(A_{inlet}P_{supply} - P_{cupR}A_{cR} - C_{cR}\dot{w} - K_{cR}w) \tag{2.34}$$

2.3.4 Outlet Port Valve

The outlet port valve functions in a similar way as the inlet port valve, except that the air that pushes the port valve open has the actuator cylinder pressure. The pressure in the actuator cylinder is unsteady, thus, the flow dynamics were modeled. The modeling process is similar to the actuator piston. The control volume used here is shown in Figure 2.8. Applying conservation of energy as shown in Equation (2.1), we evaluate $\dot{W}$, $\frac{\partial E}{\partial t}$, $h_i + \frac{v_i^2}{2}$ $h_e + \frac{v_e^2}{2}$ $\dot{m}_i$ and $\dot{m}_e$ as follows:

$$\dot{W} = A_{cL}P_{out}\dot{z} \tag{2.35}$$

$$A_{cL} = \pi r_2^2$$

where, P_{out} is the pressure on the outlet port valve in the control volume.

$$\frac{\partial E}{\partial t} = \frac{\partial U}{\partial t} = \frac{d}{dt}(mC_vT_{out}) = \frac{A_{cL}C_v}{R}(P_{out}\dot{y} + \dot{P_{out}}y) \tag{2.36}$$

where z is the displacement of the outlet port valve, T_{out} is the gas temperature in the control volume and P_{out} is the gas pressure in the control volume. The ideal gas law, Equation (2.5), was used to derive Equation (2.36). Treating the air flow from the actuator cylinder and the ambient air as stagnant flow we have:

$$h_i + \frac{v_i^2}{2} = h_p = C_pT_p = \frac{C_pP_p}{\rho_pR} \tag{2.37}$$

$$h_e + \frac{v_e^2}{2} = h_{atm} = C_p T_{atm} \tag{2.38}$$

$$\dot{m}_i = \gamma_{inL}\sqrt{\frac{k}{RT_p}} P_p A_{out} = A_{out}\gamma_{inL}\sqrt{k\rho_p P_p} \tag{2.39}$$

where A_{out} is the inlet area of the control volume. As it is drawn in Equation (2.15) and Equation (2.16), A_{out} can be approximated as:

$$A_{out} = \pi r_1^2, z > 0 \tag{2.40}$$

$$A_{out} = 0, z = 0 \tag{2.41}$$

If $P_{out} > 0.53P_p$, the unchoked case:

$$\gamma_{inL} = \sqrt{\frac{2}{k-1}}\left(\frac{P_{out}}{P_p}\right)^{\frac{k+1}{2k}}\left[\left(\frac{P_{out}}{P_p}\right)^{\frac{1-k}{k}} - 1\right]^{\frac{1}{2}} \tag{2.42}$$

If $P_{out} \leq 0.53P_p$, the choked case:

$$\gamma_{inL} = 0.58 \tag{2.43}$$

$$\dot{m}_e = \gamma_{outL}\sqrt{\frac{k}{RT_{out}}} P_{out} A_L = A_L \gamma_{outL}\sqrt{k\rho_{out} P_{out}} \tag{2.44}$$

where,

- T_{out} is the temperature of the gas in the control volume
- P_{out} is the is the pressure of the air in the
- ρ_{out} is the density of the air in the control volume

and A_L is the outlet area of the control volume and is also a function of geometry and the displacement of the outlet port valve.

$$A_L = 2\pi r_1 z \tag{2.45}$$

If $P_{atm} > 0.53P_{out}$, the unchoked case:

$$\gamma_{outL} = \sqrt{\frac{2}{k-1}}\left(\frac{P_{atm}}{P_{out}}\right)^{\frac{k+1}{2k}}\left[\left(\frac{P_{atm}}{P_{out}}\right)^{\frac{1-k}{k}} - 1\right]^{\frac{1}{2}} \tag{2.46}$$

If $P_{atm} \leq 0.53P_{out}$, the choked case:

$$\gamma_{outL} = 0.58 \tag{2.47}$$

Here, the gas was assumed ideal and the nonlinearity of the flow was considered in Equations (2.42), (2.43), (2.46) and (2.47). One can obtain the equation of $\dot{P_{out}}$ in the following form by substituting Equation (2.35)-(2.47) into Equation (2.1) and letting $\dot{Q} = \alpha_L \dot{W}$ as it was treated in the actuator piston model:

$$\dot{P_{out}} = \frac{1}{A_{cL}z}[C_{dinL}A_{out}(z)P_p\gamma_{inL}kP_p\sqrt{\frac{kP_p}{\rho_p}} - C_{doutL} \tag{2.48}$$
$$A_L(z)\gamma_{outL}RkT_{atm}\sqrt{k\rho_{out}P_{out}}] - \alpha_L k\frac{P_{out}\dot{z}}{z}$$

Here, α_L is a number from 0 to 1 depending on heat loss, and C_{dinL} and C_{doutL} are the discharge coefficients. Applying mass conservation law to the control volume results in:

$$\dot{m_i} - \dot{m_e} = A_{cL}(\rho_{out}\dot{z} + \dot{\rho_{out}}z) \tag{2.49}$$

Replacing $\dot{m_i}$ with Equation (2.39) and replacing $\dot{m_e}$ with Equation (2.44) in the equation above, $\dot{\rho_{out}}$ equation can be written as below:

$$\dot{\rho_{out}} = \frac{1}{A_{cL}z}[C_{dinL}A_{out}(z)\gamma_{inL}\sqrt{k\rho_p P_p} \tag{2.50}$$
$$-C_{doutL}A_L(z)\gamma_{outL}\sqrt{kP_{out}\rho_{out}}] - \frac{\rho_{out}\dot{z}}{z}$$

Finally, Newton's Second Law yields the equation of motion of the outlet port valve:

$$m_{cL}\ddot{z} + C_{cL}\dot{z} + K_{cL} = A_{outlet}P_{out} - A_{cL}P_{cupL} \tag{2.51}$$
$$0 \leq z \leq z_{max}, A_{outlet} = \pi r_1^2, A_{cL} = \pi r_2^2$$

- m_{cL} is the mass of the outlet port valve

- C_{cL} is the damping coefficient compensating for the friction loss of the valve
- K_{cL} is the spring constant
- z, $\dot{z}$, $\ddot{z}$ are the displacement, velocity and the acceleration of the outlet port valve
- z_{max} is the maximum distance which the outlet port valve is allowed to travel. The discontinuous nonlinearity in the port valve dynamics was considered in the simulation.

Rearranging Equation (2.51) to obtain an expression for $\ddot{z}$ results in:

$$\ddot{z} = \frac{1}{m_{cL}}(A_{outlet}P_{out} - P_{cupL}A_{cL} - C_{cL}\dot{z} - K_{cL}z) \tag{2.52}$$

All the discharge coefficients that are involved in the flow equations were determined numerically and experimentally.

2.3.5 Spool Valve

The armature of the solenoid pushes the stem of the spool valve with the magnetic force F_s when the solenoid is energized and a pre-compressed spring returns the spool valve when the solenoid is de-energized. The spool valve is pressure balanced at two ends as shown in Figure 2.9. The equation of motion of the spool valve is:

$$m_{spool}\ddot{x} + C_s\dot{x} + K_s(x + \delta_s) = F_s, 0 < x < x_0 \tag{2.53}$$

Where m_{spool} is the mass of the spool valve, C_s is the damping coefficient modeling the frictional loss, K_s and δ_s are the stiffness and preload of the spring.

2.3.6 Solenoid

A solenoid can be modeled as an RLC circuit as shown in Figure 2.10. The Kirchoff law writes:

$$V_{in} - iR - L\frac{di}{dt} = 0 \tag{2.54}$$

Where, V_{in} is the pulse input voltage, i is the current, R and L are the resistance and the inductance of the solenoid. The relationship between the current i in the coils and the magnetic force F_s on the armature is assumed to take the following form:

$$F_s = L + \frac{bi^2}{1 + \frac{x}{a}} \tag{2.55}$$

Here, a and b are chosen to curve fit the empirical data provided by the manufacture.

2.4 Simulations and Experiments

2.4.1 Experimental Setup

Figure 2.11 displays the devices that were used in the experiments. A Ford 5.4 liter 4-valve V8 engine head was used for the valve test. The camshaft was removed on the intake valve side and an EPVA was installed above one of the intake valves. A Micro-Epsilon optoNCDT 1605 point range laser sensor was used to measure the displacement of the test intake valve. The laser sensor was mounted on an angle such that the laser beam from the emitter of the laser sensor would be perpendicular to the surface of the end of the valve stem. A dSPACE DS1104 PCI board was used for control and data acquisition. A switching circuit made of IGBT's (insulated gate bipolar transistor) amplified the signal from the computer and served as a driving circuit for the solenoids. Two STP2416-015 small push-pull solenoids were used to drive two spool valves in the EPVA. A DC power supply from Extech Instruments model 382203 was used to provide the electrical power for both the sensor and the circuit.

The experiments were conducted under the combinations of various control parameters:

- $30psi$ and $40psi$ supply pressure
- $100ms$, $40ms$ and $24ms$ solenoid durations that were corresponding to $1200rpm$, $3000rpm$ and $5000rpm$ engine speeds
- 30% and 25% solenoid duty cycles

Table 2.1. The Experiment Matrix at $30psi$

Control Parameters	The combinations of parameter sets					
Supply Pressure (psi)	30					
Solenoid Period (ms)	100		40		24	
Solenoid Duty Cycle (%)	30		30		30	
Time Delay Between two Solenoids (ms)	3	5	3	5	3	5

Table 2.2. The Experiment Matrix at $40psi$

Control Parameters	The combinations of parameter sets											
Supply Pressure (psi)	40											
Solenoid Period (ms)	100				40				24			
Solenoid Duty Cycle (%)	30		25		30		25		30		25	
Time Delay Between Two Solenoids (ms)	3	5	3	5	3	5	3	5	3	5	3	5

- $5ms$ and $3ms$ time delays between the first solenoid and the second solenoid

As given in Table 2.1 and 2.2, the experiment matrix listed 18 combinations of parameter sets under which the experiments were conducted, and the responses were compared with the simulation responses in the next section. The EPVA is aimed to tailor the engine intake flow without throttling. Therefore, in the experiments and simulations, the engine intake manifold pressure is considered to be close to atmospheric pressure. Since it is the intake valve that is being studied in here, no pressure loads are included on the valve head. In future studies where the exhaust valve will be studied, the valve will have to open against a high engine cylinder pressure. This model is capable of this type of simulation, but it is not included here since no experimental data is available for validation at this time.

2.4.2 Simulation

The equations of motion derived previously were written in state space form and programmed in $Simulink^{TM}$. The simulations were performed under the same parameter sets as were the experiments. The eighteen experiment and simulation responses are presented in Figure 2.12 through Figure 2.20. The dotted lines represent experimental responses and the solid lines represent the simulation responses. Figure 2.12 shows the responses under $30psi$ supply pressure, $100ms$ solenoid period with 30% duty cycle and $5ms$ vs. $3ms$ delay between two solenoids. The $100ms$ solenoid period corresponding to the engine speed at

1200rpm. The response with 5ms delay had about 6ms rising time and the response with 3ms delay had about 5ms rising time. The maximum valve lift height was 6mm for the response with 5ms delay and 3.8mm for the response with 3ms delay. The swing motion on the top of the profile shows that the valve is in the dwell stage when the hydraulic latch is utilized to hold the valve open. The slight compressibility of the oil in the hydraulic latch causes the oscillation of the valve response which damps out eventually. The hydraulic damper is initiated at 3.7ms, where the slope of the response is largely decreased and the response approaches to the original position gradually afterwards. The responses in Figure 2.13 were obtained under the same operating conditions as those in Figure 2.12 except that the solenoid period was reduced to 40ms, corresponding to 3000rpm. The rising time of the response with 5ms and response with 3ms were 6ms and 5ms. As the solenoid period is reduced, the dwell stage is shorter. The maximum valve lift height is 6mm for the response with 5ms delay and 4mm for the response with 3ms delay. The solenoid period then was reduced to 24ms, corresponding to 5000rpm. The responses are shown in Figure 2.14. In this case, the maximum valve lift is 5mm and the rising time is 6ms for the response with 5ms delay. The maximum valve lift is 4mm and the rising time is 5ms for the response with 3ms delay. The maximum valve lift height in the 5ms delay case is decreased from 6mm to 5mm. This happens because the solenoid is de-energized before the actuator piston can fully expand to its maximum displacement; the valve has to return without reaching its maximum lift. Moreover, the valve never enters the dwell stage in this pair of responses. The solenoid period is so short that the valve entered the air discharging stage immediately after the air charging stage. Hence, the swing motion disappears on the top of the profile. The experiment and simulation responses at 40psi pressure supply with 30% and 25% solenoid duty cycles are presented in Figure 2.15 through Figure 2.20. The response rising time of the valve varies from 4ms to 6ms. The maximum valve lift is around 8mm for the response with 5ms delay and 6mm for the response with 3ms delay in this case. As was expected, the valve lift height could be controlled by regulating the supply pressure or varying the delay between two solenoids, and the valve open duration could be

controlled by controlling the activation duration of the solenoid. The mathematical model was able to capture the dynamics of the EPVA closely.

2.5 Conclusions

This article presented a dynamic model for an electrically controlled pneumatic/hydraulic valve actuator. This model will be incorporated to develop criteria for both design and control of the valvetrain in a camless internal combustion engine. Two solenoids and two spool valves, a single acting cylinder, an inlet port valve, an outlet port valve, a hydraulic latch/damper and an intake valve with its valve spring were included in this model. The mathematical model employed Newton's law, mass conservation and principle of thermodynamics. The nonlinearity of the flow, incompressibility and compressibility of the hydraulic fluid and the nonlinearity of the motion due to the physical constraint was carefully considered in the modeling process. The control parameters were studied. The model was implemented in $Simulink/Matlab^{TM}$ under different combinations of operation conditions. Validation experiments were performed on a Ford 5.4 liter 4-valve V8 engine head with various air supply pressures, solenoid periods, solenoid duty-cycles and time delay between two solenoids. The numerical simulation results were compared with the experimental data and showed excellent agreement.

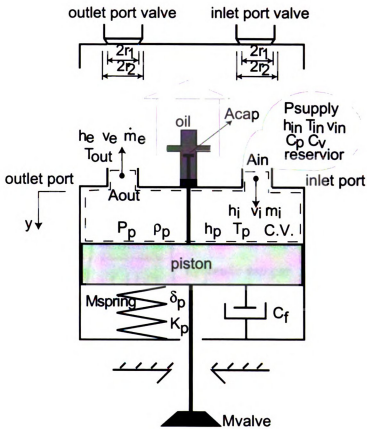

Figure 2.4. Actuator piston model

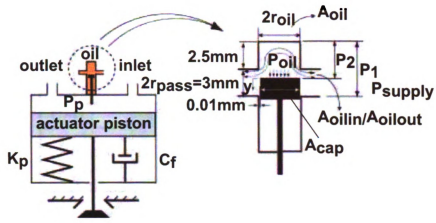

Figure 2.5. Hydraulic latch/damper model

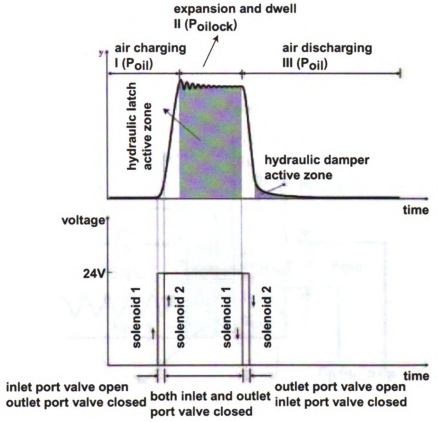

Figure 2.6. Valve lift profile with the solenoid action chart

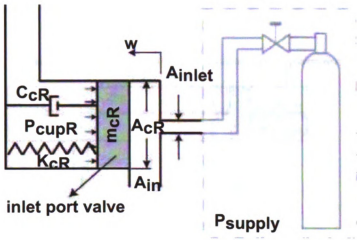

Figure 2.7. Inlet port valve model

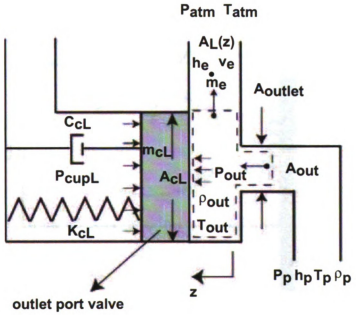

Figure 2.8. Outlet port valve model

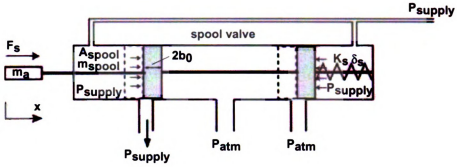

Figure 2.9. Spool valve model

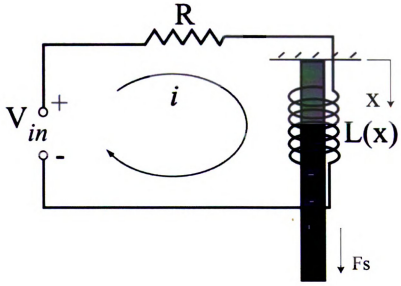

Figure 2.10. Solenoid model

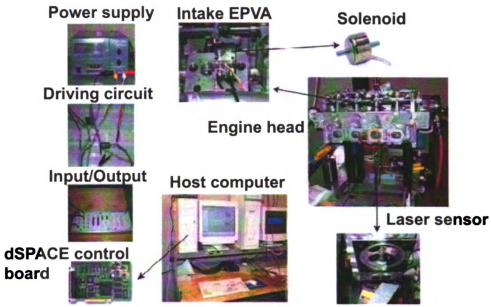

Figure 2.11. Experimental setup

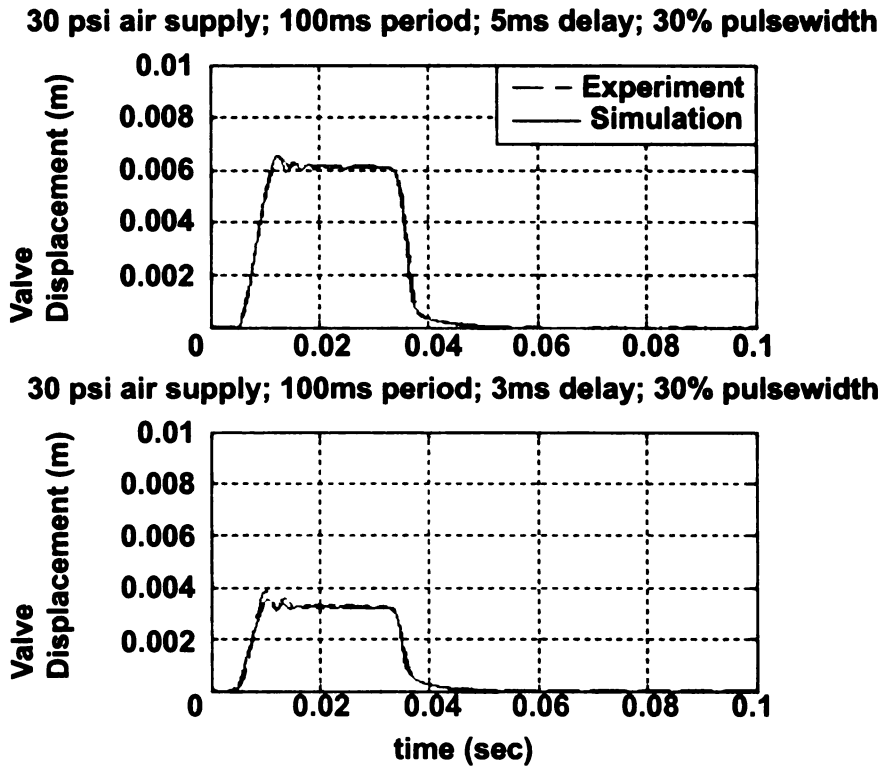

Figure 2.12. Simulation and experiment responses; 30*psi* pressure supply; 100*ms* solenoid period; 30% solenoid duty cycle; 5*ms* and 3*ms* time delay between two solenoids

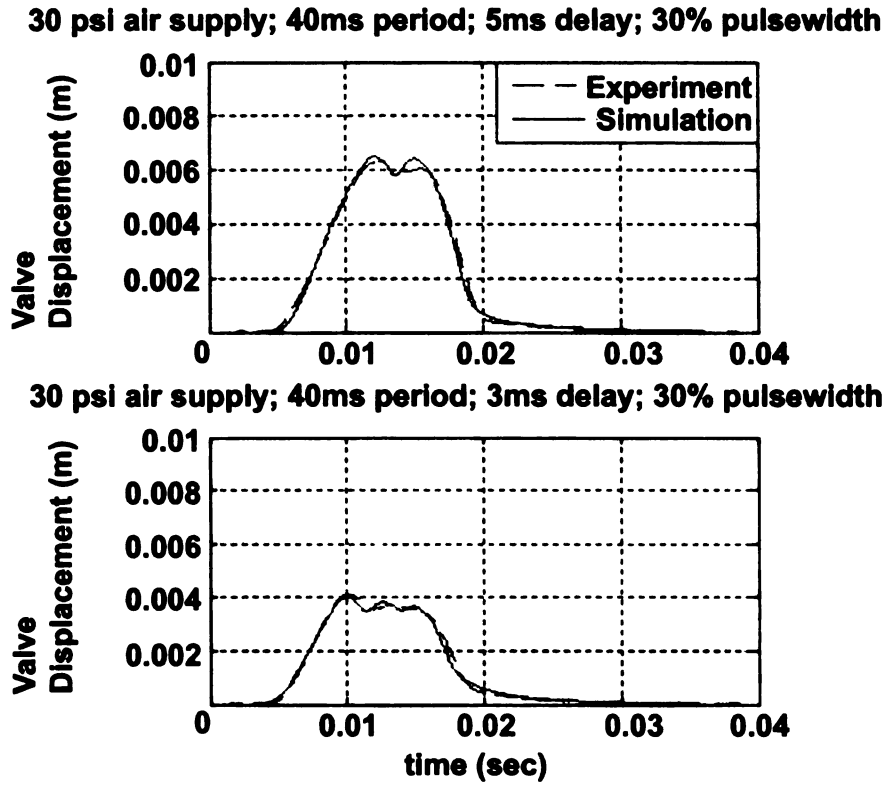

Figure 2.13. Simulation and experiment responses; $30psi$ pressure supply; $40ms$ solenoid period; 30% solenoid duty cycle; $5ms$ and $3ms$ time delay between two solenoids

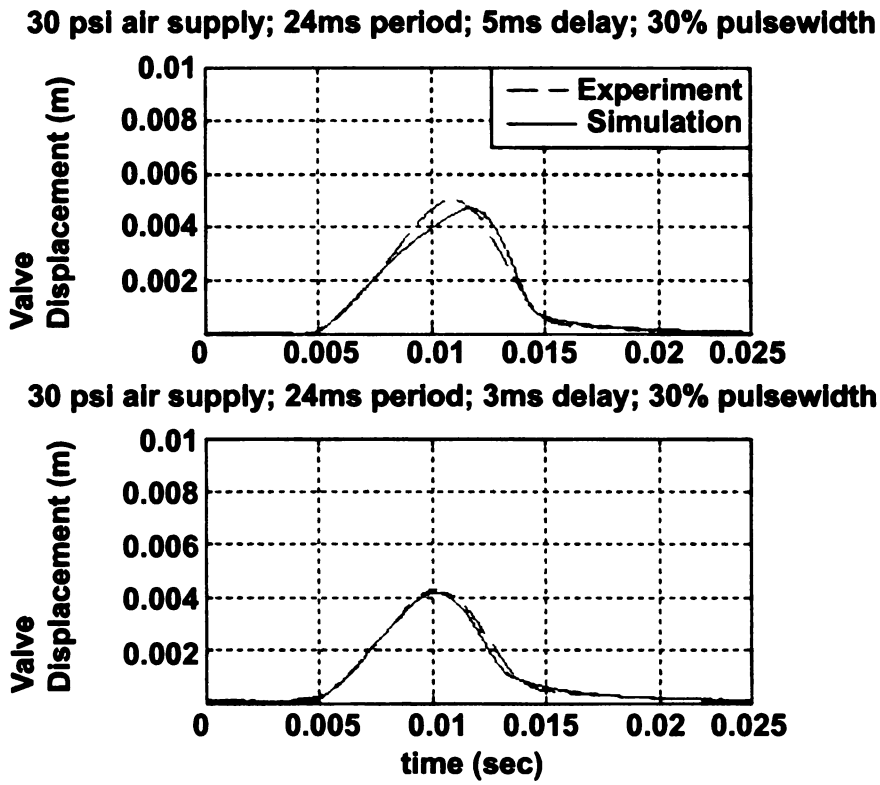

Figure 2.14. Simulation and experiment responses; $30psi$ pressure supply $24ms$ solenoid period; 30% solenoid duty cycle; $5ms$ and $3ms$ time delay between two solenoids

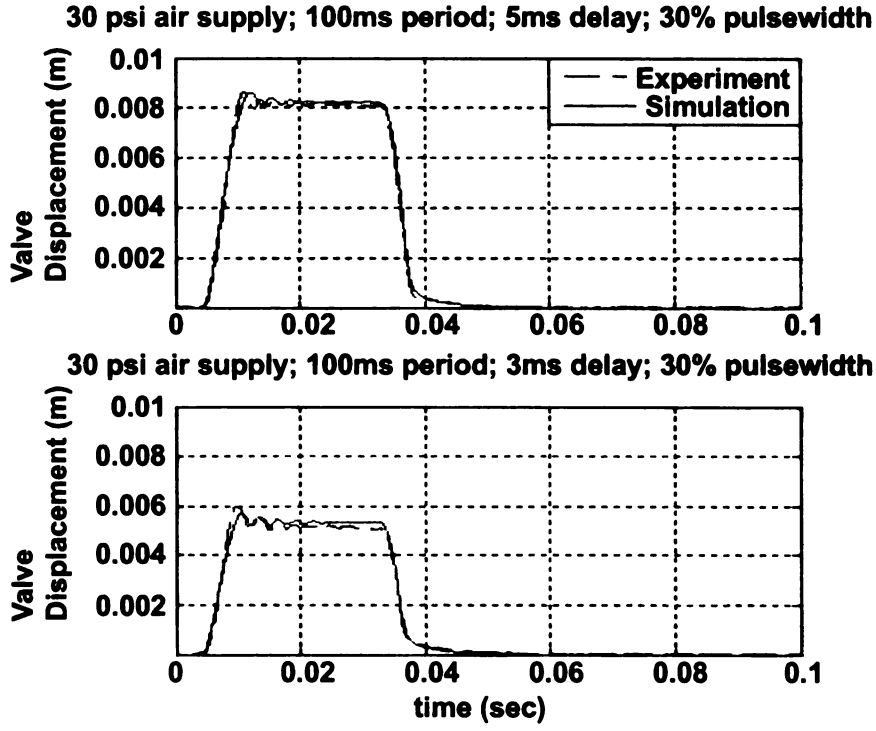

Figure 2.15. Simulation and experiment responses; $40psi$ pressure supply; $100ms$ solenoid period; 30% solenoid duty cycle; $5ms$ and $3ms$ time delay between two solenoids

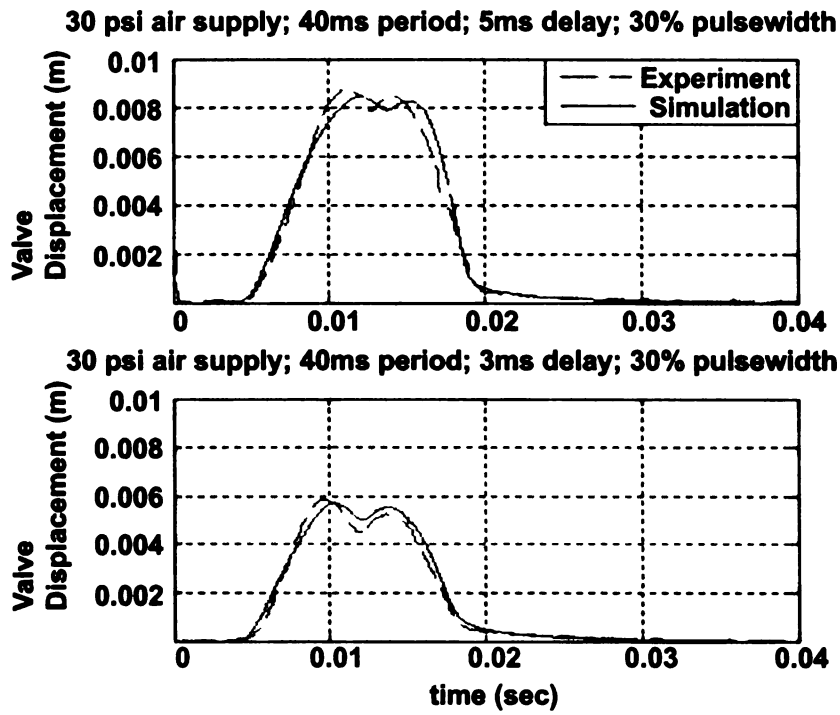

Figure 2.16. Simulation and experiment responses; 40*psi* pressure supply; 40*ms* solenoid period; 30% solenoid duty cycle; 5*ms* and 3*ms* time delay between two solenoids

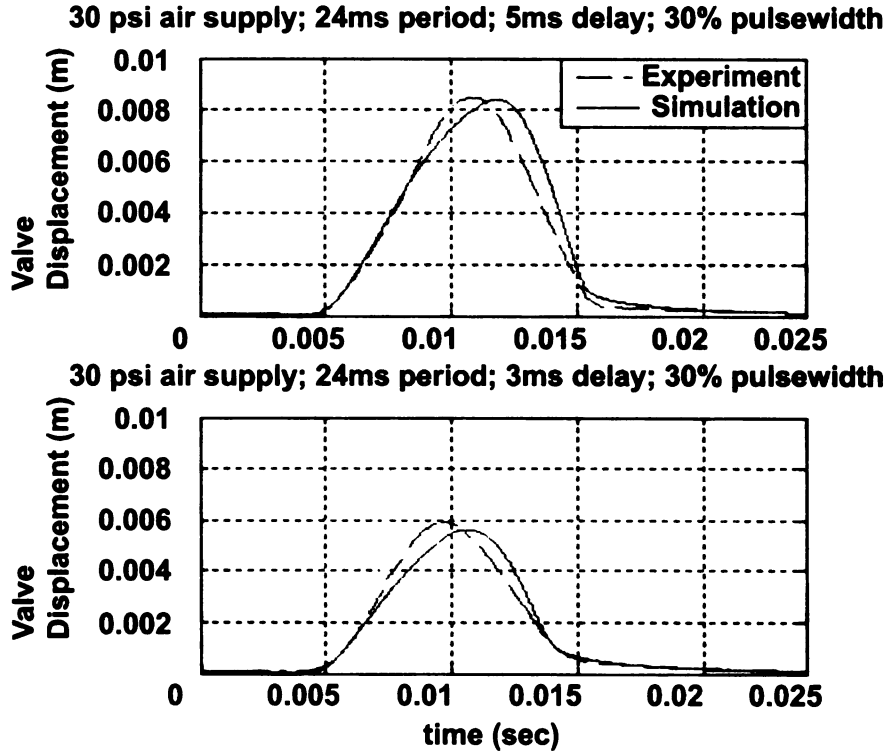

Figure 2.17. Simulation and experiment responses; $40psi$ pressure supply; $24ms$ solenoid period; 30% solenoid duty cycle; $5ms$ and $3ms$ time delay between two solenoids

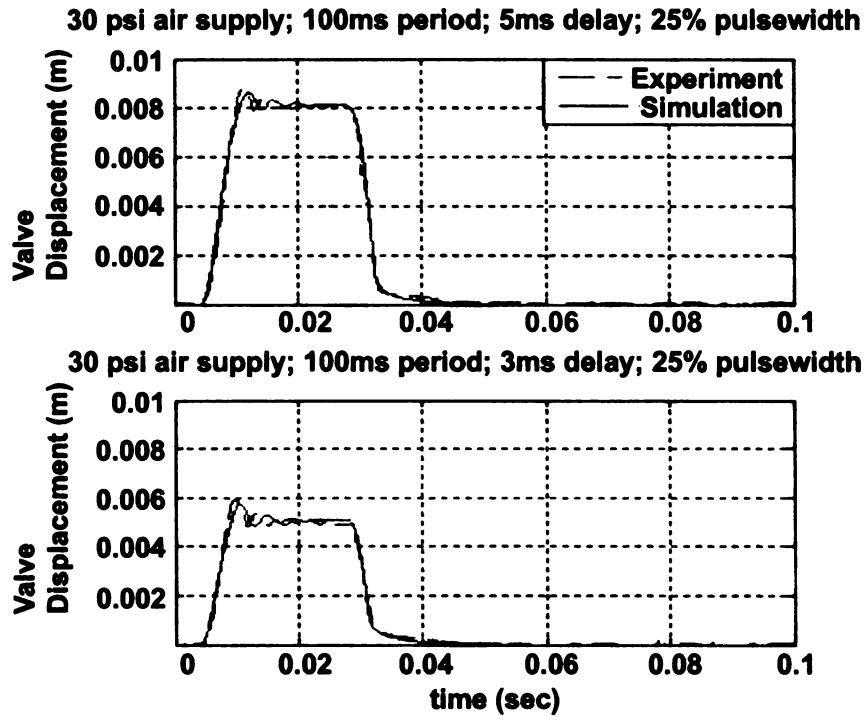

Figure 2.18. Simulation and experiment responses; $40psi$ pressure supply; $100ms$ solenoid period; 25% solenoid duty cycle; $5ms$ and $3ms$ time delay between two solenoids

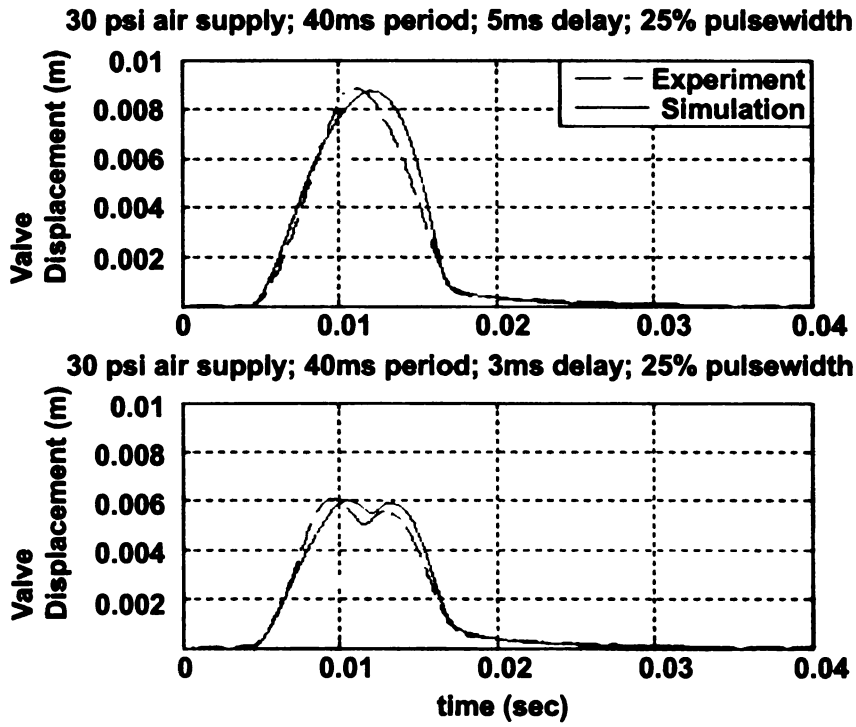

Figure 2.19. Simulation and experiment responses; $40psi$ pressure supply; $40ms$ solenoid period; 25% solenoid duty cycle; $5ms$ and $3ms$ time delay between two solenoids

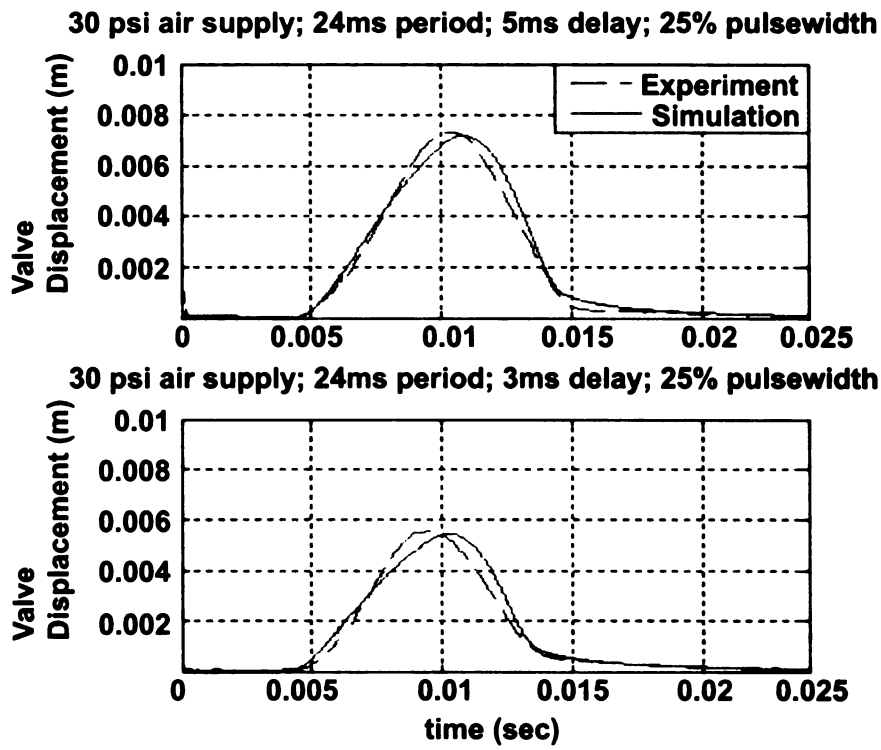

Figure 2.20. Simulation and experiment responses; $40psi$ pressure supply; $24ms$ solenoid period; 25% solenoid duty cycle; $5ms$ and $3ms$ time delay between two solenoids

CHAPTER 3

Intake Valve Control System Development

3.1 Introduction

The physics based nonlinear mathematical model developed in the previous chapter is called the level one model. In this chapter, a control oriented model, the level two model, was created. The adaptive intake valve control scheme was established. The convergence of the derived adaptive parameter identification algorithm was verified using the valve test bench data. The intake valve closed-loop control strategies was developed and validated in simulation.

3.2 Level Two Model

The level one model is a sophisticated nonlinear model which requires heavy computational throughput and is almost impossible to be implemented in real time. A control oriented model, called level two model, is needed in this case.

3.2.1 Review of System Dynamics

EPVA consists of an actuator piston, a hydraulic latch (damper), inlet and outlet port valves, two solenoids and two spool valves. The actuator piston is driven by compressed air. It sits on the back of the valve stem, hence, its motion is equivalent to the valve motion. Figure 3.1 shows the schematic diagram of an EPVA. A detailed description of EPVA dynamics and level one model can be found in chapter 2. The level two modeling work concentrates on the piston (end actuator) dynamics and omits the nonlinear flow dynamics. As illustrated in Figure 3.2, the valve operation process can be divided into three stages. They are opening stage I, dwell stage II and closing stage III.

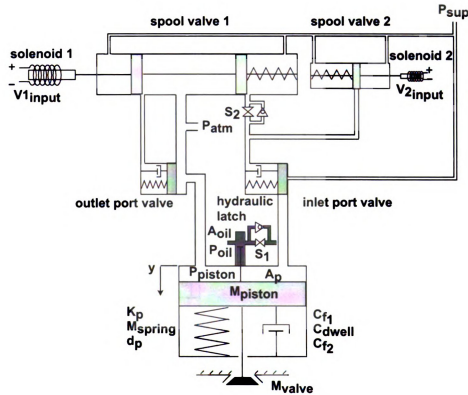

Figure 3.1. Valve lift profile with the solenoid action chart excluding system delays

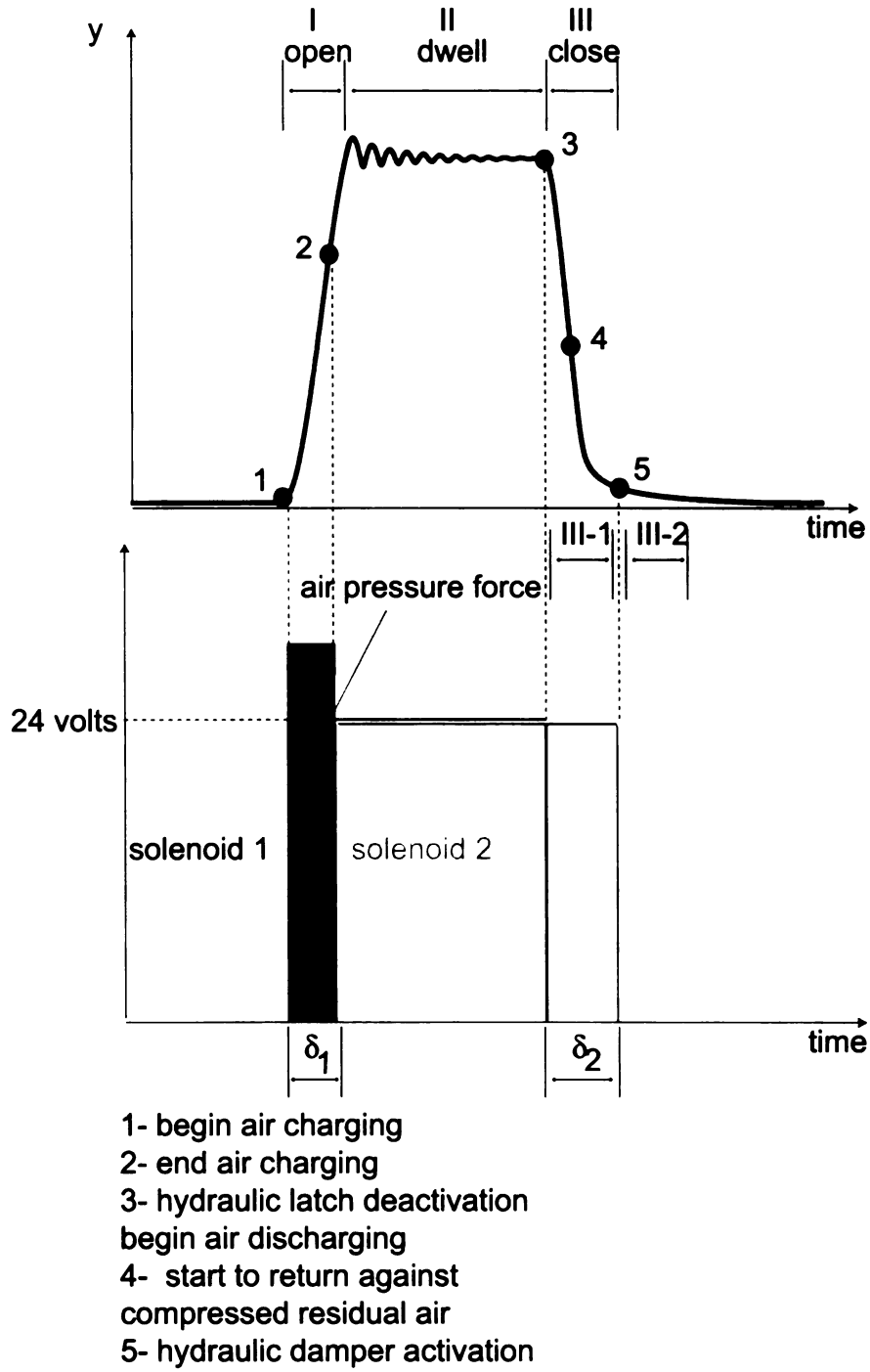

Figure 3.2. Valve lift profile with the solenoid action chart excluding system delays

3.2.2 Level Two System Modeling

Opening stage

In this stage the valve actuator is modeled as a second order mass-spring-damper system with zero initial conditions, see Equation (4.1).

$$M\ddot{y} + C_{f_1}\dot{y} + K_p(y + \delta_p) = F(t) - F(t - \delta_1) \tag{3.1}$$

$$F(t) = \begin{cases} 0, & \text{if } t < 0 \\ A_p P_p + A_{cap} P_{oil} - (A_p + A_{cap}) P_{atm} & \text{if } t \geq 0 \end{cases}$$

where $P_p = P_{oil} \approx P_{supply}$, and

- $M = M_{piston} + M_{valve} + \frac{1}{3} M_{spring} + M_{cap}$, where M_{piston} is the mass of the actuator piston, M_{valve} is the mass of the intake valve and M_{spring} is the mass of the valve spring. The effective spring mass equals one third of the total spring mass [15], and M_{cap} is the mass of the cap on the top of the valve stem;

- $A_p = \pi r_p^2 - \pi r_{oil}^2$ with r_p as the radius of the actuator piston and r_{oil} as the radius of the oil passage;

- C_{f_1} is the damping ratio approximating energy dissipation due to flow loss and frictional loss;

- K_p is the stiffness of the valve spring;

- δ_p is the preload of the valve spring;

- P_p is the in-cylinder air pressure, P_{oil} is the oil pressure and is at the same pressure as air supply, and P_{supply} is the air supply pressure;

- A_{cap} is the area of the cap on the top of the actuator piston stem;

- δ_1 is the lag between the activation of solenoid 1 and 2 without system delays as illustrated in Figure 3.2, and δ_2 is the time needed for valve to return to the seat.

Dwell stage

The equation of motion at stage II is described as follows:

$$M\ddot{y} + C_{dwell}\dot{y} + K_p(y + \delta_p) = A_p P_p + A_{cap} P_{oillock} - (A_p + A_{cap}) P_{atm} \tag{3.2}$$

where $P_p \approx P_{atm}$ since the supply pressure has been removed and the piston is fully extended at this stage, M is the total mass of the actuator system as described in Equation (4.1), C_{dwell} is the damping ratio approximating energy dissipation due to frictional loss at dwell (lock) stage, and $P_{oillock}$ is the oil pressure applied to piston stem in dwell stage. The state equation $PV^c = K = constant$ is used to obtain the expression for $P_{oillock}$ where a large c value was chosen to represent the low compressibility.

$$P_{oillock} V^c = P_i V_i^c \tag{3.3}$$

Substituting $V = A_{cap} y$ and $V_i = A_{cap} y_i$ into Equation (3.3) to obtain:

$$P_{oillock} = \frac{P_i y_i^c}{y^c} \tag{3.4}$$

where y_i is the maximum valve displacement, V_i is the volume of the fluid at the maximum valve displacement y_i, and P_i is the oil pressure P_{oil} at the peak valve lift height y_i.

Closing stage

Dynamic motion in the closing stage was divided into two sub-stages (sub-stages III-1 and III-2) as illustrated in Figure 3.2. Substage III-1 can again be separated into two segments. The first segment is from point 3, where the piston starts returning, to point 4; and the second segment is from point 4 to point 5 where the hydraulic damper becomes effective. In the first segment, piston motion is a free return, however, in the second segment, the piston returns against certain pressure due to in-cylinder compressed residual air. For simplicity, both segments were modeled as free returns. In substage III-2, the piston returns against largely increased hydraulic damping force that acts on the piston stem. The governing

equations at this stage are described in Equations (3.5) and (3.6). Equation (3.5) describes the response from point 3 to 5 (see Figure 3.2).

$$M\ddot{y} + C_{f_2}\dot{y} + K_p y + K_p \delta_p = 0 \tag{3.5}$$

where $y(0) = y_{max}$, and $\dot{y}(0) = 0$. The response beyond point 5 in hydraulic damping region follows the response of Equation (3.6).

$$\begin{aligned} M\ddot{y} + C_{f_2}\dot{y} + K_p(y + \delta_p) = A_p P_p + A_{cap} P_{oil} \\ -(A_p + A_{cap}) P_{atm} \end{aligned} \tag{3.6}$$

where P_{oil} is a constant in substage III-1. But it is a function of flow out area in the hydraulic damper in substage III-2. The detail derivation of P_{oil} can be found in chapter 2.

3.2.3 Level Two Model Validation

The simulation and experimental responses of the level two model are compared in Figure 3.3. The thin valve curve is the experimental response; and the thick one is the simulated response using level two model. Damping ratio at opening stage, C_{f_1}, and damping ratio at closing stage, C_{f_2} are identified manually by trial and error in this simulation. In the real time implementation, these damping coefficients will be adaptively identified online since they vary significantly with respect to temperature, fluid viscosity and engine operational conditions. The two curves close to the x axis are the measured solenoid currents, where the solid line is the dwell current of solenoid 1 and the dash line is that of solenoid 2. There are delays between the activation of the solenoids and the actual mechanical motions. The total delay associated with solenoids 1 and 2 are defined as Δt_1 and Δt_2 respectively. As shown in Figure 3.3, total delay of each solenoid rises in two steps. Taking solenoid 1 current as an example, the first rise is from the starting point to the first peak which represents the electrical delay; and the second rise is from the first peak to the second peak which

represents the magnetic delay. Algorithms were developed to detect Δt_1 and Δt_2 at each cycle. Δt_1 is used to follow reference opening timing by compensating the valve opening delay. Both Δt_1 and Δt_2 are used to modify the pulse width of air pressure force input δ_1 associated with the valve lift control. This will be discussed in the next section.

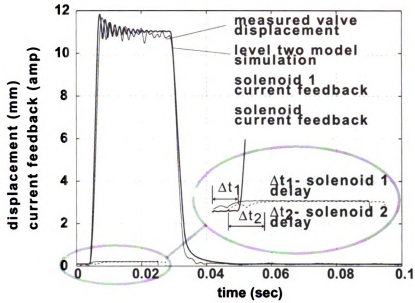

Figure 3.3. Level two model simulation and experiment responses

3.3 Control Strategy

The control strategy of valve timing, duration, and lift is addressed in this section. An adaptive parameter identification algorithm using model reference technique and MIT rule [9] played an important role in the control process. The identified parameters are then used to modify parameters in the closed-loop controller. Some approximations are introduced to obtain analytical solutions of control input in terms of the estimated parameters. To further reduce the computational efforts, only stages I and III of level two model were used in the controller. (see Figure 3.2). Parameters involved in the control process were investigated and defined for three possible cases. The closed-loop control scheme is proposed and the

concept is validated in simulation for closed-loop valve lift control. The closed-loop valve open and close timing control portion is similar to the valve lift control, and the results are not repeated in this section.

3.3.1 Parameter Definition

Figure 3.4 defines the parameters involved in control strategy. At low engine speed, the valve lift profile has all three stages as shown in the top diagram, where the holding period exists. This kind of response is categorized in case 1 (with holding). As engine speed increases, the holding period reduces. At certain engine speed, the holding period disappears, and the valve lift profile consists of only the opening and closing stages as shown in the bottom diagram. That is named as case 2 (without holding). In this case, solenoid 1 was deactivated shortly after its activation. It discharges the cylinder and allows valve to return before the hydraulic latch is engaged. In these two cases, both solenoids 1 and 2 are needed to control the valve event. There is another special case in which only solenoid 1 was used. The cylinder was simply charged with supply air when solenoid 1 is energized and discharged when solenoid 1 is de-energized. This occurs when the engine speed is so high that the activation duration of solenoid 1 becomes very small. The valve lift control is implemented by regulating air supply pressure in this case. Note that in both cases 1 and 2, the air supply pressure remains unchanged throughout the process. This special case is not the subject of discussion in this paper. As displayed in the left diagram of Figure 3.4, control pulses of solenoids 1 and 2 are generated based upon $DefA$ and $DefB$ pulses that are synchronized with engine crank angle. $DefB$ appeared to be nonzero during the time $DefA$ was sent, when the system needs to utilize both solenoids 1 and 2. $DefA$ and $DefB$ pulses carry the control information and they will be converted to solenoid command pulses.

The convention of this transformation is defined as follows. The first and second rising edges of $DefA$ correspond to the activation of solenoids 1 and 2. The first and second falling edges of $DefA$ correspond to the deactivation of solenoids 1 and 2. The first pulse width of $DefA$ is denoted as $\hat{\delta}_1$ and the second pulse width of $DefA$ is denoted as δ_2. $\hat{\delta}_1$

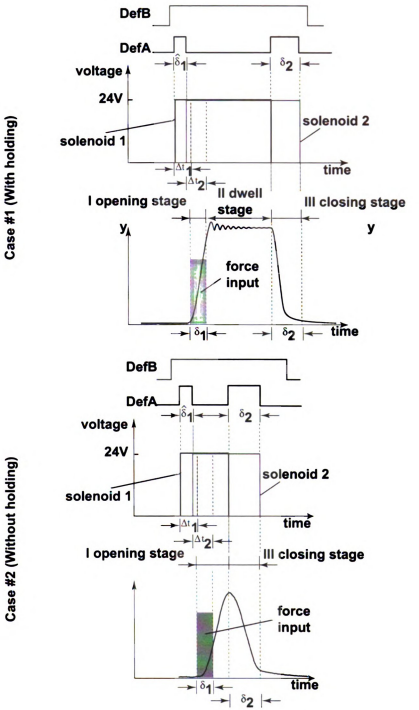

Figure 3.4. Control parameter definition for case 1 and case 2

is the time duration between the activation of two solenoids. The second falling edge of $DefA$, which is also the falling edge of solenoid 2 pulse, is defined to be the desired valve closing time. δ_2 represents the time needed for the valve to return after the deactivation of solenoid 1 (at valve return point). Activation of solenoids 1 and 2 begins their impact on the system after time delays Δt_1 and Δt_2 respectively. The air pressure in the piston cylinder rises and forms a pulse force input to the system with a pulse width δ_1. Therefore, $\hat{\delta}_1$ associates with δ_1 through the expression $\hat{\delta}_1 = \delta_1 + (\Delta t_1 - \Delta t_2)$, given the fact that Δt_1 is always greater than Δt_2. The parameter convention described in the right diagram of Figure 3.4 for case 2 is similar to case 1. For both cases, desired valve opening and closing timing and desired valve lift are known variables.

3.3.2 Adaptive Parameter Identification

The architecture of adaptive parameter identification is illustrated in Figure 3.5, where $G_m(S)$ is the model and $G_p(S)$ is the plant. The goal of this estimator is to identify the damping ratios C_{f_1} and C_{f_2}, where C_{f_1} is for the opening stage and C_{f_2} is for the closing stage. The error e between model and plant outputs reduces as the estimated parameters converge. The excitation force u is a pulse input with PE of order infinity that meets the persistent excitation condition in the adaptive identification. The identification controller based on MIT rule utilizes the error between the model and plant outputs and generates the estimated C_{f_1} or C_{f_2}, where C_{f_1} and C_{f_2} update at every step during the identification period.

MIT rule

MIT rule states as follows.

$$J(\theta) = \frac{1}{2}e^2 = \frac{1}{2}[y(t) - y_m(t)]^2 \tag{3.7}$$

$$\dot{\theta} = -\gamma \nabla_\theta J(\theta) = -\gamma e \nabla_\theta e = -\gamma e \frac{\partial e}{\partial \theta} \tag{3.8}$$

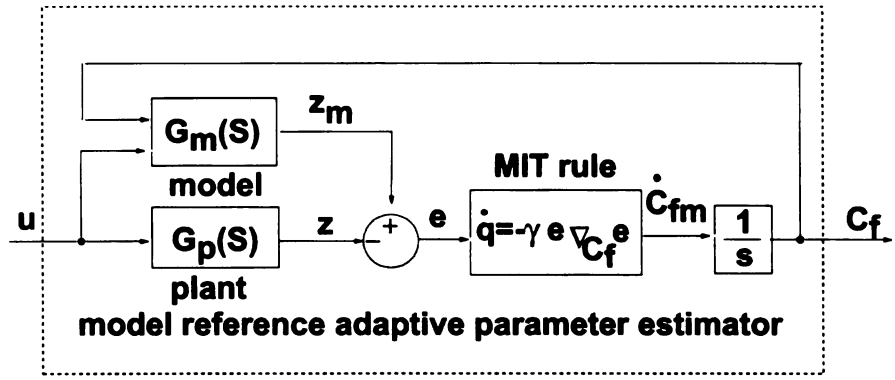

Figure 3.5. Model reference adaptive parameter identification scheme

where y, valve displacement, is the plant output and y_m is the model output of valve displacement, e is the error between the model and plant outputs, θ is the estimated parameter, and $\gamma > 0$ is the adaptive gain. In this case,

$$\theta = \begin{cases} C_{f_1}, & \text{for opening stage} \\ C_{f_2}, & \text{for closing stage} \end{cases}$$

Adaptive law at opening stage

In this section and the following section, the adaptive law at opening and closing stage is developed based on the MIT rule. The governing equation of the system at this stage is expressed in Equation (3.9).

$$M\ddot{y} + C_{f_1}\dot{y} + K_p y + K_p \delta_p = u(t) \tag{3.9}$$

where $y(0) = -\delta_p$, $\dot{y}(0) = 0$, and $u(t) = F(t) - F(t - \delta_1)$ by Equation (4.1). To change the coordinate, let

$$z = y + \delta_p \tag{3.10}$$

Equation (3.9) can be re-written in z coordinate as below:

$$M\ddot{z} + C_{f_1}\dot{z} + K_p z = u(t) \tag{3.11}$$

where $z(0) = \dot{z}(0) = 0$. Laplace transform of Equation (3.11) results in Equation (3.12):

$$MS^2 + C_{f_1} SZ(S) + K_p Z(S) = U(s) \tag{3.12}$$

The transfer function takes the following form:

$$G(S) = \frac{Z(S)}{U(S)} = \frac{1}{MS^2 + C_{f_1}S + K_p} \tag{3.13}$$

The error between the model output and the plant output in Laplace domain $E(S)$ can be expressed in the equation below:

$$\begin{aligned} E(S) = Z(S) - Z_m(S) = &\frac{1}{MS^2 + C_{f_1}S + K_p}U(S) \\ &- \frac{1}{MS^2 + C_{fm_1}S + K_p}U(S) \end{aligned} \tag{3.14}$$

where Z and Z_m are the plant and model outputs, and C_{f_1} and C_{fm_1} are the plant and model damping ratios. Let $P(S) = \frac{\partial E(S)}{\partial C_{fm_1}}$. We obtain $P(S)$ by taking partial derivative of $E(S)$ with respect to C_{fm_1}:

$$P(S) = \frac{U(S)}{MS^2 + C_{fm_1}S + K_p}\frac{S}{MS^2 + C_{fm_1}S + K_p} \tag{3.15}$$

Since $\frac{U(S)}{MS^2+C_{fm_1}S+K_p} = Z_m(S)$ by Equation (3.14), Equation (3.15) can be rearranged into Equation (3.16) :

$$\begin{aligned} P(S) &= Z_m(S)\frac{S}{MS^2 + C_{fm_1}S + K_p} \\ &= Z_m(S)\frac{1}{MS + C_{fm_1} + \frac{K_p}{S}} \end{aligned} \tag{3.16}$$

Taking the inverse Laplace transform of Equation (3.16) to obtain the adaptation law of $\dot{p}(t)$ results in Equation (3.17).

$$\dot{p}(t) = \frac{1}{M}\left(z_m(t) - C_{fm_1}p(t) - K_p\int p(t)dt\right) \tag{3.17}$$

The adaptation law of C_{f1} at opening stage is summarized below:

$$\begin{cases} \dot{C}_{fm_1} = -\gamma_1 p(t)e \\ \dot{p}(t) = \frac{1}{M}\left(z_m(t) - C_{fm_1}p(t) - K_p\int p(t)dt\right) \\ e = z - z_m = y - y_m \end{cases}$$

with $\gamma_1 > 0$ chosen to be an adaptive gain. The adaptation takes place between point 1 and the first peak on the valve response as indicated in Figure 3.2.

Adaptive law at closing stage

The adaptive law of C_{f2} at the closing stage can be derived in a similar way to the opening stage, and the result is presented below.

$$\begin{cases} \dot{C}_{fm_2} = -\gamma_2 q(t) e \\ \dot{q}(t) = \frac{1}{M}\left(z_m(t) - C_{fm_2} q(t) - K_p \int q(t)dt - \int z(0)dt\right) \\ e = z - z_m = y - y_m \end{cases}$$

with $\gamma_2 > 0$ being an adaptive gain and C_{fm_2} being the model damping ratio. The adaptation occurs between points 3 and 4 as indicated in Figure 3.2, since the valve experiences a pure free return in this portion of the response.

3.3.3 Closed-Loop Control Scheme

Valve opening timing control can be achieved by compensating the identified solenoid 1 delay Δt_1 at every cycle. Controller design in this subsection focuses on the valve lift and closing timing control. These involve the adjustment of $\hat{\delta}_1$ and δ_2.

Closed-loop valve lift and closing timing control

Since the estimated damping ratios are available due to adaptive parameter identification, the closed-loop valve timing and lift control scheme is developed based upon the identified parameters and the lift control algorithm is validated in simulation. The structure of the closed-loop controller with the parameter estimator is shown in Figure 3.6. The control goal is to let the plant output y track the desired input y_{desire} and the desired closing timing. The nominal values of $\hat{\delta}_{1_o}$ and δ_{2_o} are computed based on the estimated C_{f_1} and C_{f_2}. They are the feedforward control signals to the system. The error between y_{max} and y_{desire} passes through an integrator and then adds onto the nominal $\hat{\delta}_{1_o}$. That produces $\hat{\delta}_1$ as a feedback signal to the system for valve lift control. The integral action is added to achieve the zero steady state tracking error and at the same time to reject the step type of disturbance. $u(\hat{\delta}_{1_o}, \delta_{2_o})$ can be depicted as a function that converts $\hat{\delta}_{1_o}$ and δ_{2_o} to the force input u. In the same manner, δ_2 is constructed as a feedback signal. This allows the closed-

loop controller to track the desired closing timing. K_1 and K_2 are two closed-loop gains. The control system operates in an open loop using pre-determined $\hat{\delta}_{1_i}$ and δ_{2_i} until the parameter identification algorithm converges, and then, switches to closed-loop control to minimize the tracking error. A detailed control scheme is presented in Figure 3.7. System

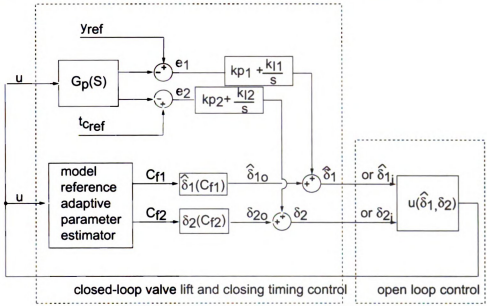

Figure 3.6. Closed-loop valve lift and timing control scheme

inputs include valve displacement, solenoids 1 and 2 current feedback, and supply pressure P_{supply}. Desired outputs are valve opening crank angle, valve closing crank angle, and valve lift height. This diagram includes the adaptive estimator that identifies both C_{f_1} and C_{f_2}, and an algorithm developed to detect critical points including maximum valve lift height, valve opening and closing locations and peak displacement, etc. These results are used by the following algorithm to identify Δt_1, Δt_2, $\hat{\delta}_1$ and δ_2. These four parameters are used to generates $DefA$ and $DefB$ pulses. $DefA$ and $DefB$ are then converted to solenoid commands sent to the valve actuator. It is critical to provide a suitable adaptation window which determines the start and end of adaptive identification at opening and closing stages. Moreover, the returning point at closing stage could be affected by a number of factors. It greatly depends on hydraulic latch performance, for instance, when the latch is released

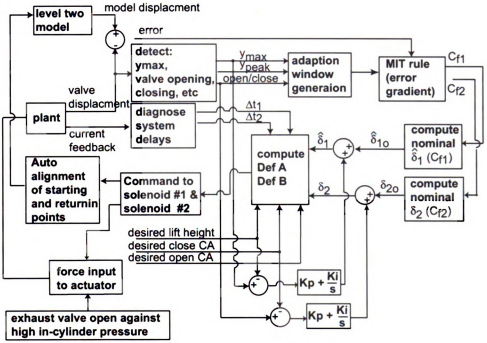

Figure 3.7. Control scheme with parameter identification based on model reference adaptation method

or whether there is certain oil leak in the latch. Inaccurate locations of the start point at opening stage and the return point at closing stage may cause instability of parameter identification. Algorithms were designed to allocate these locations automatically. This increases the robustness of parameter identification. The adaptive parameter identification algorithm is used to generate feedforward control signals. The feedback closed-loop control will be applied in real time to obtain the initial conditions close enough to the true values so that small adaptive gains can be used to acquire stability.

Solutions of $\hat{\delta}_{1_o}$ and δ_{2_o}

In order to compute $\hat{\delta}_{1_o}$ and δ_{2_o}, analytical solutions need to be established. It was found that the system damping ratio is between over-damped and slightly under-damped cases based upon the identified values. Therefore, two first order systems are employed to approximate the second order systems for both opening and closing stages in the region of interest. The closed-form analytical solutions are developed based on the first order system. The formulas of computing $\hat{\delta}_{1_o}$ in terms of C_{f_1} are provided by Equations (3.18), (3.19) and (3.20).

$$\hat{\delta}_{1_o} = \delta_1 - (\Delta t_1 - \Delta t_2) \tag{3.18}$$

$$\delta_1 = \frac{2}{\sigma} \ln(\frac{a}{a - y_{max}}) \tag{3.19}$$

$$a = \frac{f_0}{K_p} - \delta_p \tag{3.20}$$

where $f_0 = A_p P_p + A_{cap} P_{oil} - (A_p + A_{cap}) P_{atm}$ is defined by Equation (4.1). The formula of solving δ_{2_o} in terms of C_{f_2} is provided in Equation (3.21).

$$\delta_{2_o} = \frac{100}{C_{f_2}\sigma} \ln(\frac{\delta_p}{y_{max} + \delta_p}) \tag{3.21}$$

In Equations (3.19) and (3.21), σ is derived accordingly for three cases as follows:

$$\sigma = \begin{cases} \frac{C_f}{2M}, C_f^2 < 4K_pM & \text{underdamped} \\ \frac{C_f}{2M}, C_f^2 = 4K_pM & \text{critically damped} \\ |\frac{-C_f + \sqrt{C_f^2 - 4K_pM}}{2M}|, C_f^2 > 4K_pM & \text{overdamped} \end{cases}$$

with $C_f = C_{f_1}$ at opening stage or $C_f = C_{f_2}$ at closing stage.

Open-loop parameter estimation and closed-loop lift control simulation

The adaptive parameter estimation algorithm was simulated for 40 cycles and the results are presented in Figure 3.8 and Figure 3.9. The system was simulated with $80psi$ air supply pressure, $5ms$ lag between the activation of solenoids 1 and 2, $100ms$ solenoid period (equivalent to 1200RPM) and $25ms$ solenoid active duration. Figure 3.8 shows that C_{f_1} and C_{f_2} converge to 80 and 85 respectively. Note that these values are the damping ratios set in the plant model which served as the control target for simulation purposes. The error between the model and the plant outputs converges to a set tolerance in less than ten cycles. Figure 3.9 shows that after $\hat{\delta}_{1_o}$ and δ_{2_o} were evaluated with the solution based upon the identified C_{f_1} and C_{f_2}, they converge to $5ms$ (top) and $3ms$ (bottom) approximately. The estimated $\hat{\delta}_{1_o}$ is close to the true lag ($5ms$) used in the plant, and δ_{2_o} is also approached to the $3ms$ model plant closing duration. The closed-loop lift controller is validated in a 40 cycle simulation using the level two model. The simulation results are presented in Figure 3.10. The system was simulated with $80psi$ air supply pressure, $5ms$ lag between the activation of solenoids 1 and 2 during the open-loop parameter identification period, $100ms$ solenoid period (equivalent to 1200RPM) and $25ms$ solenoid active duration. The desired valve lift y_{desire} is $5mm$. The top diagram in Figure 3.10 displays the valve lift converging to the $5mm$ set point with zero tracking error. It can also observed from the middle diagram that that the nominal control input $\hat{\delta}_{1_o}$ is estimated to be $3.6ms$ based on the desired valve lift. As displayed in the bottom diagram of this figure, the plant is operated in an open loop condition to achieve the parameter convergence in the first ten cycles. The closed-loop control input $\hat{\delta}_1$ dropped from its initial value to $3.68ms$ at the eleventh cycle. This indicates the beginning of the closed-loop control and the system detects the reference input at this point. In the next cycle, the valve lift was brought down to $5mm$. This one cycle transient response is one of the design criteria.

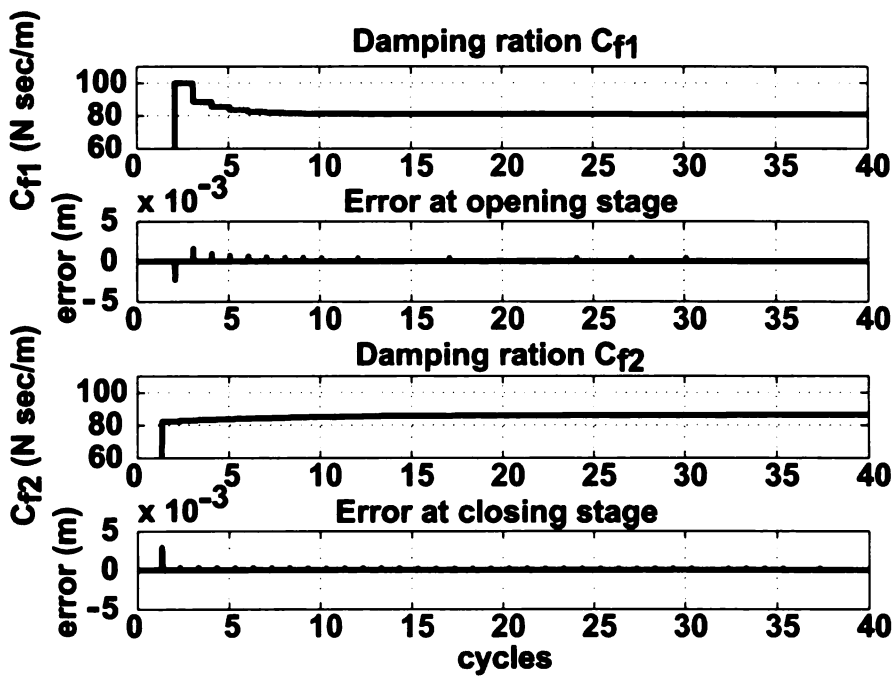

Figure 3.8. C_{f_1} and C_{f_2} identification simulation with fixed valve operation at 1200RPM

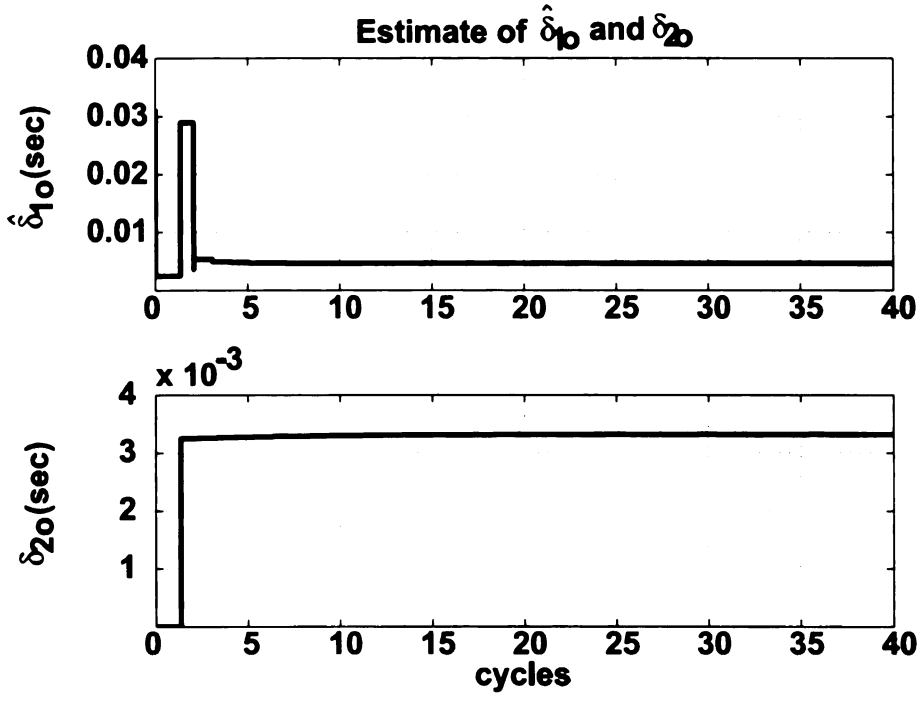

Figure 3.9. $\hat{\delta}_{1_o}$ and δ_{2_o} estimation simulation with fixed valve operation at 1200RPM

3.4 Verification of Parameter Identification Convergence on Test Bench

3.4.1 Intake Valve Control System Hardware Configuration

An $Opal - RT^{TM}$ real-time control system was employed as a real time controller for the hardware-in-loop bench tests. This system consists of two 3.2GHz CPU's equipped with two 16 channel A/D and D/A boards and one 16 channel digital I/O board. The communication between the two CPU's is a high performance serial bus IEEE 1934 fire wire with the data transfer rate at 400MHz per bit. CUP #1 is used for engine controls and CPU #2 is dedicated for controlling the EPVA.

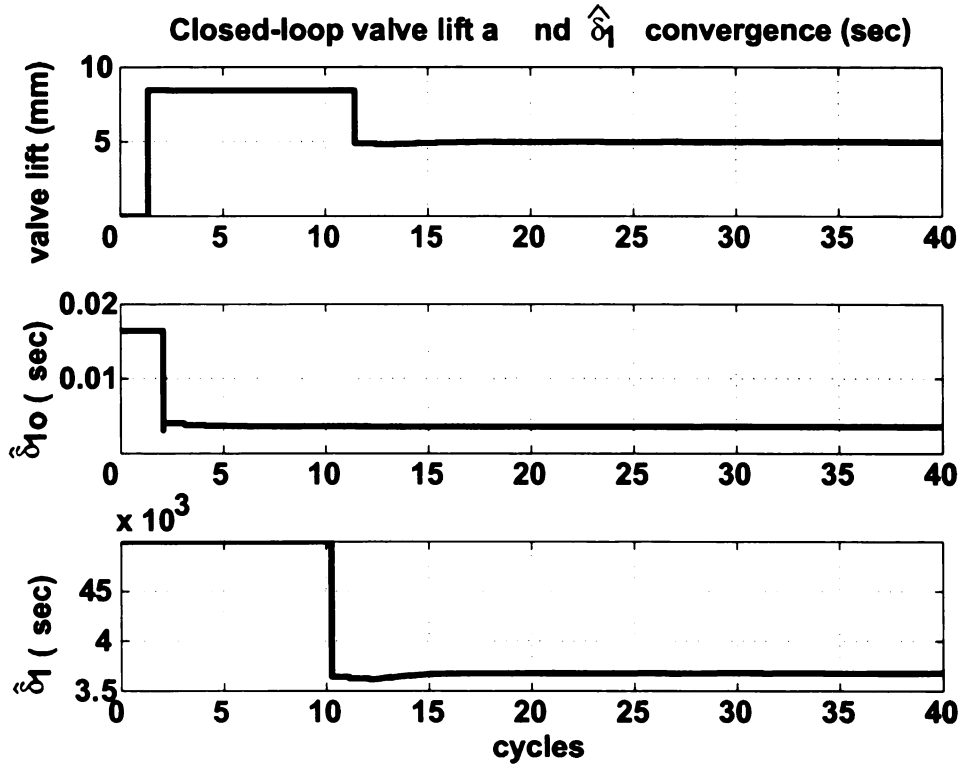

Figure 3.10. Closed-loop valve lift control at 1200RPM

3.4.2 Intake Valve Actuator Driving Circuit

The solenoid driving circuit was designed to amplify the signal from the D/A outputs of the real time controller and to sense the solenoid current. The circuit is required to have a short solenoid release time and fast switching capability with low noise. The circuit was made of switching MOSFETs (Metal-Oxide Semiconductor Field-Effect Transistor) and NPN BJT (Bipolar Junction Transistors).

3.4.3 Evaluation of Parameter Identification Convergence

EPVA bench tests were conducted using a cylinder head of 5.4 liter 3 valve V8 engine. 200 cycle data was recorded at different engine speeds. The convergence of adaptive parameter identification algorithm was verified using the bench test data. There are two sets of data equivalent to engine speed at 1200RPM and 5000RPM. At 1200RPM, the test parameters are $80psi$ air supply pressure, $100ms$ solenoid period with $25ms$ solenoid active duration. The lag between the activation of solenoids 1 and 2 was $5ms$. The parameter identification resulting at 1200RPM are presented in Figures 3.11, 3.12 and 3.13. Figure 3.11 shows that C_{f_1} and C_{f_2} converge to 55 and 65, where the error between model and plant outputs reduce to less than the given tolerance. Figure 3.12 displays $\hat{\delta}_{1_o}$ and δ_{2_o} computed with the estimated C_{f_1} and C_{f_2}. Both parameters converges to about $5.8ms$ and $3ms$ respectively and they are close to the true lag of $5ms$ and the measured return time of $3ms$. The last cycle of valve response with the model response is displayed in Figure 3.13. The two rectangular windows are the parameter identification regions for opening and closing stages. The adaptive algorithm is inactive outside these two windows. The test parameters at 5000RPM are $80psi$ air supply pressure and $24ms$ solenoid period with $6ms$ solenoid active duration. The lag between the activation of solenoids 1 and 2 was $5ms$. The parameter identification resulting at 5000RPM is presented in Figures 3.14, 3.15 and 3.16. Again, Figure 3.14 shows the convergence of C_{f_1} and C_{f_2}. Figure 3.15 shows that $\hat{\delta}_{1_o}$ and δ_{2_o} reach steady state values that are quite close to the true values. Figure 3.16 presents the

last valve lift with reference model outputs and the identification windows.

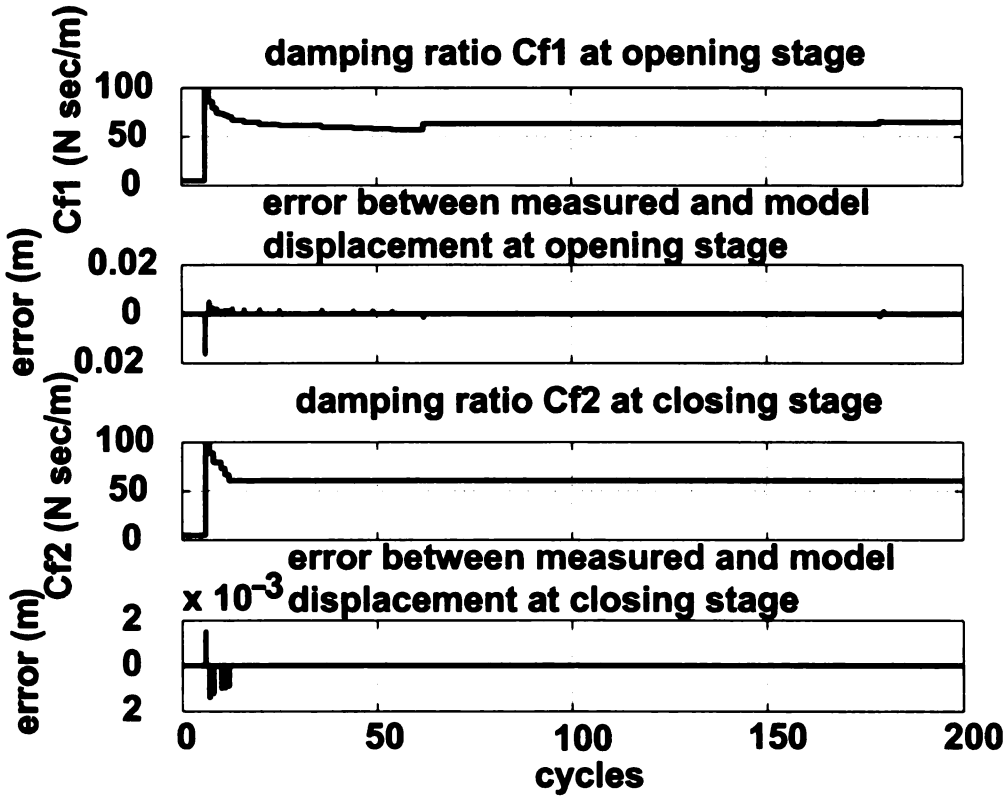

Figure 3.11. C_{f_1} and C_{f_2} identification with 200 cycle valve bench data at 1200RPM

3.5 Closed-loop Intake Valve Control Scheme for Real Time Application

This section presents the detailed closed-loop intake valve lift, opening and closing timing control schemes for the real time application.

3.5.1 Closed-loop Lift Control

The architecture of the closed-loop valve lift control is depicted in Figure 3.17. System inputs include reference valve displacement, solenoids 1 and 2 current measurements from

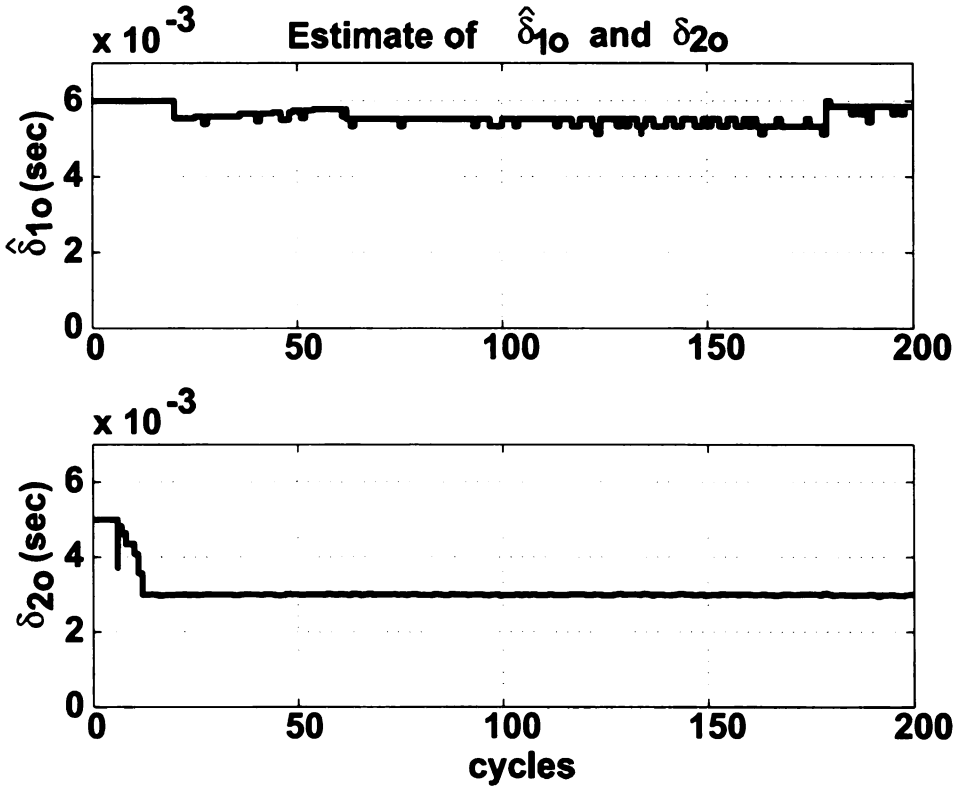

Figure 3.12. $\hat{\delta}_{1_o}$ and δ_{2_o} estimation with 200 cycle valve bench data at 1200RPM

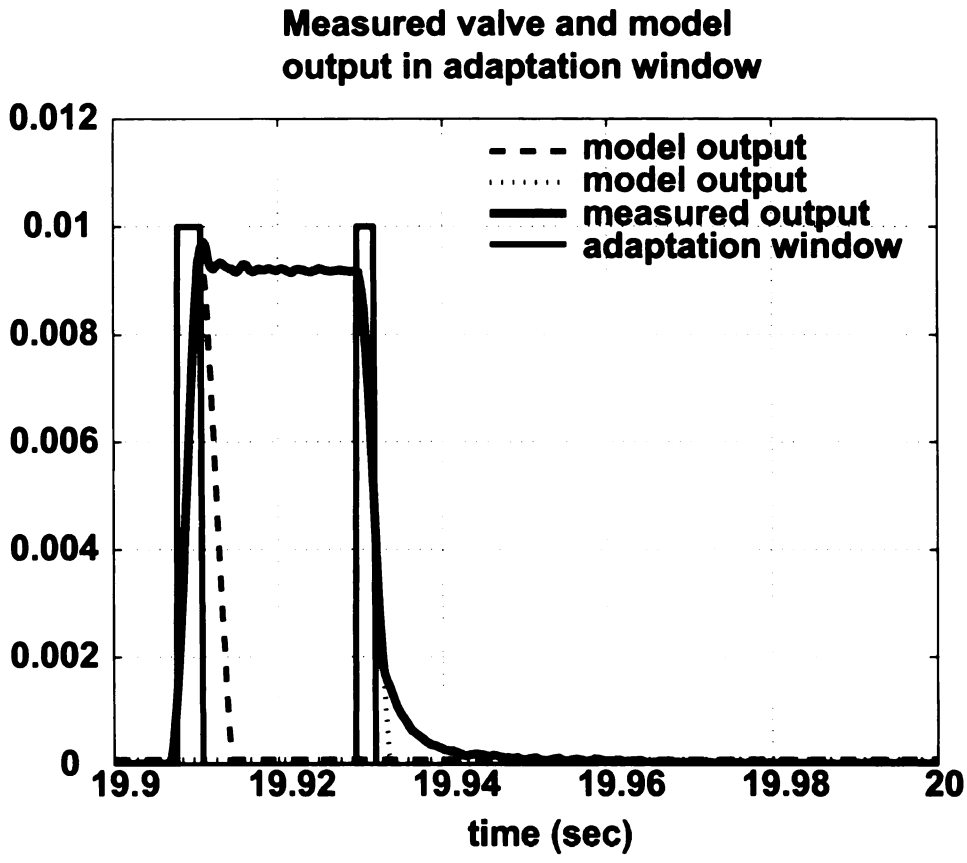

Figure 3.13. The last valve lift profile at 1200RPM with the reference model output

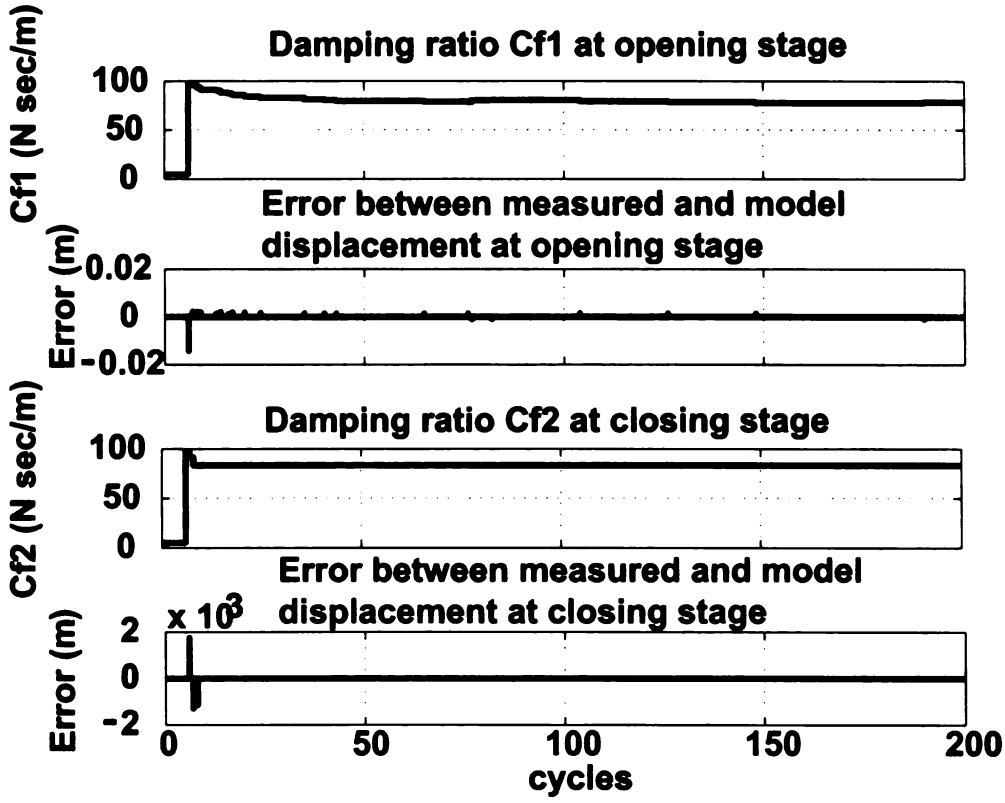

Figure 3.14. C_{f_1} and C_{f_2} identification with 200 cycle valve bench data at 5000RPM

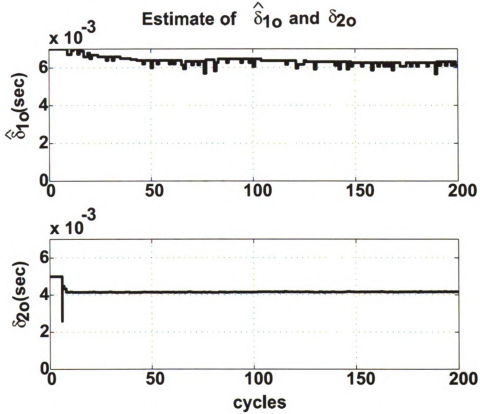

Figure 3.15. $\hat{\delta}_{1_o}$ and δ_{2_o} estimation with 200 cycle valve bench data at 5000RPM

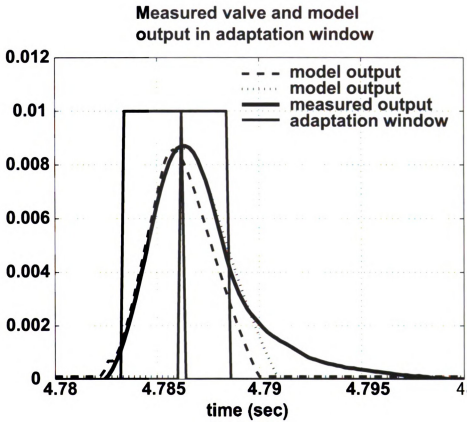

Figure 3.16. The last valve lift profile at 5000RPM with the reference model output

the solenoid driving circuit (see Experimental Implementation section), air supply pressure, and oil pressure. The valve lift height is the output. The lift control consists of two parts, the open-loop parameter identification for feedforward control and the closed-loop lift control using a PI scheme. The system starts with a short period of open-loop valve operation where C_{f_1} is estimated using a high adaptive gain to achieve fast convergence. A subroutine checking the convergence of C_{f_1} switches the system from open-loop operation to closed-loop control as soon as the identification error stays below a given tolerance for a reference number of cycles. The open-loop identification period can take around 50 cycles. The open-loop identification scheme and the closed-loop lift tracking scheme are displayed in the upper and lower dotted line blocks respectively.

The open-loop parameter identification scheme includes the plant, the model plant, and a driving circuit. The inputs of the driving circuit are the solenoid command pulses from the prototype controller's D/A. The outputs of it are the amplified solenoid commands and the solenoid current feedbacks. Moreover, the parameter identification scheme comprises an algorithm that creates a C_{f_1} identification zone where the adaptive algorithm is active and the displacement error is detected to be used by the adaptation law. The open-loop scheme also contains the model reference adaptive system involving the MIT rule with a high adaptation gain γ_1. The direct force input to the model plant is computed from the solenoid pulses by a subroutine. It guarantees that the model plant output starts at the same point as the plant output. These subroutines complete C_{f_1} identification. Meanwhile, the $DefA$ and $DefB$ pulses are generated by a pre-determined $\hat{\delta}_{1_i}$. They are converted to two solenoid pulses amplified by the driving circuit for the EPVA actuators.

In addition to the subroutines used in the open-loop parameter identification period, additional algorithms were developed for the closed-loop valve lift tracking control. There are algorithms that compute the feedforward nominal control input ($\hat{\delta}_{1_o}$), detect system delay Δt_1 and Δt_2 and compute critical points including maximum valve lift, valve opening and closing locations, peak displacement, and so on. In this block, the model reference adaptive system (MRAS) uses a low adaptation gain γ_1 to maintain parameter convergence

due to a sudden change of the valve displacement in a transient operational condition. The feedforward nominal control input $\hat{\delta}_{1_o}$ calculated from C_{f_1} needs to be sufficiently accurate to minimize the transient response time and the tracking error. The actual valve lift is a feedback signal to the system and it is subtracted from the reference valve lift to form the lift error. This error is the input of a proportional and integral (PI) controller with K_p as a proportional gain and K_i as an integral gain. The PI controller is updated every engine cycle. The output of the PI controller is then added onto the feedforward nominal input $\hat{\delta}_{1_o}$ to generate $\hat{\delta}_1$ as a controlled input to the system. The integral action is used to achieve the zero steady state tracking error. The $DefA$ pulse is generated based on $\hat{\delta}_1$. The $DefA$ and $DefB$ pulses are converted into solenoid commands. They are amplified by the solenoid driving circuit for the valve actuators.

As discussed in the Control System Hardware Configuration section, there are two CPU's in the prototype controller. CPU#1 operates at a relatively slower rate (1 ms) than CPU#2, but its outputs can be synchronized with the engine crank angle. CPU#2 is dedicated to valve operation at a sample rate of 40 microseconds since the valve control algorithms require fast sample rate. The CPU#2 also takes care of the conversion from the $DefA$ and $DefB$ pulses to the solenoid pulses. The PI controller is operated per engine combustion event. It is implemented in CPU#1 to reduce the computational throughput of CPU#2. $DefA$ and $DefB$ pulses are generated in CPU#1 since they are crank synchronized.

Closed-loop opening timing control

In order to track the reference valve opening timing calculated by the engine control CPU#1, the valve control system needs to detect the magnetic delay of valve solenoid 1 Δt_1 which is equivalent to the time lag between the activation of solenoid 1 and the actual valve opening. With known Δt_1, the control system can track the reference opening timing by compensating the delay Δt_1. The main task of this control scheme is the system delay detection and its closed-loop PI controller. The solenoid delay Δt_1 is calculated using

solenoid 1 current obtained from the solenoid driving circuit. It is used as feedforward control. The true valve opening timing is used as a feedback to the closed-loop controller, and it is subtracted from the reference valve opening timing to form an error signal of the PI controller. The output of the PI controller combined with feedforward control Δt_1 produces the final control input to the engine control system which updates the $DefA$ pulse. Most algorithms are implemented in CPU#2, except for the crank angle synchronized $DefA$ and $DefB$ pulse generation and the combustion event based PI controller that are implemented in CPU#1.

Closed-loop closing timing control

The closed-loop valve closing timing control and valve lift control schemes share the similar approach. Figure 3.19 shows the open-loop parameter identification for detecting C_{f_2} and the closed-loop valve closing timing controller. The adaptive gain γ_2 is high in the open-loop operation and low in the closed-loop operation. A pre-determined δ_{2_i} controls the valve closing timing in the open-loop operation. The system switches from open-loop to closed-loop control based upon the convergence criterion of the estimated C_{f_2} which is the same as the opening case. The feedforward control δ_{2_o} is computed from the identified C_{f_2}, and the system control output δ_2 consists of the feedforward control and the PI control output. Information from δ_2 is then used to generate $DefA$ pulse. The $DefA$ and $DefB$ pulses are sampled by CPU#2 and converted to solenoid control commands that are sent to the valve driving circuit. Again, the PI control algorithm and the formation of $DefA$ and $DefB$ pulses are implemented in CPU#1, and the rest of the algorithms are implemented in CPU#2. The closed-loop timing control scheme allows the actuator to track the reference closing timing.

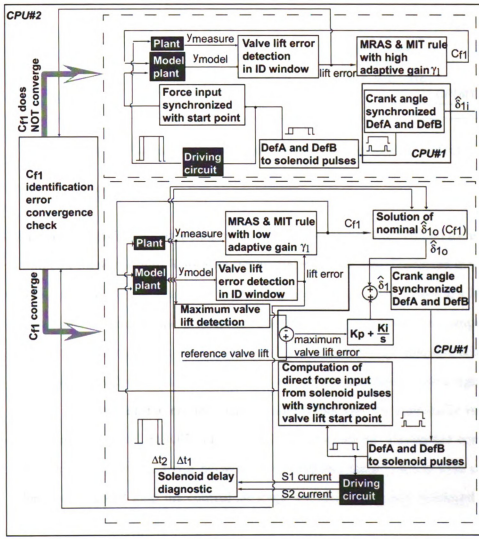

Figure 3.17. Schematics of closed-loop valve lift control

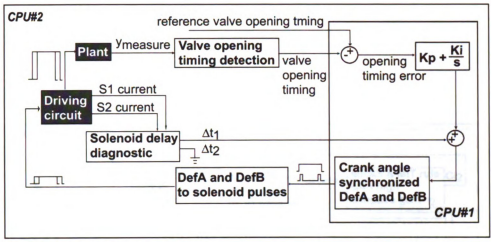

Figure 3.18. Schematics of closed-loop valve opening timing control

3.6 Conclusion

In this chapter, a control oriented model called level two model was developed for model reference parameter identification. This level two model is a piece wise linearized model based upon a previously developed nonlinear model which was built using Newton's law, mass conservation and thermodynamic principles. The level two model reduces computational throughput and enable real time implementation. A model reference adaptive scheme was employed to identify valve parameters required to generate real time control signals. The convergence of adaptive parameter identification algorithms was experimentally verified using the test bench data at 1200RPM and 5000RPM engine speed. Parameter convergence was achieved within 40 cycles. Error between the model and plant outputs were converged to set tolerances. Closed-loop lift control strategy was developed and validated in simulation. One cycle transient response and zero steady state tracking error was achieved in simulation. The detailed closed-loop intake valve lift, opening timing and closing timing control schemes were presented. The closed-loop intake valve control algorithm will be evaluated by experiments in chapter 5.

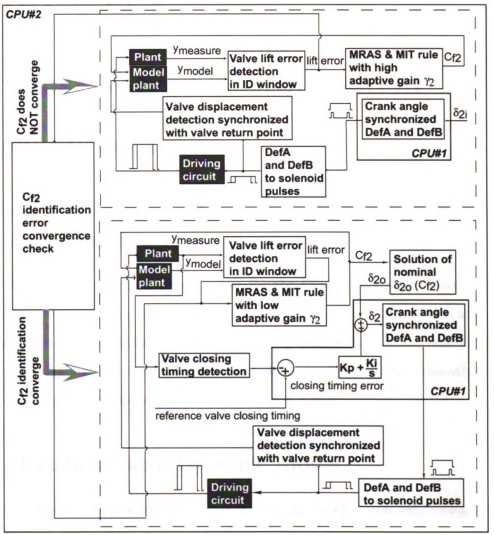

Figure 3.19. Schematics of closed-loop valve closing timing control

CHAPTER 4

Exhaust Valve Control System Development

4.1 Introduction

The modeling and control of intake valves for the Electro-Pneumatic Valve Actuators (EPVA) was shown in early chapters and chapter 4 extends the EPVA modeling and control development to exhaust valves for both valve timing and lift control. The control strategy developed utilizes model based predictive techniques to overcome the randomly variable in-cylinder pressure against which the exhaust valve opens.

4.2 Exhaust Valve Dynamic Model

A physics based nonlinear model, called a level one model, was built component-by-component based upon the flow and fluid dynamics. The details of the level one model and its verification can be found in chapter 2. This model provides an insight to the operation of the pneumatic/hydraulic mechanical actuation system. A piecewise linearized level two model was then created based on the level one model to reduce the computational throughput for control system development purpose. The details of the level two model are described in chapter 3. The level two model was used as the actuator model for the intake

valve in the previous studies. Here, it is used for the exhaust valve actuator modeling. The exhaust valve opens against a high in-cylinder combustion pressure with large cycle-to-cycle variations. This in-cylinder pressure produces a force on the face of the exhaust valve that affects the valve dynamics. This in-cylinder pressure is modeled and integrated with the exhaust valve actuator model to capture the exhaust valve dynamics. The system dynamics illustrated here focuses on the relationship between the solenoid control commands and the exhaust valve response. It follows the same analysis as that of the level two model which simplifies the system dynamics used for the level one model analysis. As shown in Figure 4.1, the valve response can be divided into three stages. They are the opening stage (I), dwell stage (II), and closing stage (III). Solenoid #1 is activated at point 0 first. It induces a high air pressure force to push the valve open at point 1 after Δt_1. Solenoid #2 is then activated (point 2) with a time lag $\hat{\delta}_1$. It removes this air pressure force Δt_2 time after solenoid #2 is activated (point #3). Note that the interplay between two solenoids results in a pulse force input to the actuator valve piston with pulse width δ_1. The increment of the pulse width increases valve lift. Now, with zero input, the valve movement continues until it reaches its peak lift at point #4, the valve equilibrium. This ends the open stage. Next, the valve enters the dwell stage where it is held open by a hydraulic latch mechanism. At the end of the dwell stage, solenoid #1 is deactivated at point #5. After Δt_3 time, the valve starts to return (point #6). The close stage starts at point #6 and ends at point #9 where the valve is considered closed. The returning duration is δ_2 between these two points.

The two solenoids have electro-mechanical delays after their activation and de-activation (see Figure 4.1). Δt_1 is defined as the delays for solenoid #1 at activation. Δt_2 is defined as solenoid #2 delay at activation. The de-activation delay for both solenoids are Δt_3. The solenoid commands direct the valve motion after the delays. The time lag applied between the activation of two solenoids is denoted as $\hat{\delta}_1$. This differs from the time lag between two delayed solenoid activations which is denoted as δ_1 since two solenoid delays, Δt_1 and Δt_2, are not equal. The exhaust valve lift control algorithm is to determine

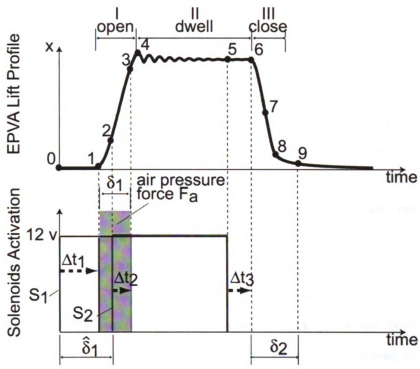

0: solenoid #1 activated
1: air pressure force on and valve opens
2: solenoid #2 activated
3: air pressure force off
4: valve peak displacement
5: solenoid #1 and #2 deactivated
5: valve returns without resistance
7: valve returns against cmpressed residual air
8: hydraulic damper activation
9: valve closes

S_1: solenoid #1
S_2: solenoid #2
Δt_1: solenoid #1 turn-on delay
Δt_2: solenoid #2 turn-on delay
Δt_3: solenoid #1 and #2 turn-off delay

Figure 4.1. Valve lift profile with the solenoid command chart

when to activate solenoid #2 during exhaust valve opening for each cycle with the varying in-cylinder pressure at the face of the valve and its activation delay in presence. It is impossible to remove the input force F_a instantly upon the activation of solenoid #2 due to its activation delay. An model based predictive lift control algorithm is developed to make this possible. The details are described in the control strategy section.

The exhaust valve closing timing control requires knowledge of δ_2, the amount of time that the valve takes to close. To guarantee the exhaust valve closing at the desired time requires de-activating solenoid #1 by time δ_2 before exhaust valve closing. δ_2 can be predetermined from the different valve lift set points. In other words, the closing timing control relies on a repeatable valve lift control. Developing a lift control system is the primary emphasis of work described in this paper.

The opening stage exhaust valve actuator model and the in-cylinder pressure model are employed to formulate the model based predictive lift control scheme. In order to validate the exhaust valve lift control algorithm, the level two model integrated with the in-cylinder pressure model is used as a plant model in simulation. The opening stage exhaust valve actuator model and the in-cylinder pressure model are introduced in the following two subsections.

4.2.1 Actuator Model

The opening stage exhaust actuator model with the in-cylinder pressure is studied in this section. This model is expanded based on the level two model from chapter 3 to include the in-cylinder pressure dynamics. Figure 4.2 shows the schematic diagram of the single actuating piston for this system. At the opening stage, the valve actuator is modeled as a second order mass-spring-damper system with zero initial conditions, see Equation (4.1). All pressures used in modeling and control formulation process are gauge pressure in this article.

$$M\ddot{y} + C_f\dot{y} + K_p(y + \delta_p) = F_a(t) - F_b(x) \tag{4.1}$$

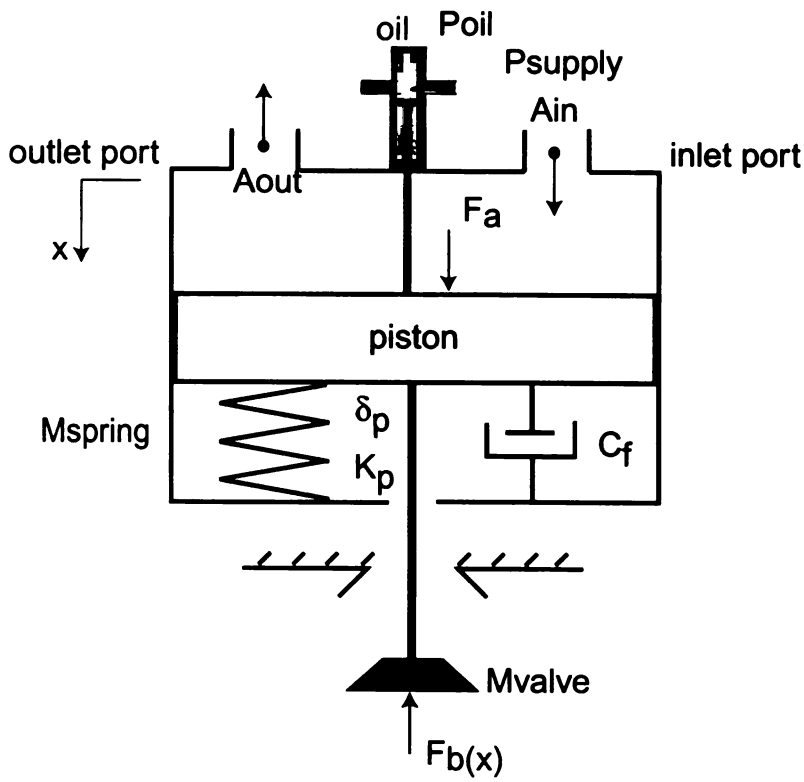

Figure 4.2. Actuator piston model

$$F_a(t) = F(t) - F(t - \delta_1) \tag{4.2}$$

$$F(t) = \begin{cases} 0, & \text{if } t < 0 \\ A_p P_p + A_{oil} P_{oil} & \text{if } t \geq 0 \end{cases}$$

where, $P_p = P_{oil} \approx P_{supply}$, and

- $F_b(x)$ is the in-cylinder pressure force at the back of the valve modeled in the next section;

- $M = M_{piston} + M_{valve} + \frac{1}{3} M_{spring} + M_{cap}$, where M_{piston} is the mass of the actuator piston, M_{valve} is the mass of the intake valve, M_{spring} is the mass of the valve spring. The effective spring mass equals one third of the total spring mass [15], and M_{cap} is the mass of the cap on the top of the valve stem;

- $A_p = \pi r_p^2 - \pi r_{oil}^2$ and $A_{oil} = \pi r_{oil}^2$ with r_p as the radius of the actuator piston and r_{oil} as the radius of the oil passage;

- C_f is the damping ratio approximating energy dissipation due to flow loss and frictional loss;

- K_p is the stiffness of the valve spring;

- δ_p is the preload of the valve spring;

- P_p is the in-cylinder air pressure, P_{oil} is the oil pressure and is at the same pressure as air supply, and P_{supply} is the air supply pressure;

- A_{cap} is the area of the cap on the top of the actuator piston stem;

- δ_1 is the lag between the activation of solenoid #1 and solenoid #2 after solenoid delays as illustrated in Figure 4.1, and δ_2 is the time needed for the valve to return to the seat.

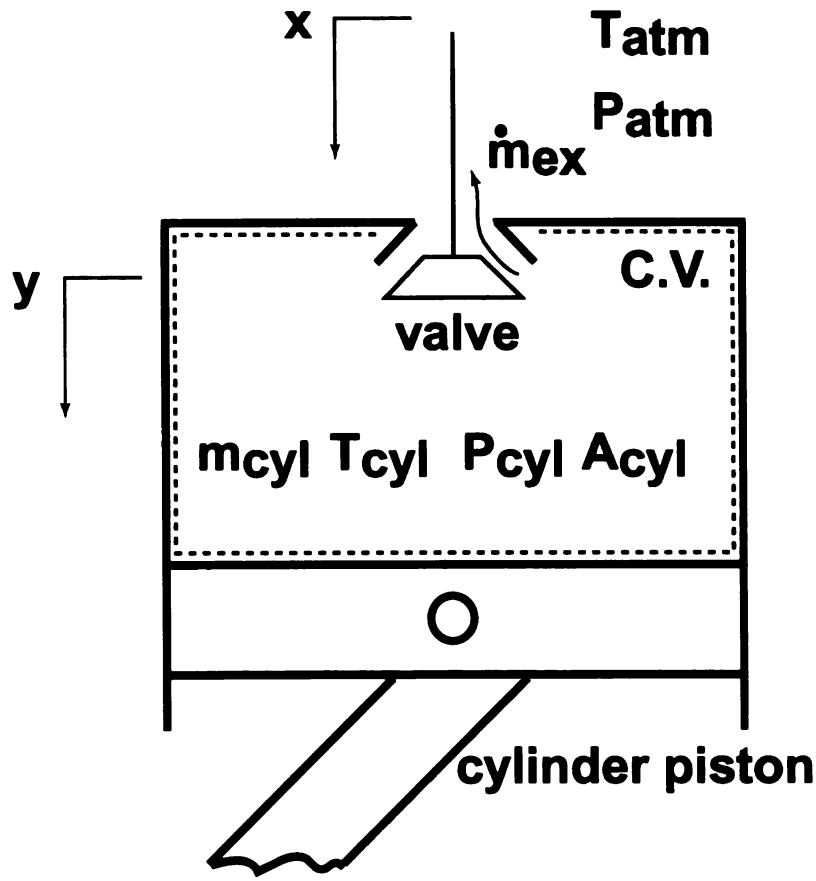

Figure 4.3. In-cylinder pressure model

4.2.2 In-cylinder Pressure Model

The in-cylinder pressure $F_b(x)$ needs to be modeled and evaluated in Equation (4.1). Figure 4.3 illustrates the dynamics in the combustion chamber with an exhaust valve. A control volume is drawn above the piston, where m_{cyl}, T_{cyl} and P_{cyl} are the mass, temperature and pressure inside the combustion cylinder. A_{cyl} is the engine piston area. $\dot{m}_{ex}$ is the mass flow rate at the exit when the exhaust valve opens. T_{atm} and P_{atm} are the atmospheric temperature and pressure. x and y are the exhaust valve displacement and cylinder piston displacement respectively. The mass flow rate equation at the exit are written for both choked and unchoked flow cases through Equations (4.3) to (4.5) following their derivation in [7].

$$\dot{m}_{ex} = C_{d_{ex}} \gamma P_{cyl} A_{ex}(x) \sqrt{\frac{k}{RT_{cyl}}}, \; A_{ex} = 2\pi r_{valve} x \tag{4.3}$$

where, A_{ex} is the flow area with r_{valve} being the valve radius; $C_{d_{ex}}$ is the flow coefficient at the exit; R is the residual gas constant. C_p and C_v are the specific heat of the residual gas at constant pressure and constant volume respectively and $k = \frac{C_p}{C_v}$. When $P_{cyl} \geq (\frac{k+1}{2})^{\frac{k}{k-1}} P_{atm}$, the flow is choked at the exit. In this case, γ is shown in Equation (4.4)

$$\gamma = \sqrt{(\frac{2}{k+1})^{\frac{k+1}{k-1}}}. \tag{4.4}$$

When $P_{cyl} \leq (\frac{k+1}{2})^{\frac{k}{k-1}} P_{atm}$, the flow is unchoked and γ is expressed in Equation (4.5)

$$\gamma = \sqrt{\frac{2}{k-1}} (\frac{P_{atm}}{P_{cyl}})^{\frac{k+1}{2k}} [(\frac{P_{atm}}{P_{cyl}})^{\frac{1-k}{k}} - 1]. \tag{4.5}$$

The mass of the residual gas inside the combustion cylinder in Equation (4.6) can be obtained by integrating the calculated mass flow rate. The initial mass m_0 is derived using ideal gas law, where P_0, V_0, R_0 and T_{cyl_0} are the initial in-cylinder gas pressure, volume, gas constant and temperature at the exhaust valve opening.

$$m_{cyl} = -\int_0^t \dot{m}_{ex} dt + m_0, \quad m_0 = \frac{P_0 V_0}{R T_{cyl_0}} \tag{4.6}$$

Using the ideal gas law again with the obtained m_{cyl} results in an expression of in-cylinder pressure as shown in Equation (4.7).

$$P_{cyl} = \frac{m_{cyl} R T_{cyl}}{V_{cyl}}, \quad V_{cyl} = A_{cyl} y. \tag{4.7}$$

where, k, R and T_{cyl} are variables acquired from the WAVE^{TM} simulation with the same engine configuration and parameters; and y is the piston displacement derived from the cylinder geometry in Equation (4.8).

$$y = r[1 + \frac{L}{r} - \cos(\theta) - \sqrt{\frac{L}{r} - \sin^2(\theta)}] \tag{4.8}$$

- $A_{cyl} = \pi(\frac{1}{2} \times bore)^2 = 0.0401m^2$ $(bore = 90.2mm)$
- L is the connecting rod length $(L = 169.2mm)$
- r is the crank shaft radius $(r = \frac{1}{2} stroke = 52.9mm)$
- θ is the engine crank angle.

Therefore, $F_b(x)$ can be expressed in Equation (4.9) below.

$$F_b(x) = P_{cyl} A_{valve}, \tag{4.9}$$

where P_{cyl} is defined in Equation (4.7).

4.2.3 Validation of In-cylinder Pressure Model by Simulation

The in-cylinder pressure force F_b is a function of the exhaust valve displacement since the flow out area A_{ex} is a function of the exhaust valve displacement. In order to validate the in-cylinder pressure model, combustion experiments were conducted using a 5.4L 3 valve V8 engine with in-cylinder pressure measurement and a conventional cam shaft at 1500RPM. The pressure model was simulated using the conventional cam profile as the valve displacement input. The modeled in-cylinder pressure was then compared with the measured in-cylinder pressure as shown in Figure 4.4. The top diagram of this figure shows

the modeled pressure (solid line) in the rectangular windows and measured in-cylinder pressure (dash line) with satisfactory modeling accuracy. The bottom diagram shows the exhaust cam profile used in the simulation and experiments. The in-cylinder pressure model

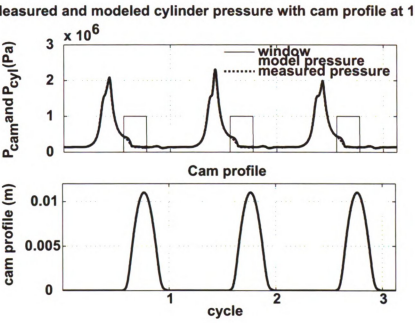

Figure 4.4. In-cylinder pressure model validation by simulation

is then integrated into the pneumatic exhaust valve model and the responses are shown in Figure 4.5. Here, the pressure model uses the EPVA valve displacement to calculate the corresponding in-cylinder pressure. The modeled pressure (solid line in top diagram) and the associated EPVA valve lift profile (solid line in bottom diagram) are compared with the experiment pressure (dash line) and the cam profile (dash line). The simulation result demonstrates that the in-cylinder pressure drops rather quickly with the EPVA exhaust valve actuation since the EPVA valve opens faster than the conventional cam based valve. This simulated in-cylinder pressure is used to construct the control signals. The exhaust valve model is used as a plant model and it is integrated with the in-cylinder pressure model in simulations to validate the control algorithm. The modeled in-cylinder pressure is one

of the two inputs to the plant (exhaust valve) and the actuation force F_a commanded by the two solenoid control signals is the other input.

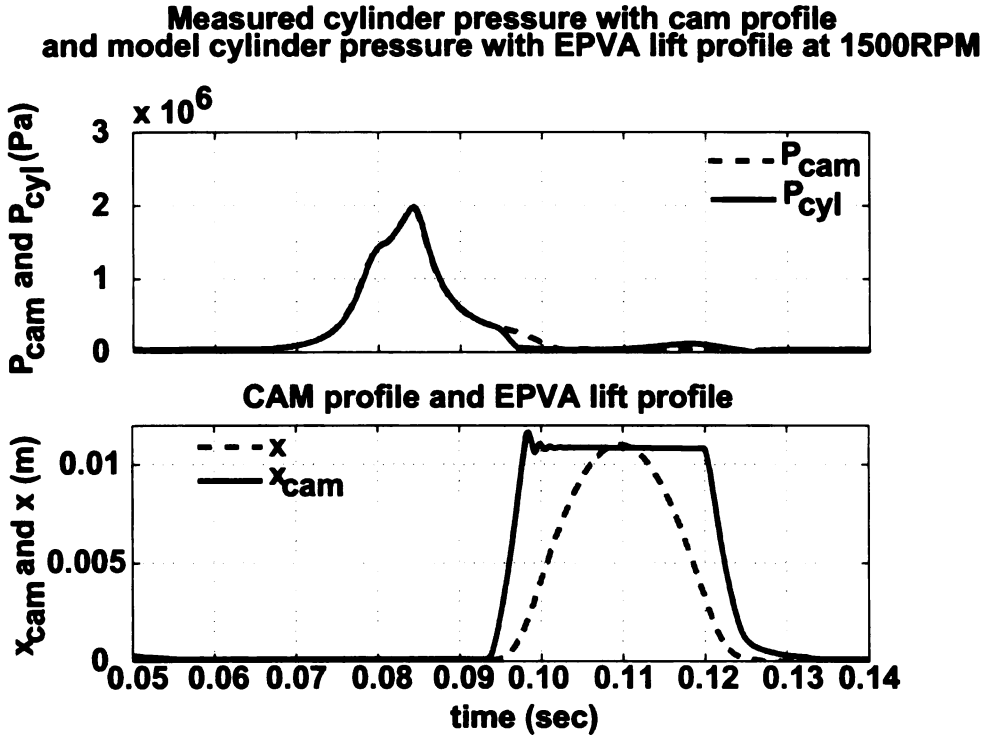

Figure 4.5. In-cylinder pressure model integrated into exhaust valve model

4.3 Control Strategy

Since the in-cylinder pressure on the face of the exhaust valve varies significantly from cycle to cycle, the valve lift control needs to be adjusted as a function of the current in-cylinder back pressure for each individual cycle. As explained in the actuator dynamics section, the exhaust actuator is modeled as a second order mass-spring damper system at the opening stage. Activating solenoid #1 applies the force F_a on the valve and moves the exhaust valve. Activating solenoid #2 removes the force and the valve continues to open until it reaches the maximum displacement. Solenoid #2 activation timing determines the

maximum valve lift. Therefore, the key for valve lift control is to find when to activate solenoid #2. Figure 4.6 illustrates the idea of the exhaust valve lift control strategy. Solenoid #1 is activated at time 0. After the delay of Δt_1, the input force F_a acts on the system and the exhaust valve starts to open at point 1. Solenoid #2 is then activated at point 2, after Δt_2 delay, force F_a is removed at point 3. The valve moves further until its velocity decreases to 0 at point 4. The second order valve system response from points 3 to 4 can be calculated with zero input and nonzero initial conditions at point 3. In other words, the valve peak displacement at point 4 can be calculated if the initial displacement and velocity at point 3 are known. Once the calculated displacement at point 4 reaches the reference maximum valve lift, point 3 is found to be the right time to remove force F_a. If activating solenoid #2 could turn off the input force F_a immediately, we would only need to activate it whenever the calculated displacement of point 4 reaches the reference lift. But the solenoid delay requires the activation to take place at point 2 with Δt_2 amount of time before point 3. This means that if point 3 is the time to eliminate input force, point 2 is the time to activate solenoid #2. However, the initial conditions at point 3 where the peak displacement of the valve is calculated are not yet available at point 2. Therefore, an algorithm is derived to predict initial conditions of point 3 at point 2. This strategy of initial condition prediction can be implemented as long as the delay Δt_2 of solenoid #2 is less than the lag $\hat{\delta}_1$ between the activation of two solenoids. The predictive algorithm needs to know both states, valve displacement and velocity, at point 2. An Kalman state estimator was used to estimate them with minimized effect of measurement noise. Now we can determine the time to activate solenoid #2 (point 2), which is served as a feedforward control of the valve actuator. A PI scheme is used as a feedback closed-loop lift control system to reduce the steady state lift tracking error.

The flow chart of the feedforward control scheme is shown in Figure 4.7. First, the solenoid #1 is activated. Secondly, the Kalman state estimator provides the current states. Finally, a model based prediction algorithm uses the estimated states to calculate the states after solenoid #2 delay Δt_2, which is then used to calculate the peak valve displacement. If

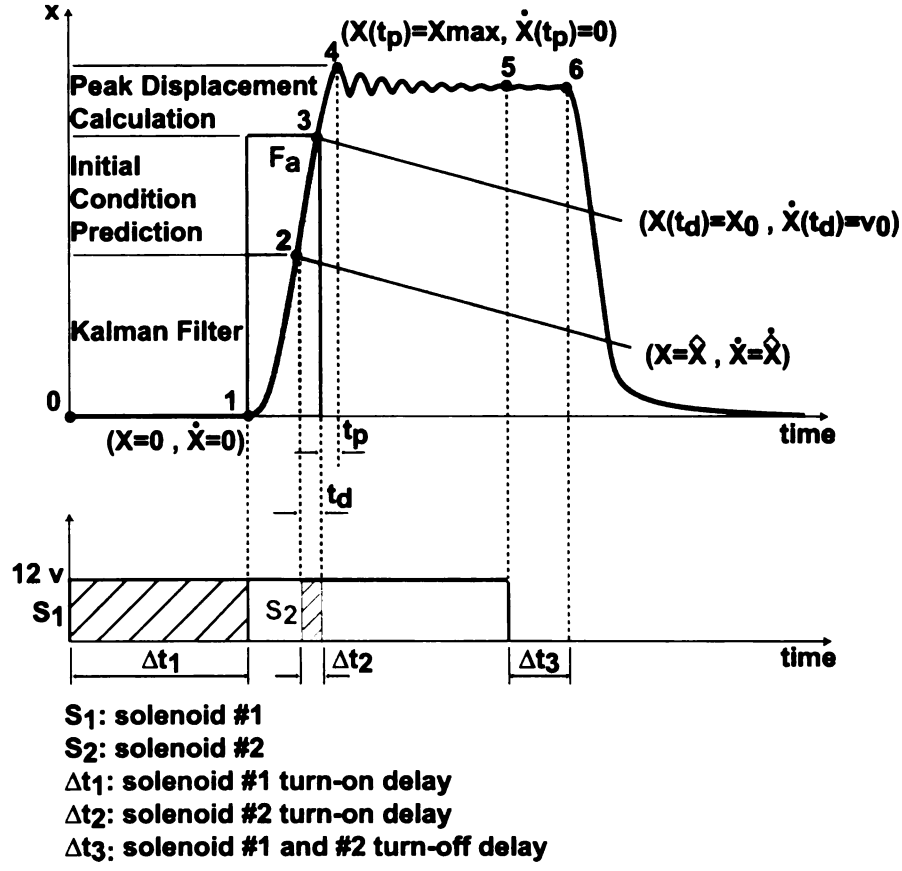

Figure 4.6. Exhaust valve lift control strategy

the calculated peak displacement is greater than or equal to the reference valve lift, solenoid #2 is activated, otherwise, the process repeats until the condition is satisfied. The details of the derivations are discussed in the following four subsections.

4.3.1 Peak Displacement Calculation (PDC)

This section describes the solution for the peak displacement at point 4 based on the initial conditions at point 3. Recall that the governing equation of the exhaust valve at the opening stage is presented in Equation (4.1). The back pressure force $F_b(x)$ equals the product of the exhaust valve area and the modeled in-cylinder pressure. The in-cylinder pressure used in the control algorithm development here is piece-wisely linearized according to the simulated in-cylinder pressure against EPVA exhaust valve profile as shown in Figure 4.8, where $F_b(x) = px + q$ ($p \leq 0$ and $q > 0$) with

$$\begin{cases} p = p_1,\ q = q_1,\ x \leq 0.002m \\ p = p_2,\ q = q_2,\ 0.002m < x \leq 0.008m \\ p = p_3,\ q = q_3,\ x > 0.008m \end{cases}$$

Substituting $F_b(x)$ with its linearized expression in Equation (4.1) results in Equation (4.10) below.

$$M\ddot{x} + C_f\dot{x} + K_p x = F_a - (px + q) - K_p\delta_p \tag{4.10}$$

Move the px term to the left resulting in Equation (4.11):

$$M\ddot{x} + C_f\dot{x} + (K_p + p)x = F_a - q - K_p\delta_p \tag{4.11}$$

Let $K = K_p + p$ and $F_a = 0$ since it is assumed that input force F_a is turned off to obtain Equation (4.12) in a general format given the initial condition $x(0) = x_0$, $\dot{x}(0) = v_0$.

$$M\ddot{x} + C_f\dot{x} + Kx = -Q,\ Q = K_p\delta_p + q \tag{4.12}$$

Recall that p takes three different values, p_1, p_2 and p_3 in three valve displacement regions. K could be either negative, zero or positive depending on the value of p. When K is positive, Equation (4.12) can be rewritten into Equation (4.13) as below:

$$\ddot{x} + 2\zeta\omega_n\dot{x} + \omega_n^2 x = -\frac{Q}{M} \tag{4.13}$$

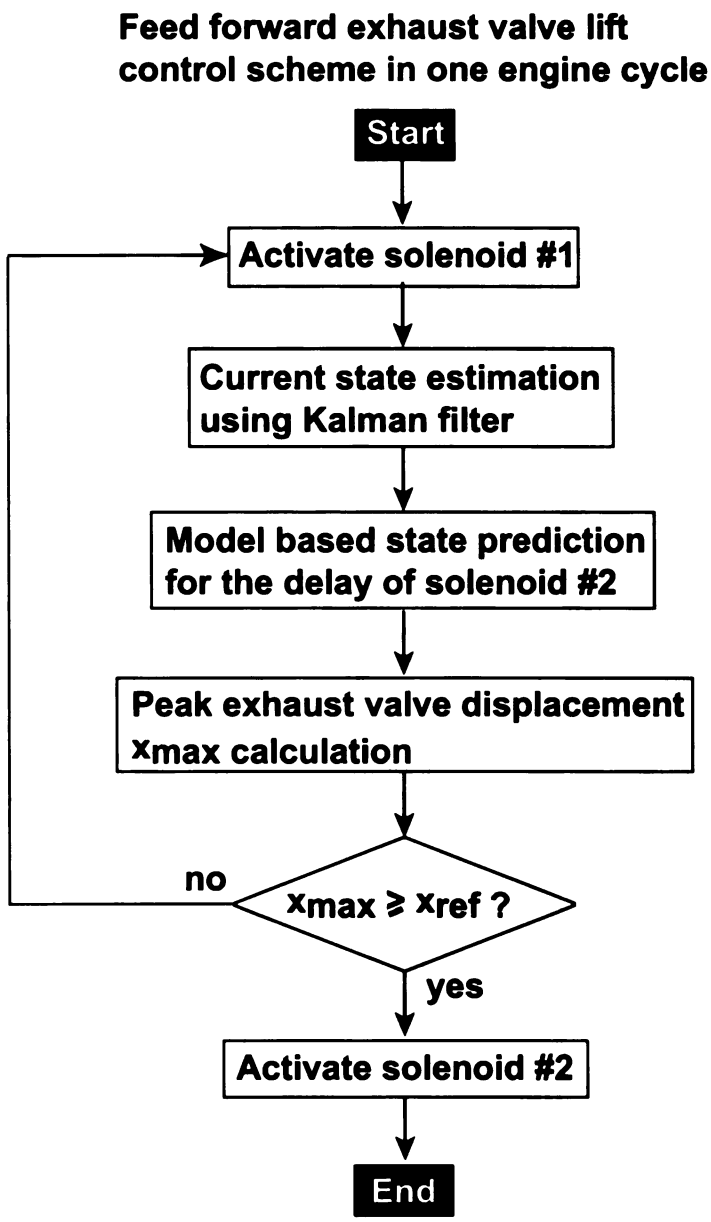

Figure 4.7. Feedforward exhaust valve lift control strategy

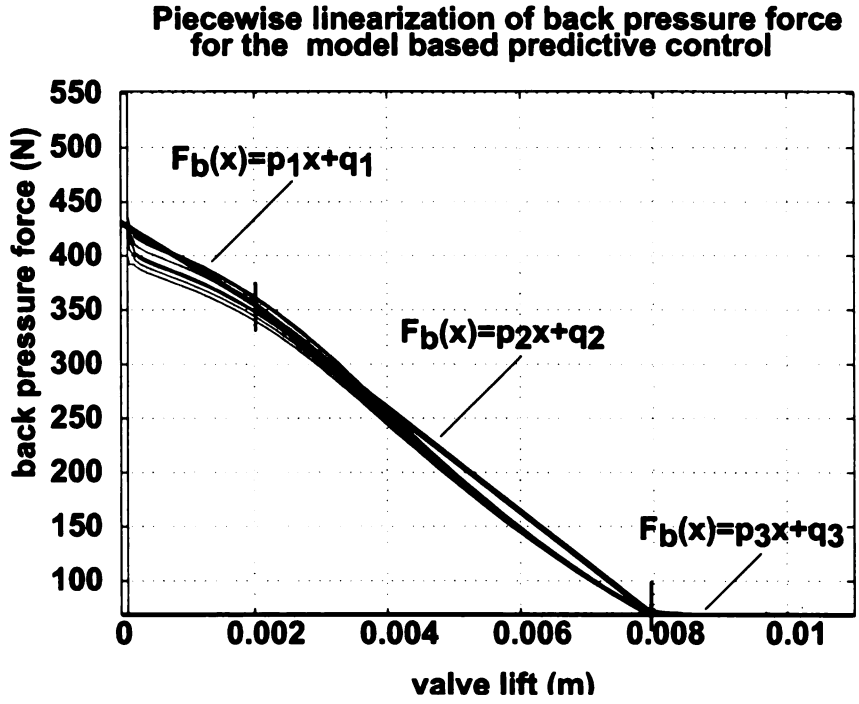

Figure 4.8. Piecewise linearization of in-cylinder pressure

where $\omega_n = \sqrt{\frac{K}{M}}$ and $\zeta = \frac{C_f}{2}\sqrt{\frac{1}{MK}}$. In this case, the solution can be categorized into under damped, critically damped and over damped scenarios depending on the value damping ratio ζ, damping coefficient C_f, mass M and equivalent stiffness K in Equation (4.13). The peak displacement solution derivation of Equation (4.12) proceeds separately in four cases. Case #1 is $K > 0$ with $0 < \zeta < 1$, case #2 is $K > 0$ with $\zeta = 1$, case #3 is $K > 0$ with $\zeta > 1$ and case #4 is $K \leq 0$. The initial condition denoted as $x(0) = x_0$ and $\dot{x}(0) = v_0$ in this section are derived in the next section of model based initial condition prediction.

PDC case #1 $K > 0$ with $0 < \zeta < 1$ (under damped)

We start with solving Equation (4.13) for all three cases where $K > 0$. The homogenous solution x_h can be expressed in Equation (4.14)

$$x_h = e^{-\zeta\omega_n t}(a_1 e^{i\omega_d t} + a_2 e^{-i\omega_d t}),\ \omega_d = \sqrt{1-\zeta^2}\omega_n \tag{4.14}$$

Solving for the particular solution x_p of Equation (4.13) results in Equation (4.15)

$$x_p = -\frac{Q}{K} \tag{4.15}$$

The complete solution $x(t) = x_p(t) + x_h(t)$ can be expressed in Equation (4.16).

$$x(t) = e^{-\zeta\omega_n t}(a_1 e^{i\omega_d t} + a_2 e^{-i\omega_d t}) - \frac{Q}{K}$$

Applying Euler formula $e^{i\alpha} = cos(\alpha) + isin(\alpha)$ and trigonometric identities to the equation above to obtain Equation (4.16)

$$x(t) = Ae^{-\zeta\omega_n t}\sin(\omega_d t + \theta) - \frac{Q}{K} \tag{4.16}$$

where A and θ are determined by the initial conditions as follows:

$$\begin{cases} x(0) = A\sin(\theta) - \frac{Q}{K} = x_0 \\ \dot{x}(0) = -\zeta A\omega_n \sin(\theta) + \omega_d A\cos(\theta) = v_0 \end{cases}$$

$$\begin{cases} A = \sqrt{\frac{(v_0+\zeta\omega_n\chi_0)^2+\chi_0^2\omega_d^2}{\omega_d^2}},\ \chi_0 = x_0 + \frac{Q}{K} \\ \theta = tan^{-1}(\frac{\omega_d\chi_0}{v_0+\zeta\omega_n\chi_0}) \end{cases}$$

The peak displacement $x_p = x(t_p)$ is solved at $\dot{x}(t_p) = 0$ with t_p being the time the valve takes to travel to its maximum displacement (see Figure 4.6). Taking the time derivative of $x(t)$ and setting it to zero at t_p result in Equation (4.17).

$$\dot{x}(t_p) = -\zeta\omega_n A e^{-\zeta\omega_n t_p} \sin(\omega_d t_p + \theta) = 0 \tag{4.17}$$

Solving Equation (4.17) yields:

$$t_p = \begin{cases} \frac{1}{\omega_d}\left(tan^{-1}\left(\sqrt{\frac{1}{\zeta^2} - 1}\right) - \theta\right), & tan^{-1}\sqrt{\frac{1}{\zeta^2} - 1} > \theta \\ \frac{1}{\omega_d}\left(tan^{-1}\left(\sqrt{\frac{1}{\zeta^2} - 1}\right) - \theta + 2\pi\right), & otherwise \end{cases}$$

Substituting t_p into Equation (4.16), we obtain the peak displacement $x(t_p)$. The solution of the peak displacement is summarized below:

PDC Summary $K > 0$ with $0 < \zeta < 1$
$x(t_p) = Ae^{-\zeta\omega_n t_f} \sin(\omega_d t_p + \theta) - \frac{Q}{K}$
$Q = K_p\delta_p + q,\ K = K_p + p,\ \theta = tan^{-1}\left(\frac{\omega_d x_0}{v_0 + \zeta\omega_n x_0}\right)$
$t_p = \begin{cases} \frac{1}{\omega_d}\left(tan^{-1}\left(\sqrt{\frac{1}{\zeta^2} - 1}\right) - \theta\right), & tan^{-1}\sqrt{\frac{1}{\zeta^2} - 1} > \theta \\ \frac{1}{\omega_d}\left(tan^{-1}\left(\sqrt{\frac{1}{\zeta^2} - 1}\right) - \theta + 2\pi\right), & otherwise \end{cases}$
$A = \sqrt{\frac{(v_0 + \zeta\omega_n x_0)^2 + x_0^2\omega_d^2}{\omega_d^2}},\ x_0 = x_0 + \frac{Q}{K}$
$\omega_n = \sqrt{\frac{K}{M}},\ \zeta = \frac{C_f}{2}\sqrt{\frac{1}{MK}},\ \omega_d = \sqrt{1 - \zeta^2}\omega_n$
$x_0 = x(t_d),\ v_0 = \dot{x}(t_d)$
$x(t_d)$ and $\dot{x}(t_d)$ obtained from model based initial condition prediction

PDC case #2 $K > 0$ with $\zeta = 1$ (critically damped)

Again, the homogenous solution x_h and non-homogenous solution x_p are shown below.

$$x_h(t) = (a_1 + a_2 t)e^{-\omega_n t} \tag{4.18}$$

$$x_p = -\frac{Q}{K} \tag{4.19}$$

The total solution is

$$x(t) = x_h(t) + x_p(t) = (a_1 + a_2 t)e^{-\omega_n t} - \frac{Q}{K} \tag{4.20}$$

where a_1 and a_2 below are obtained by evaluating the above equation at the initial conditions $x(0) = x_0$, $\dot{x}(0) = v_0$.

$$\begin{cases} a_1 = x_0 + \frac{Q}{K} \\ a_2 = v_0 + \omega_n(x_0 + \frac{Q}{K}) \end{cases}$$

Similarly, we solve for t_p and $x(t_p)$ at $\dot{x}(t_p) = 0$. The expression of peak displacement $x(t_p)$ is summarized below:

PDC Summary $K > 0$ with $\zeta = 1$
$x(t_p) = (a_1 + a_2 t_p)e^{-\omega_n t_p} - \frac{Q}{K}$
$Q = K_p\delta_p + q, \quad K = K_p + p, \; t_p = \frac{a_2 - \omega_n a_1}{\omega_n a_2}$
$a_1 = x_0 + \frac{Q}{K}, \; a_2 = v_0 + \omega_n(x_0 + \frac{Q}{K}), \; \omega_n = \sqrt{\frac{K}{M}}$
$x_0 = x(t_d), \; v_0 = \dot{x}(t_d)$
$x(t_d)$ and $\dot{x}(t_d)$ obtained from
model based initial condition prediction

PDC case #3 $K > 0$ with $\zeta > 1$ (over damped)

The homogeneous and non-homogeneous solutions of Equation (4.13) in this case takes the following form,

$$x_h(t) = a_1 e^{\lambda_1 t} + a_2 e^{\lambda_2 t}$$

where $\lambda_1 = -\zeta\omega_n - \omega_n\sqrt{\zeta^2 - 1}$ and $\lambda_2 = -\zeta\omega_n + \omega_n\sqrt{\zeta^2 - 1}$,

$$x_p = -\frac{Q}{K}. \tag{4.21}$$

The total solution is shown in Equation (4.22)

$$x(t) = x_h(t) + x_p(t) = a_1 e^{\lambda_1 t} + a_2 e^{\lambda_2 t} - \frac{Q}{K} \tag{4.22}$$

Evaluating the total solution at the initial conditions $x(0) = x_0$, $\dot{x}(0) = v_0$ results in a_1 and a_2 as below:

$$\begin{cases} a_1 = \frac{-v_0 + (-\zeta + \sqrt{\zeta^2 - 1})\omega_n x_0}{2\omega_n\sqrt{\zeta^2 - 1}} \\ a_2 = \frac{v_0 + (\zeta + \sqrt{\zeta^2 - 1})\omega_n x_0}{2\omega_n\sqrt{\zeta^2 - 1}} \end{cases}$$

Solve for t_p at $\dot{x}(t_p) = 0$ to obtain:

$$t_p = \begin{cases} \frac{1}{\lambda_2 - \lambda_1} \ln \frac{-\lambda_1 a_1}{\lambda_2 a_2}, & a_1 a_2 \lambda_1 \lambda_2 < 0 \\ no \quad solution, & \text{otherwise} \end{cases}$$

Evaluate $x(t)$ at t_p to obtain the peak displacement $x(t_p)$. The solutions are summarized below:

PDC Summary $K > 0$ with $\zeta > 1$
$x(t_p) = a_1 e^{\lambda_1 t_p} + a_2 e^{\lambda_2 t_p} - \frac{Q}{K}$
$Q = K_p \delta_p + q, \quad K = K_p + p$
$t_p = \begin{cases} \frac{1}{\lambda_2 - \lambda_1} \ln \frac{-\lambda_1 a_1}{\lambda_2 a_2}, & a_1 a_2 \lambda_1 \lambda_2 < 0 \\ no \quad solution, & \text{otherwise} \end{cases}$
$a_1 = \frac{-v_0 + (-\zeta + \sqrt{\zeta^2 - 1})\omega_n x_0}{2\omega_n \sqrt{\zeta^2 - 1}}, \; a_2 = \frac{v_0 + (\zeta + \sqrt{\zeta^2 - 1})\omega_n x_0}{2\omega_n \sqrt{\zeta^2 - 1}}$
$\lambda_1 = -\zeta\omega_n - \omega_n \sqrt{\zeta^2 - 1}, \; \lambda_2 = -\zeta\omega_n + \omega_n \sqrt{\zeta^2 - 1}$
$\omega_n = \sqrt{\frac{K}{M}}, \; \zeta = \frac{C_f}{2} \sqrt{\frac{1}{MK}}$
$x_0 = x(t_d), \; v_0 = \dot{x}(t_d)$
$x(t_d)$ and $\dot{x}(t_d)$ obtained from
model based initial condition prediction

PDC case #4 $K \leq 0$

The homogeneous and non-homogeneous solutions of Equation (4.13) with $K \leq 0$ takes the form in Equations (4.23) and (4.23).

$$x_h(t) = a_1 e^{\lambda_1 t} + a_2 e^{\lambda_2 t},$$

where $\lambda_1 = \frac{-C_f + \sqrt{C_f^2 - 4MK}}{2M}$ and $\lambda_2 = \frac{-C_f + \sqrt{C_f^2 - 4MK}}{2M}$ with $c^2 - 4KM > 0$ since $K \leq 0$.

$$x_p = -\frac{Q}{K}. \tag{4.23}$$

The complete solution is expressed in Equation (4.24). The coefficients a_1 and a_2 are provided in Equation (4.25) by evaluating Equation (4.24) at the initial conditions $x(0) = x_0$, $\dot{x}(0) = v_0$.

$$x(t) = x_h(t) + x_p(t) = a_1 e^{\lambda_1 t} + a_2 e^{\lambda_2 t} - \frac{Q}{K} \tag{4.24}$$

$$a_1 = \frac{\lambda_2 \chi_0 - v_0}{\lambda_2 - \lambda_1},\ a_2 = \frac{v_0 - \lambda_1 \chi_0}{\lambda_2 - \lambda_1}\ with\ \chi_0 = x_0 + \frac{Q}{K} \tag{4.25}$$

Similarly, solve for t_p below at $\dot{x}(t_p) = 0$:

$$t_p = \begin{cases} \frac{1}{\lambda_2 - \lambda_1} \ln \frac{-\lambda_1 a_1}{\lambda_2 a_2}, & a_1 a_2 \lambda_1 \lambda_2 < 0 \\ no\ \ solution, & \text{otherwise} \end{cases}$$

Substitute the above solution into Equation (4.24) to obtain the peak displacement $x(t_p)$ which is summarized below:

PDC Summary $K < 0$
$x(t_p) = a_1 e^{\lambda_1 t_p} + a_2 e^{\lambda_2 t_p} - \frac{Q}{K}$
$Q = K_p \delta_p + q,\ \ K = K_p + p$
$t_p = \begin{cases} \frac{1}{\lambda_2 - \lambda_1} \ln \frac{-\lambda_1 a_1}{\lambda_2 a_2}, & a_1 a_2 \lambda_1 \lambda_2 < 0 \\ no\ \ solution, & \text{otherwise} \end{cases}$
$a_1 = \frac{\lambda_2 \chi_0 - v_0}{\lambda_2 - \lambda_1},\ a_2 = \frac{v_0 - \lambda_1 \chi_0}{\lambda_2 - \lambda_1},\ \chi_0 = x_0 + \frac{Q}{K}$
$\lambda_1 = \frac{-C_f + \sqrt{C_f^2 - 4MK}}{2M},\ \lambda_2 = \frac{-C_f - \sqrt{C_f^2 - 4MK}}{2M}$
$\omega_n = \sqrt{\frac{K}{M}},\ \zeta = \frac{C_f}{2}\sqrt{\frac{1}{MK}}$
$x_0 = x(t_d),\ v_0 = \dot{x}(t_d)$
$x(t_d)$ and $\dot{x}(t_d)$ obtained from model based initial condition prediction

4.3.2 Model Based Initial Condition Prediction (ICP)

The previous section solves for the peak displacement $x(t_p)$ using the displacement and velocity at point 3 as initial conditions (Figure 4.6). This section derives the formulas to predict the displacement $x(t_d)$ and velocity $\dot{x}(t_d)$ at point 3, given the displacement and velocity at point 2. The displacement and velocity at point 2 are initial conditions denoted as $x(0) = x_0$ and $\dot{x}(0) = v_0$ in this section. Their values are estimated by the Kalman state estimation described in the next subsection. Solenoid #2 delay, Δt_2, is the time input and F_a is a constant force input between points 2 and 3. Consider the governing equation again in Equation (4.1). Given $F_b(x) = px + q$, Equation (4.1) becomes

$$M\ddot{x} + C_f \dot{x} + K_p x = F_a - (px + q) - K_p \delta_p \tag{4.26}$$

Rearrange the equation above to obtain

$$M\ddot{x} + C_f\dot{x} + (K_p + p)x = F_a - q - K_p\delta_p \tag{4.27}$$

Let $K = K_p + p$ and $W = q + K_p\delta_p - F_a$, Equation (4.27) becomes Equation (4.28).

$$M\ddot{x} + C_f\dot{x} + Kx = -W \tag{4.28}$$

It is clear that Equations (4.12) and (4.28) have the same form. Previously, Equation (4.12) was evaluated for the maximum displacement given initial conditions. Now, Equation (4.28) is evaluated for the displacement and velocity in t_d amount of time given initial conditions, where $t_d = \Delta t_2$ (see Figure 4.6). The displacement solutions of Equation (4.28) are the same as those of Equation (4.12) by replacing Q with W. The time derivative of the displacement yields the solution of the valve velocity. Similarly, the solutions can be categorized into four cases. They are under damped, critically damped and over damped with $K > 0$ and $K \leq 0$. The solutions are summarized case by case in the following subsections.

ICP case #1 $K > 0$ with $0 < \zeta < 1$ (under damped)

ICP Summary $K > 0$ with $0 < \zeta < 1$
$x(t_d) = Ae^{-\zeta\omega_n t_d}\sin(\omega_d t_d + \theta) - \frac{W}{K}$
$\dot{x}(t_d) = -\zeta\omega_n Ae^{-\zeta\omega_n t_d}\sin(\omega_d t_d + \theta)$
$+A\omega_d e^{-\zeta\omega_n t_d}\cos(\omega_d t_d + \theta)$
$W = q + K_p\delta_p - F_a, \quad K = K_p + p$
$A = \sqrt{\frac{(v_0+\zeta\omega_n x_0)^2 + x_0^2\omega_d^2}{\omega_d^2}}, \ \theta = -tan^{-1}(\frac{\omega_d x_0}{v_0+\zeta\omega_n x_0})$
$x_0 = x_0 + \frac{W}{K}$
$\omega_n = \sqrt{\frac{K}{M}}, \ \zeta = \frac{C_f}{2}\sqrt{\frac{1}{MK}}, \ \omega_d = \sqrt{1-\zeta^2}\omega_n$
$x_0 = \hat{x}, \ v_0 = \dot{\hat{x}}$
$\hat{x}$ and $\dot{\hat{x}}$ obtained from Kalman filter state estimation

ICP case #2 $K > 0$ with $\zeta = 1$ (critically damped)

ICP Summary $K > 0$ with $\zeta = 1$
$x(t_d) = (a_1 + a_2 t_d)e^{-\omega_n t_d} - \frac{W}{K}$
$\dot{x}(t_d) = a_2 e^{-\omega_n t_d} - (a_1 + a_2 t_d)\omega_n e^{-\omega_n t_d}$
$W = q + K_p \delta_p - F_a, \quad K = K_p + p$
$a_1 = x_0 + \frac{W}{K}, \; a_2 = v_0 + \omega_n(x_0 + \frac{W}{K}), \; \omega_n = \sqrt{\frac{K}{M}}$
$x_0 = \widehat{x}, \; v_0 = \dot{\widehat{x}}$
$\widehat{x}$ and $\dot{\widehat{x}}$ obtained from Kalman filter state estimation

ICP case #3 $K > 0$ with $\zeta > 1$ (over damped)

ICP Summary $K > 0$ with $\zeta > 1$
$x(t_d) = a_1 e^{\lambda_1 t_d} + a_2 e^{\lambda_2 t_d} - \frac{W}{K}$
$\dot{x}(t_d) = a_1 \lambda_1 e^{\lambda_1 t_d} + a_2 \lambda_2 e^{\lambda_2 t_d}$
$W = q + K_p \delta_p - F_a, \quad K = K_p + p$
$a_1 = \frac{-v_0 + (-\zeta + \sqrt{\zeta^2 - 1})\omega_n x_0}{2\omega_n \sqrt{\zeta^2 - 1}}, \; a_2 = \frac{v_0 + (\zeta + \sqrt{\zeta^2 - 1})\omega_n x_0}{2\omega_n \sqrt{\zeta^2 - 1}}$
$\lambda_1 = -\zeta\omega_n - \omega_n\sqrt{\zeta^2 - 1}, \; \lambda_2 = -\zeta\omega_n + \omega_n\sqrt{\zeta^2 - 1}$
$\omega_n = \sqrt{\frac{K}{M}}, \; \zeta = \frac{C_f}{2}\sqrt{\frac{1}{MK}}$
$x_0 = \widehat{x}, \; v_0 = \dot{\widehat{x}}$
$\widehat{x}$ and $\dot{\widehat{x}}$ obtained from Kalman filter state estimation

ICP case #4 $K \leq 0$

ICP Summary $K \leq 0$
$x(t_d) = a_1 e^{\lambda_1 t_d} + a_2 e^{\lambda_2 t_d} - \frac{W}{K}$
$\dot{x}(t_d) = a_1 \lambda_1 e^{\lambda_1 t_d} + a_2 \lambda_2 e^{\lambda_2 t_d}$
$W = q + K_p \delta_p - F_a, \quad K = K_p + p$
$a_1 = \frac{\lambda_2 \chi_0 - v_0}{\lambda_2 - \lambda_1}, \; a_2 = \frac{v_0 - \lambda_1 \chi_0}{\lambda_2 - \lambda_1}$
$\lambda_1 = \frac{-C_f + \sqrt{C_f^2 - 4MK}}{2M}, \; \lambda_2 = \frac{-C_f - \sqrt{C_f^2 - 4MK}}{2M}$
$\chi_0 = x_0 + \frac{W}{K}, \; \omega_n = \sqrt{\frac{K}{M}}, \; \zeta = \frac{C_f}{2}\sqrt{\frac{1}{MK}}$
$x_0 = \widehat{x}, \; v_0 = \dot{\widehat{x}}$
$\widehat{x}$ and $\dot{\widehat{x}}$ obtained from Kalman filter state estimation

4.3.3 Kalman Filter State Estimation (KFE)

The displacement and velocity at point 2 (see Figure 4.6) are needed as initial conditions in the previous section. The system is equipped with a displacement sensor which measures the exhaust valve displacement. The velocity obtained through taking a time derivative of the measured displacement is unreliable due to the measurement noise. The observer formulated in this section performs the optimal estimations of both the displacement and velocity at point 2 in the presence of noise using Kalman state estimator. The estimated displacement and velocity are denoted as $\hat{x}$ and $\dot{\hat{x}}$ respectively. The state space notation of the system is expressed below:

$$\begin{aligned} \dot{x} &= Ax + Bu + Gw(t) \\ y &= Cx + v(t) \end{aligned}$$

where $A = \begin{bmatrix} 0 & 1 \\ \frac{-K}{M} & \frac{-C_f}{M} \end{bmatrix}$, $B = \begin{bmatrix} 0 \\ 1 \end{bmatrix}$, $C = \begin{bmatrix} 1 & 0 \end{bmatrix}$ and $x = \begin{bmatrix} x_1 \\ x_2 \end{bmatrix}$; $w(t)$ and $v(t)$ represent the process noise and measurement noise. Note that $u = -W$ is the input to the system, $x_1 = x$ and $x_2 = \hat{x}$ are the states representing the valve displacement and velocity. The Kalman state estimator takes the following forms:

$$\begin{aligned} \dot{\hat{x}} &= A\hat{x} + Bu + L(y - c\hat{x}) \\ y &= C\hat{x}, \quad \hat{x}(0) = 0 \end{aligned}$$

where $L = \begin{bmatrix} l_1 \\ l_2 \end{bmatrix}$ is the observer gain acquired through solving the Algebraic Riccati Equation (4.29) and Equation (4.30); and $\hat{x} = \begin{bmatrix} \hat{x}_1 \\ \hat{x}_2 \end{bmatrix}$ contains the estimated states with $\hat{x}_1$ and $\hat{x}_2$ being the estimated displacement and velocity. Note that G is considered as an identity matrix.

$$AP + PA^T + GWG^T - PC^TV^{-1}CP = 0 \tag{4.29}$$

$$W \geq 0 \ \textit{and} \ V > 0$$

where W and V are covariance matrices of w and v, respectively. If (C, A) is observable, the Algebraic Riccati Equation has a unique positive definite solution P, and the estimated

state $\hat{x}$ asymptotically approaches true state x using L given by Equation (4.30).

$$L = PC^T V^{-1} \tag{4.30}$$

The estimator is summarized below with obtained l_1 and l_2:

Kalman filter state estimation summary
$\dot{\hat{x}}_1 = \hat{x}_2 + l_1(x_1 - \hat{x}_1)$
$\dot{\hat{x}}_2 = -\frac{K}{M}\hat{x}_1 - \frac{C_f}{M}\hat{x}_2 + \frac{u}{M} + l_2(x_1 - \hat{x}_1)$
$K = K_p + p, \;\; u = F_a - q - K_p\delta_p$

4.3.4 Closed-Loop Control Scheme

The feedforward solution of solenoid #2 activation timing is obtained by implementing the formulas from the peak displacement calculation, model based initial condition prediction and Kalman filter state estimation subsections. This solution combined with the displacement error compensation from the proportional and integrator (PI) feedback scheme forms a closed-loop control signal of solenoid #2 as illustrated in Figure 4.9.

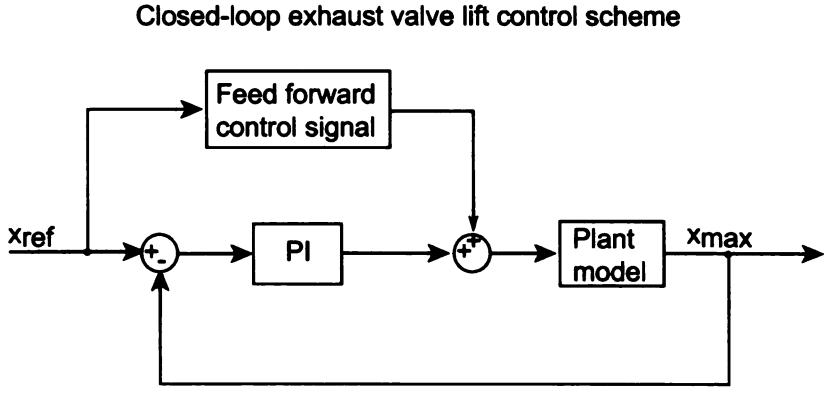

Figure 4.9. Closed-loop exhaust valve lift control scheme

4.4 Simulation Result

The developed control algorithms are validated by simulation using the combined valve actuator and the in-cylinder pressure model as the plant model. The three segments of the feedforward control strategy and the closed-loop control scheme are evaluated in sequence.

4.4.1 Simulation of Peak Displacement Calculation

Figure 4.10 demonstrates the simulation results in four out of 80 cycles where the solenoid #2 is activated when the calculated peak displacement reaches the reference valve peak lift of $11mm$. This tests the open loop feedforward peak displacement calculation algorithm. The model valve displacement and velocity are employed as the known initial condition in this simulation. The top diagram shows that the peak valve lift is maintained at $11mm$, rejecting the in-cylinder pressure variation at the back of the exhaust valve (shown in the bottom diagram) when the feedforward peak displacement calculation is applied.

4.4.2 Simulation of Model Based Initial Condition Prediction

Figure 4.11 presents the simulation results of the model based displacement prediction. The solenoid #2 delay (Δt_2 or t_d) is assumed to be $2ms$ in the simulation. White noise is injected to the plant displacement output to simulate the measurement noise. The plant displacement (solid) without measurement noise injected and the predicted displacement (dash) in the prediction active region are displayed in the top diagram for one cycle. The middle diagram displays the error between the two. The bottom diagram shows the error between the plant and predicted displacement of 80 cycles closed-loop lift tracking simulation with lift set points of $11mm$, $6mm$, $8mm$ and again $11mm$. The absolute error is less than $0.7mm$. The simulation results of the model based velocity prediction are shown in Figure 4.12. The absolute error between the plant and predicted velocity is less than $0.25m/s$ in all 80 cycles simulated using the closed-loop lift tracking control with four lift set points.

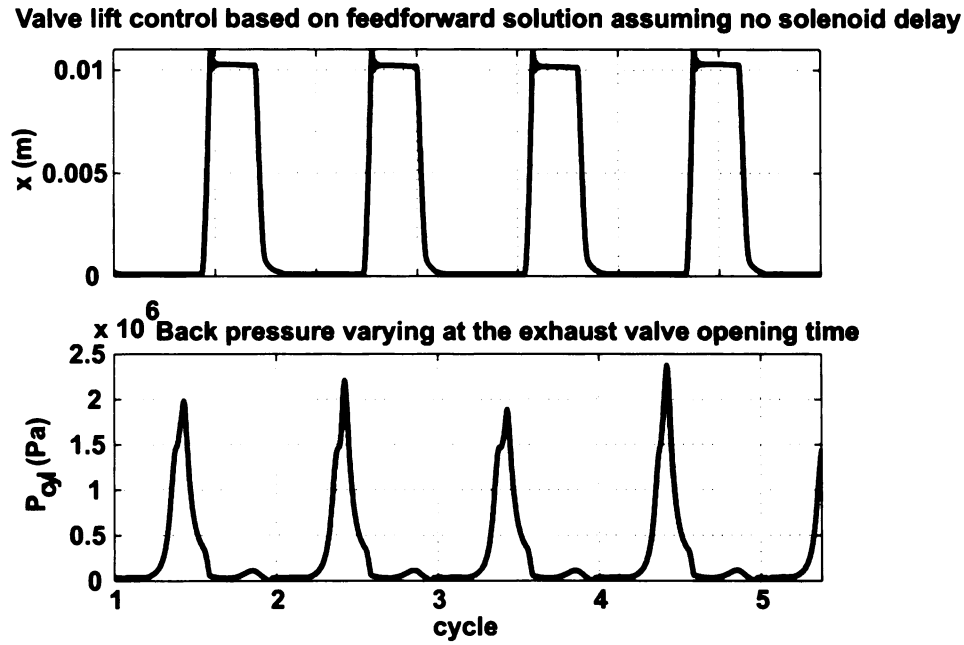

Figure 4.10. Simulation validation of feedforward solution without considering solenoid #2 delay

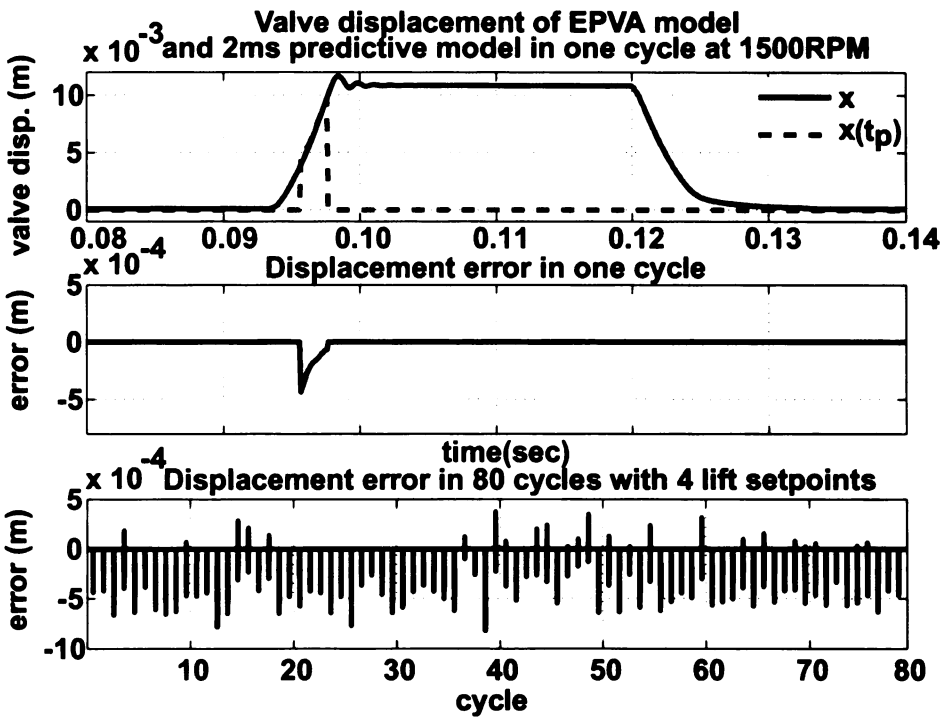

Figure 4.11. Simulation validation of displacement prediction x_{0_p}

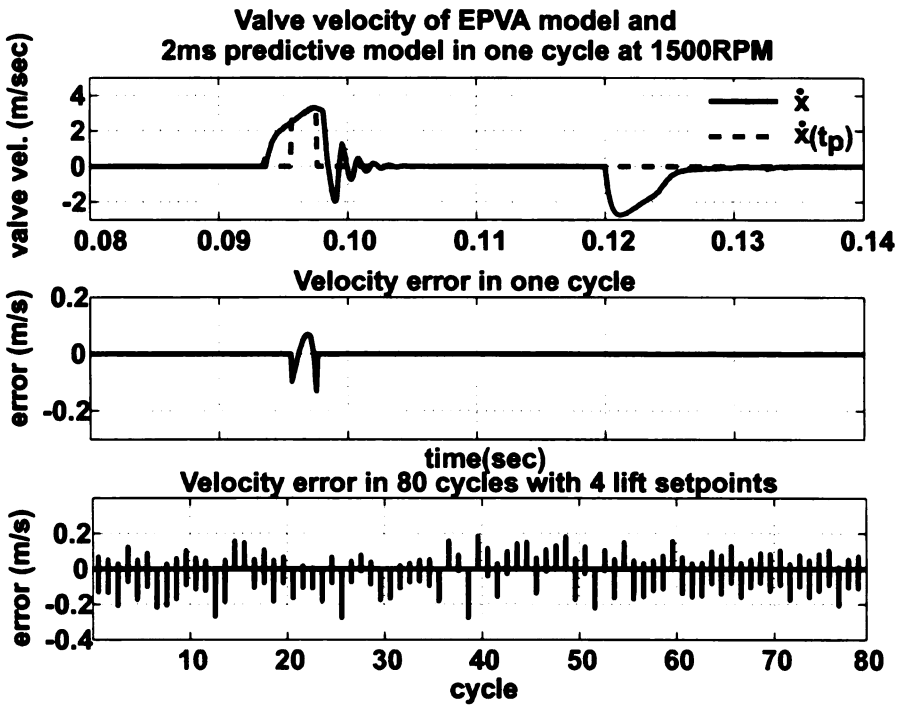

Figure 4.12. Simulation validation of velocity prediction $\dot{x}_{0_p}$

4.4.3 Simulation of Kalman Filter State Estimation

Figure 4.13 displays a simulated valve displacement output with white noise measurement. Figure 4.14 and Figure 4.15 present the simulation results of the Kalman filter state estima-

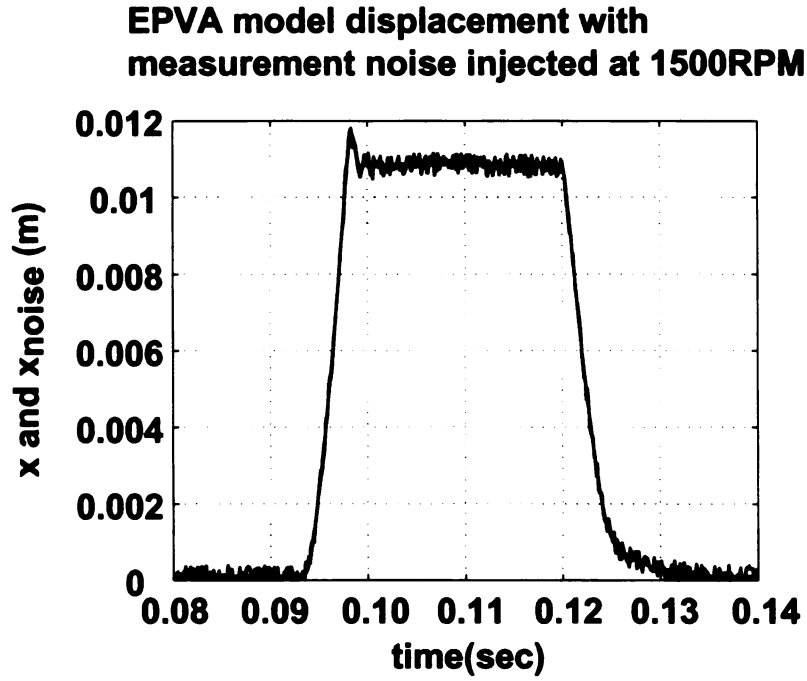

Figure 4.13. Model displacement with measurement noise injected

tion with the measurement noise in presence. The absolute error between the displacements of the plant (without measurement noise) and the Kalman estimator is less than $0.3mm$. The absolute error between the plant velocity (without measurement noise) and the estimated velocity is less than $0.38m/s$. These comparison were accomplished in 80 cycle simulation using the closed-loop lift tracking control with four lift set points.

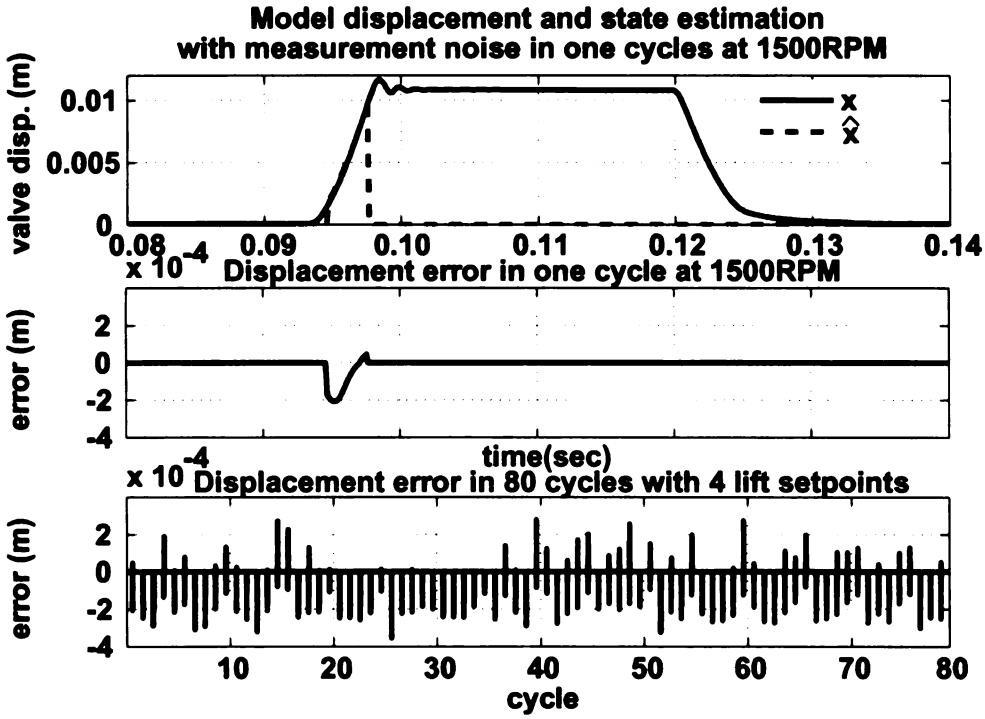

Figure 4.14. Simulation validation of kalman filter displacement estimation $\widehat{x}_0$ with measurement noise

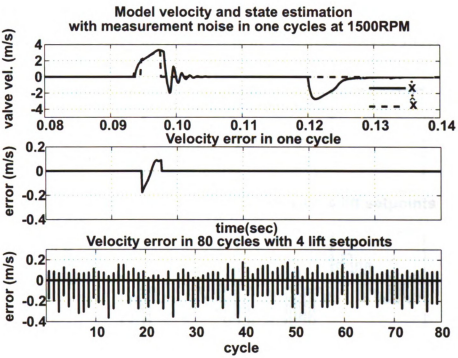

Figure 4.15. Simulation validation of Kalman filister velocity estimation $\widehat{x}_0$ with measurement noise

4.4.4 Simulation of Closed-Loop Exhaust Valve Lift Tracking

Finally, Figure 4.16 presents the entire closed-loop lift tracking simulation result with all three feedforward control sequences assembled at four reference lift set points in the presence of measurement noise. The dark and grey lines in the top diagram represent the reference and model valve lift respectively. The bottom diagram demonstrates that the absolute lift tracking error is below $0.6mm$ at steady state. The exhaust valve tracks the reference lift within a single engine cycle having the lift error less than $0.5mm$.

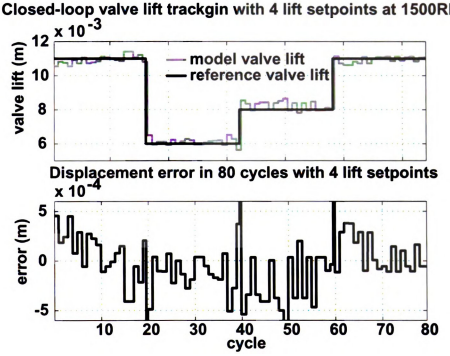

Figure 4.16. Simulation validation of closed-loop exhaust valve lift tracking control system with four set points

4.5 Real Time Exhaust Valve Lift Control Algorithm

In this section, the closed-loop lift control strategy was evaluated by experiments. The feedforward lift control inputs were calculated before the real time implementation to save the real time throughput. The damping ratio of the exhaust valve model at the opening stage is need in constructing the feed forward lift control signal using the developed model based predictive lift control strategy. To identify this model parameter, the open loop lift control tests were conducted on the exhaust valve at $600RPM$. The maximum pressure at the back of exhaust valve was set to be $60psi$, the supply air and oil pressure was $120psi$ and the target lift was $10mm$. The valve back pressure varies randomly from cycle to cycle with the variation as large as $14.5psi$. The measured valve back pressure was used in the exhaust valve model simulation. The lag between the activation of two solenoids were kept the same in both the experiments and the simulations for parameter identification purpose. The experiment and simulation valve responses are displayed in Figure 4.17. The bottom diagram shows the model (dot line) and the measured (solid line) valve lift profiles in five cycles. The top diagram shows the corresponding pressure against with the exhaust valve opens. The damping ratio was chosen so that the model valve responses agree with the experimental valve responses as demonstrated in this figure.

The developed model based predictive control strategy can be used to seek the timing of activating the second solenoid and use this timing as a feedforward lift control input in real time. In order to reduce the real time computational throughput, the developed strategy was used to calculate the lag between the activation of the first and the second solenoid for different lift set points in simulation. In the real time application, this lag was the feedforward lift control input which was combined with the feed back PI compensation to form a closed-loop lift control input. The measured valve back pressure in the pressurized chamber was piecewisely linearized and used in the feedforward control input calculation. The measured pressure was multiplied by the area of the exhaust valve to obtain the pressure force acting on the back of the valve. This force were plotted in Figure 4.18 (grey

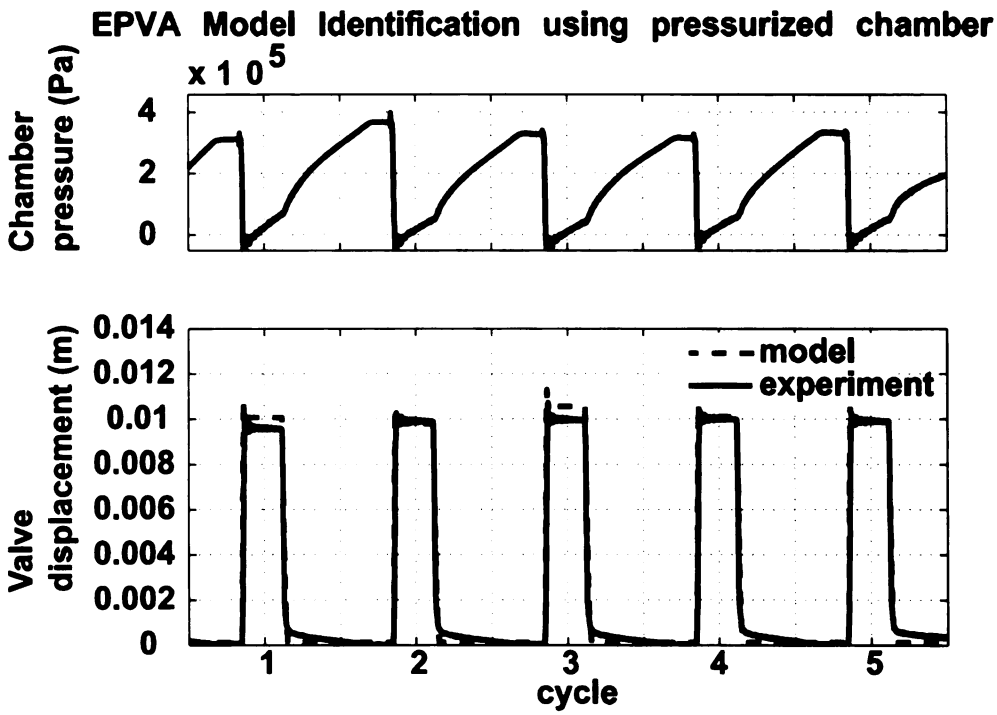

Figure 4.17. Exhaust valve model identification with measured randomly varying valve back pressure

curves) against the valve displacement for 20 cycles. As shown in this figure, they were linearized in three segments (solid lines) during the exhaust valve open to approximate the mean value of these forces. The coefficients, p_1, q_1, p_2, q_2, p_3 and q_3, were used to construct the feedforward lift control input through the model based predictive control algorithm. Simulations were performed to determine the lags between the activation of two solenoids according to the given reference lifts. The exhaust valve was identified earlier and used as the plant in the simulations. The measured back pressure at which the exhaust valve opens against was used to keep the configuration of the simulation consistent with that of the experiment. The results are displayed in Figure 4.19. The diagrams in the left column are the valve lift output from the exhaust valve model. Those in the right column are the calculated feedforward lift control inputs which are the calculated lags between the activation of the first and second solenoids. The lag was found to be about $3.8ms$ (top right), $4.1ms$ (middel right) and $4.8ms$ (bottom right) to achieve the target lift of $6mm$ (top left), $8mm$ (middle left) and $10mm$ (bottom left).

4.6 Conclusion

A mathematical exhaust valve actuator model and an in-cylinder pressure model have been developed for a model based predictive lift control for the exhaust valve. The exhaust valve model was approximated by a partially linearized second order spring-mass-damper system. The in-cylinder pressure was modeled during the exhaust valve opening stage. This model was integrated with the exhaust valve actuator model for control development. The thermodynamics data used in this model was obtained with the WAVE^{TM} simulation which was calibrated using experimental in-cylinder pressure data. The in-cylinder pressure model was validated using experimental data and demonstrates satisfactory model accuracy.

A model based predictive control strategy was developed for feedforward control. This strategy contains three segments; peak displacement calculation, model based initial condition prediction and Kalman state estimation. Simulations were carried out which includes

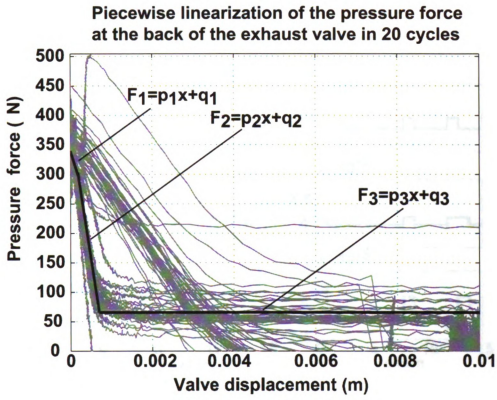

Figure 4.18. Piecewise linearization of the measured exhaust valve back pressure force

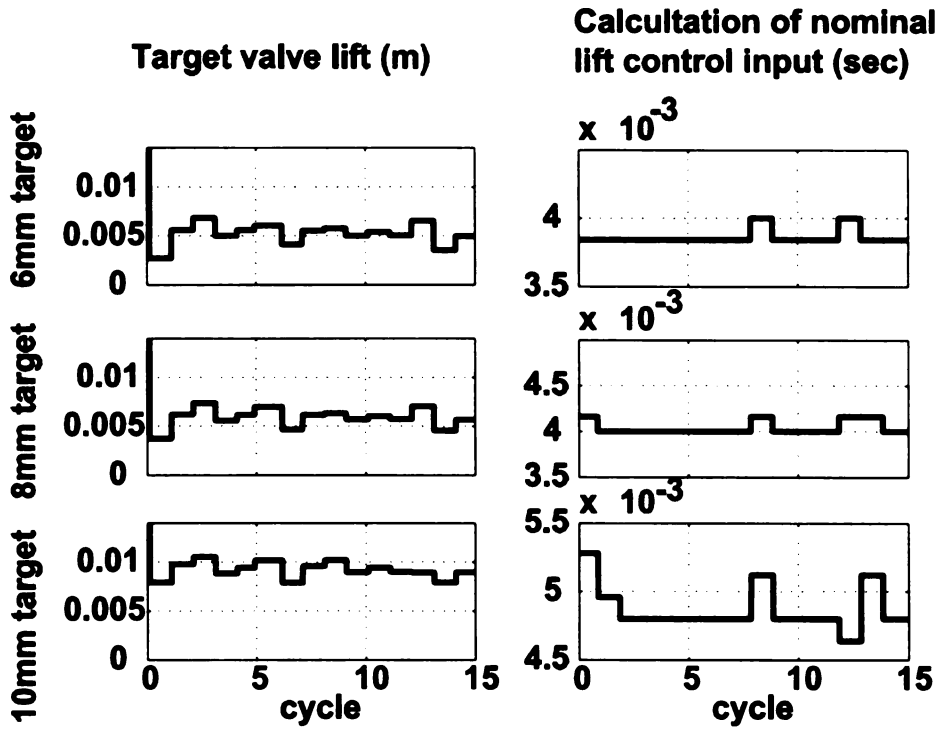

Figure 4.19. Calculation of the feedforward exhaust valve lift control inputs for three set points using the measured valve back pressure

the white noise at the measurement side to test the performance of every individual segment and the entire feedforward algorithm assembled from these segments. A proportional and integral controller was used for closed loop control. Combined with model based predictive feedforward control, the closed loop control system for valve lift was evaluated. This was accomplished by simulations using the developed exhaust valve and in-cylinder pressure models at different reference lift points and included measurement noise. The simulation results demonstrate that the steady state valve lift error is below $0.6mm$. The exhaust valve tracks the reference lift within a single engine cycle having a lift error less than $0.5mm$ in simulations. A real time closed-loop exhaust valve control algorithm is developed using the model based predictive control strategy. It will be evaluated by experiments in chapter 5.

CHAPTER 5

Experiment Implementation

5.1 Introduction

In the early chapters, valve actuator system models were created and the closed-loop control strategies for both intake and exhaust valves were developed and the lift control algorithms were validated by simulations. The valve timing control depends on the reliability of the lift control and the idea of timing control are similar as that of the lift control. Therefore, chapter 5 focuses on the experimental implementation and evaluation of the developed intake and exhaust valve lift control systems.

5.2 Experiment Setup

5.2.1 Mechanical System Configuration

Experiments were conducted on a 5.4L 3 valve (2 intake valves and 1 exhaust valve) V8 engine head. As displayed in Figure 5.1, the cam and cam shaft were removed from the engine head. Three electro-pneumatic actuators were installed on the top of each valve to manage the intake and exhaust valve events. Micro-Epsilon^{TM} point range sensors were mounted under each valve to measure the valve displacements (see Figure 5.2).

To test the exhaust valve control system, a pressurized chamber was installed under the

test poppet valves, which imitates the in-cylinder pressure acting at the back of the exhaust valve. The pressure chamber is shown in Figure 5.3. It was pressurized throughout every experiment with the supply air pressure of $65psi$. The pressure inside drops immediately when the exhaust valve opens and builds up when it closes. The exhaust lift control experiments were performed at the engine speed as low as $600RPM$ to ensure that the chamber pressure recovers to as high as $60psi$ at every cycle. An optical window was built underneath the exhaust valve on the bottom of the chamber The exhaust valve laser sensor sends and receives laser beam through this optical window to detect the exhaust valve displacement. A pressure transducer was mounted at the side wall close to the exhaust valve head. The pressure transducer provided a relative reading whose maximum value was set to be $60psi$.

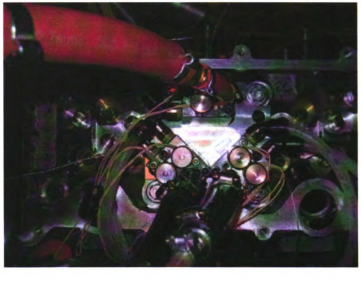

Figure 5.1. Top view of EPVA installed on the 5.4L 3V V8 engine head

5.2.2 Control System Hardware Configuration

A real time modular Opal-RT^{TM} control system was employed as a prototype controller for the EPVA bench tests. The system consists of:

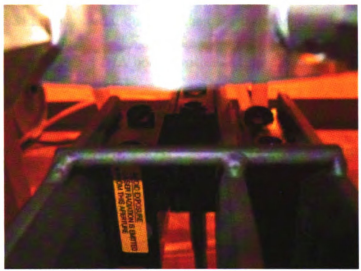

Figure 5.2. Point range laser valve displacement sensors

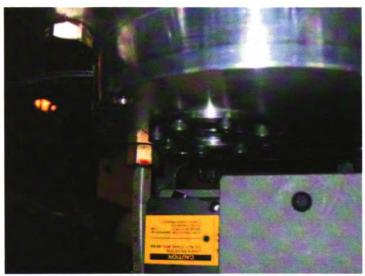

Figure 5.3. Pressure chamber under the valves

- Two 3.2GHz CPU's

- An IEEE 1934 fire wire serial bus with the data transfer rate at 400MHz per bit

- Two 16 channel A/D and D/A boards with less than 1 μs conversion rate

- One 16 channel digital I/O board at 50 ns sampling rate

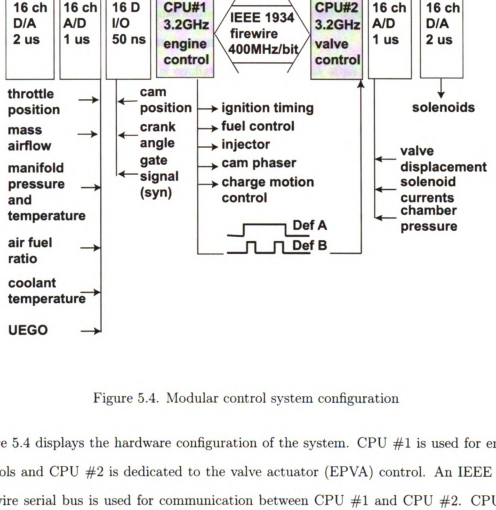

Figure 5.4. Modular control system configuration

Figure 5.4 displays the hardware configuration of the system. CPU #1 is used for engine controls and CPU #2 is dedicated to the valve actuator (EPVA) control. An IEEE 1934 fire wire serial bus is used for communication between CPU #1 and CPU #2. CPU #1 is configured to be updated every $1ms$ and execute the engine control every combustion cycle. This means that this CPU updates input and updates analog outputs every $1ms$,

but calculates the engine control parameters every engine combustion event. The digital outputs of CPU #1 are synchronized with the engine crank angle with one-third crank degree resolution. The crank angle calculation is completed within the digital I/O card of CPU #1 utilizing digital inputs from cam sensor, gate and crank signals from an encoder. The CPU #1 digital outputs are spark pulse, fuel injection pulse, charge motion control, and intake and exhaust valve timing pulses, especially the pulses $DefA$ and $DefB$ that synchronize the valve control between the engine and valve control system. The inputs of the 16 channel analog I/O board include ionization signal, pressure signal, throttle position, mass air flow rate, coolant temperature, manifold pressure and temperature, and air fuel ratio from universal exhaust gas oxygen (UEGO) sensor.

The valve control CPU #2 is configured to operate at $40\mu s$ sample rate, which is close to one crank angle degree at $4000RPM$. CPU #2 executes most of the valve control algorithms and generates the control signals for the pneumatic valve actuators. A 16 channel A/D board reads $DefA$ and $DefB$ pulse signals from CPU #1, valve lift signal from valve lift position sensors, solenoid current signals from their drive circuits, and supply air pressure signal. The solenoid control pulses and the exhaust valve pressure (which is needed to calculate the feedforward lift control inputs in simulation) are the output from a 16 channel D/A board.

A dSPACE^{TM} Autobox was utilized to run an engine simulator which provides the engine crank angle, gate signal, speed and other control parameters to both the engine controller and EPVA controller in real time application.

As displayed in Figure 5.5, the black box at left and right is the Opal-RT^{TM} control system for the valve actuation and engine control respectively. The white box sitting on the Opal-RT^{TM} system is the dSPACE^{TM} engine simulator.

5.2.3 Valve Actuator Driving Circuit

The intake valve solenoid driving circuit was designed to amplify the signal from the D/A controller outputs. Besides, it measures the solenoid current. The circuit is required to

Figure 5.5. Control hardware

have a short solenoid release time and fast switching capability with low noise. A single channel driving circuit drawing is shown in Figure 5.6. This circuit consists of a switching MOSFET (Metal-Oxide Semiconductor Field-Effect Transistor) and a NPN BJT (Bipolar Junction Transistors). The solenoid current is measured across a 0.5Ω resistor in serial with the source of the MOSFET. The exhaust valve solenoid driving circuit used the peak and hold scheme to minimize the solenoid electro-magnetic delays. The total solenoid delay including the electro-magnetic and mechanical delays was kept below $2ms$ using this circuit. The intake and exhaust driving circuit boxes are shown in Figure 5.5 too.

5.3 Experimental Evaluation on Intake Valve Lift Control System

5.3.1 Statistical analysis of Open-loop Valve Bench Data

Before the closed-loop valve lift and timing control bench tests were conducted, a statistical study focusing on the valve response repeatability was performed on test bench at both

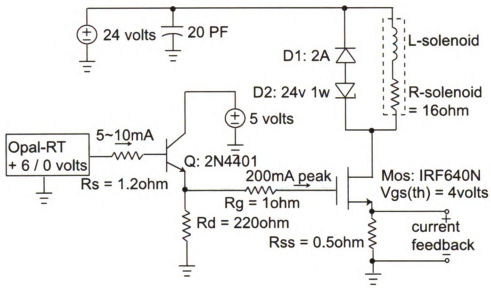

Figure 5.6. Solenoid driving circuit

high and low engine speeds. The test bench uses the EPVA actuators installed on a 5.4 liter 3-valve V8 engine head. Results of this study will be used to compare with those of the closed-loop valve lift test data to evaluate the steady state closed-loop lift control performance in Closed-loop Valve Lift Control Experimental Responses session. The valve repeatability has a great impact on the adaptive estimation and steady state response. The operational conditions that were used in the open-loop parameter identification in valve lift tracking tests were the same for both the low and high engine speeds. They were applied to collect these sample data. This means that the lag between the activation of solenoids 1 and 2 is set to be a constant value $\hat{\delta}_{1_i}$ used in the open-loop period in the lift tracking tests. The solenoid pulse period and pulse width, the air supply pressure and the oil pressure were held constant in both types of experiments.

Low engine speed open-loop valve bench data

Five bench tests were conducted using $80psi$ air supply pressure, $90psi$ oil pressure, $100ms$ solenoid period, which corresponds to the engine speed at $1200rpm$, with 25% pulse duty cycle and a lag of $5ms$ between the activation of two solenoids. The valve lift was targeted to be $9mm$ and there was a holding period on the valve lift profile under this experiment configuration (see Table 5.1). Two hundred-cycle data was collected from each experiment. The purpose of running these tests is to analyze statistical characteristics of the valve responses. Their histograms were plotted and the mean and standard deviation of responses were calculated. Taking data group #3 as an example, Figure 5.7 shows the histogram of data group #3, where the top plot is the valve lift histogram which reflects the valve lift repeatability and the bottom one is the histogram of the valve lift integral during the valve opening which indicates the repeatability of the engine charged air. For the valve lift diagram, the horizontal axis is the valve lift ranging from $8.4mm$ to $9.8mm$ and the vertical axis is the number of occurrence for each valve lift; and for the bottom diagram, the horizontal axis is the integral area and the vertical axis is the number of occurrence. The mean μ and the standard deviation σ were calculated, and the mean of integral area

of the valve lift was normalized to one. The 3σ value was used to indicate 95% occurrence.

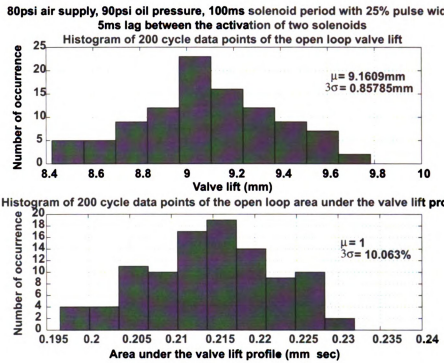

Figure 5.7. Histogram of open-loop valve lift bench test data points for $9mm$ target lift at $1200rpm$ in 200 cycles

The statistical analysis results of five data groups were summarized in Table 5.1. For the valve lift, group #5 has the largest valve lift mean at $9.55mmm$ and group #2 has the smallest mean at $8.83mmm$. The largest 3σ valve lift, $0.86mm$, is from data group #3. The smallest 3σ valve lift ($0.44mm$) was from data group #1. Regarding the analysis of the integral area of every cycle, the mean values were normalized to one, the 3σ values were calculated associated to normalized data and interpreted as percentage. Among the five data group, #3 has the largest 3σ value of 10.06%. Group #3 data provided the largest variation in both valve lift and the integral area. The corresponding histogram was displayed in Figure 5.7 and it will be compared with the closed-loop histogram of the

Table 5.1. Statistical study of open-loop valve actuation data with $9mm$ target lift at $1200rpm$

Engine configuration	Data group	y_{max} $= \mu \pm 3\sigma$ (mm)	y_{area} $= \mu \pm 3\sigma$
$80psi$ air supply pressure	#1	9.691 ± 0.43783	$1 \pm 4.639\%$
$90psi$ oil pressure	#2	8.8256 ± 0.80343	$1 \pm 10.87\%$
$100ms$ valve operation period	#3	9.1609 ± 0.85785	$1 \pm 10.063\%$
$25ms$ valve opening duration	#4	9.354 ± 0.5068	$1 \pm 6.7673\%$
$5ms$ lag of S2 (with holding)	#5	9.5495 ± 0.71124	$1 \pm 8.0833\%$

largest variation operated with a $9mm$ reference lift to show the valve lift repeatability improvement at the same operational condition due to closed-loop control.

High engine speed open-loop valve bench data

Similar to the low engine speed case, five bench tests were conducted using $80psi$ air supply pressure, $90psi$ oil pressure, $24ms$ solenoid period (which corresponds to the engine speed at $5000rpm$) with a 25% pulse duty cycle and a lag of $5ms$ between the activation of two solenoids. There is no holding pattern displayed in the valve lift profile when the engine is operated at $5000rpm$. In this case the valve returns before the hydraulic latch is engaged to hold the valve open (recall the discussion in the System Dynamics section). The desired valve lift was also set to be $9mm$ for this experiment (see Table 5.2). Two hundred-cycle data was collected for each experiment. The mean μ and the standard deviation σ were calculated. The mean of the valve lift integral was normalized to one as well. Again, the 3σ values were used to cover 95% sample data points.

Table 5.2 summarizes the statistical analysis results of five data groups. For the valve lift, data group #1 has the largest mean valve lift at $9.14mm$ and group #5 has the smallest mean valve lift at $8.59mm$. The largest 3σ valve lift was from data group #4 at $0.63mm$ which is less than the largest 3σ valve lift ($0.86mm$) at low engine speed ($1200rpm$). The smallest valve lift 3σ value of $0.17mm$ was found from data group #2. It is less than the largest valve lift 3σ value ($0.44mm$) from the $1200rpm$ tests. This indicates that the valve lift repeatability improves at high engine speed. For the integral area, data group #4 has the largest 3σ value of 11.7%. The group #4 test results show the largest variation in both

Table 5.2. Statistical study of open-loop valve actuation data with $9mm$ target lift at $5000rpm$

Engine configuration	Data group	y_{max} $= \mu \pm 3\sigma$ (mm)	y_{area} $= \mu \pm 3\sigma$
$80psi$ air supply pressure	#1	9.1424 ± 0.26838	$1 \pm 6.1233\%$
$90psi$ oil pressure	#2	9.1281 ± 0.17305	$1 \pm 4.4528\%$
$24ms$ valve operation period	#3	9.0284 ± 0.39827	$1 \pm 8.339\%$
$6ms$ valve opening duration	#4	8.8649 ± 0.6346	$1 \pm 11.7\%$
$5ms$ lag of S2 (without holding)	#5	8.5943 ± 0.42403	$1 \pm 5.545\%$

valve lift and the integral area of the valve lift. Their histograms are shown in Figure 5.8, where the top histogram is for the valve lift and the bottom one is for the integral area. For the top diagram, the horizontal axis is the valve lift ranging from $8.9mm$ to $9.5mm$ and the vertical axis is the number of occurrence of each valve lift. For the bottom diagram, the horizontal axis is the integral area and the vertical axis is the number of occurrence of integral area. This histogram will be used to compare the corresponding closed-loop test data later.

Open-loop low valve lift bench data

The EPVA is capable of providing a valve lift as low as $3mm$. This subsection studies statistical property at low valve lift to determine if the low valve lift operation mode is acceptable for engine control. Since the valve lift repeatability improves as engine speed increases (from the previous analysis), we are going to study the low valve lift operation only at low engine speed ($1200rpm$). Five bench tests were conducted using the same experimental setup as high lift case at $1200rpm$ engine speed except the lag between the activation of two solenoids was reduced to $3.4ms$ to obtain the targeted valve lift at $3mm$. The statistical results were shown in Table 5.3. The mean valve lift varies from $2.68mm$ to $3.51mm$. The largest valve lift 3σ value is $2.5mm$ from data group #3 and the 3σ value is not less than $0.8mm$ among the rest of the data groups. Consequently, data group #3 has a 3σ integral area value as high as 73.196%. Although the actuator is capable of providing a lift as low as $3mm$, its repeatability is not good enough to deliver a stable air flow when engine is operated at light load conditions. For this engine control project, the

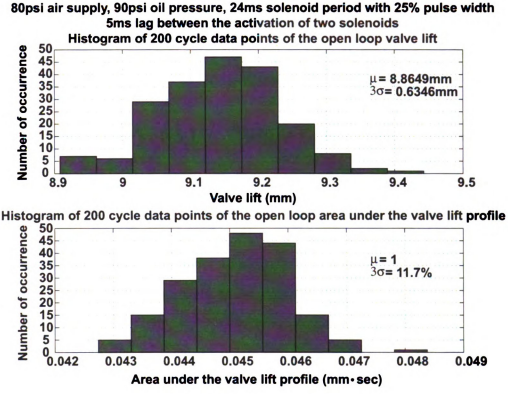

Figure 5.8. Histogram of open-loop valve lift bench test data points for $9mm$ target lift at $5000rpm$ in 200 cycles

Table 5.3. Statistical study of open-loop valve actuation data with $3mm$ target lift at $1200rpm$

Engine configuration	Data group	y_{max} $= \mu \pm 3\sigma$ (mm)	y_{area} $= \mu \pm 3\sigma$
$80psi$ air supply pressure	#1	2.6751 ± 0.89005	$1 \pm 15.71\%$
$90psi$ oil pressure	#2	3.3175 ± 0.79791	$1 \pm 18.745\%$
$100ms$ valve operation period	#3	3.3581 ± 2.4954	$1 \pm 73.196\%$
$25ms$ valve opening duration	#4	3.5056 ± 0.94671	$1 \pm 18.803\%$
$3.4ms$ lag of S2 (with holding)	#5	3.1683 ± 1.432	$1 \pm 41.194\%$

valve lift operational range is to be limited between $5mm$ and $11mm$ to ensure the desired repeatability. When the required valve lift is below $5mm$ at light load condition, a flap valve or a throttle would be used to reduce the intake air flow.

5.3.2 Closed-loop Valve Lift Control Experimental Responses

The closed-loop valve control algorithms were verified on the valve test bench utilizing the same engine head as open-loop cases. The experimental responses at both low and high engine speeds are presented in this section. Since both closed-loop valve opening and closing timing controls are similar to the valve lift control case, the results are not presented. Air and oil supply pressure for all tests are $80psi$ and $90psi$ respectively. The experimental parameter is $100ms$ solenoid period with $25ms$ solenoid active duration (25% duty cycle) corresponding to $1200rpm$ in the low engine speed tests and $24ms$ solenoid period with $6ms$ solenoid active duration (25% duty cycle) corresponding to $5000rpm$ in the high engine speed tests. The initial lag between the activation of solenoids 1 and 2 during the open-loop parameter identification period was $5ms$ at both low and high speed tests.

Experimental results at low engine speed

2500 cycles of valve responses were recorded with various reference valve lift points. The estimated parameter was converged in the first 25 cycles (or $2.5ms$). The reference valve lift varies every 500 cycles from $9mm$ to $6mm$, from $6mm$ to $10mm$, from $10mm$ to $7mm$, and from $7mm$ to $9mm$. Their steady state responses are presented in Figures 5.11, 5.13,

5.15 and 5.17. On the top diagram of every figure, the black line is the reference valve lift, and the grey line is the actual valve lift. The bottom diagram shows the lift error between the reference and the actual valve lifts. They start at 50 cycles before the reference valve lift step change and end right before the next reference valve lift change. The top diagrams of Figures 5.12, 5.14, 5.16)and 5.18)display the nominal input $\hat{\delta}_{1_o}$ (solid line) calculated based on the estimated C_{f_1} against the controlled input $\hat{\delta_1}$ (dotted line) which is the output of the PI feedback controller. Their enlarged transient responses are presented in the bottom diagrams, where the dark lines are the reference valve lift and the grey lines are the true valve displacement.

Open-loop parameter identification valve responses

Figure 5.9 enlarges the first 80 cycle valve lift tracking responses. C_{f_1} identification error (the bottom diagram) converges to a set tolerance in about 25 cycles. It can be observed from the top diagram that the system switched from the open-loop to closed-loop control at the $65th$ cycle where the lift error jumps from zero to $0.7mm$ (the dark grey line in the top diagram). This indicates that the closed-loop controller is engaged.

Steady state responses of valve lift tracking

During the steady state operations, the valve lift tracks the reference valve lift and oscillates around the reference values. The responses show good repeatability at high valve lifts. The maximum absolute valve lift error was bounded by $0.4mm$ at $10mm$ lift and $0.5mm$ at $9mm$ lift. The repeatability is relatively lower at low lift, however, the valve lift error falls mostly in the region of $\pm 0.5mm$ at $6mm$ and $7mm$ lift. This is partially due to the fact that the pneumatic valve actuator has a higher sensitivity at the low valve lift, which results in a high steady state lift error. The maximum absolute steady state error at these four set points are listed in Table 5.4.

The statistical performance of the valve lift responses with the closed-loop controller is also important to study. The statistical characteristics of the open-loop valve lift are

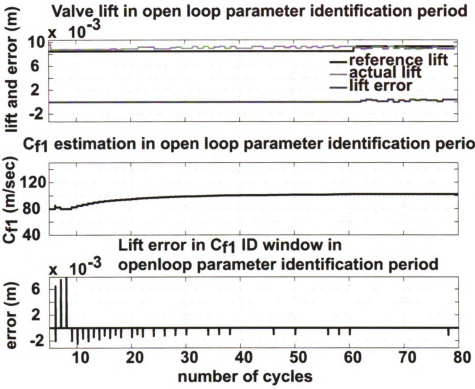

Figure 5.9. Open-loop parameter C_{f_1} identification at $1200rpm$

Table 5.4. Maximum SS absolute valve lift error ($1200rpm$)

Reference valve lifts (mm)	6	7	9	10
Max. absolute lift error (mm)	0.75	1.3	0.5	0.4

Table 5.5. Statistical study of closed-loop valve actuation data at $1200rpm$

Engine configuration	Data group	y_{max} $= \mu \pm 3\sigma$ (mm)	y_{area} $= \mu \pm 3\sigma$
$80psi$ air supply pressure	#1	9.2358 ± 0.454	$1 \pm 5.4534\%$
$90psi$ oil pressure	#2	9.2495 ± 0.3478	$1 \pm 2.9224\%$
$100ms$ valve operation period	#3	9.0984 ± 0.38628	$1 \pm 4.8195\%$
$25ms$ valve opening duration	#4	9.0549 ± 0.44419	$1 \pm 5.1670\%$
$9mm$ reference valve lift (with holding)	#5	9.1015 ± 0.41092	$1 \pm 4.1833\%$

analyzed in the earlier section of Statistical Analysis of Open-Loop Valve Bench Data. The results of the valve lift statistical study shown in both Figure 5.7)and Table 5.1 provide the worst lift 3σ value at $0.86mm$ and the worst integral area 3σ value at 10.87% with the valve lift at $9mm$ using five test data groups. The same statistical analysis is conducted for the closed-loop lift control. Five 200 cycle steady state valve lift responses at $9mm$ were used to calculate the means and standard deviations of the valve lift and its integrated area. These results are compared with the open-loop results. The diagrams displayed in Figure 5.10 depict the histograms of the lift and integral area of the valve lift profile. They are obtained from the data group with the largest variations among all five data groups (see group #1 in Table 5.5). Note that the axes ranges and the bin width of the valve lift (top) and integral area (bottom) histograms in Figure 5.10 are the same as those in Figure 5.7 for an easy comparison.

The five sets of means and 3σ values of valve lift and integral area were summarized in Table 5.5. The worst 3σ value of the valve lift reduced from the open-loop $0.86mm$ to the closed loop $0.45mm$, and the worst integral area 3σ value reduced from 10.87% to 5.45% (see both Table 5.5 and Table 5.1). In other words, the worst case 3σ values of both valve lift and integral area were reduced by about 45%. This indicates that the closed-loop valve lift control reduces the valve lift variation, and hence, improves its lift repeatability.

Transient responses of valve lift tracking

The feedforward nominal input $\hat{\delta}_{1_o}$ remains steady due to the fact that the parameter identification convergence is preserved in the closed-loop lift control operation. It takes

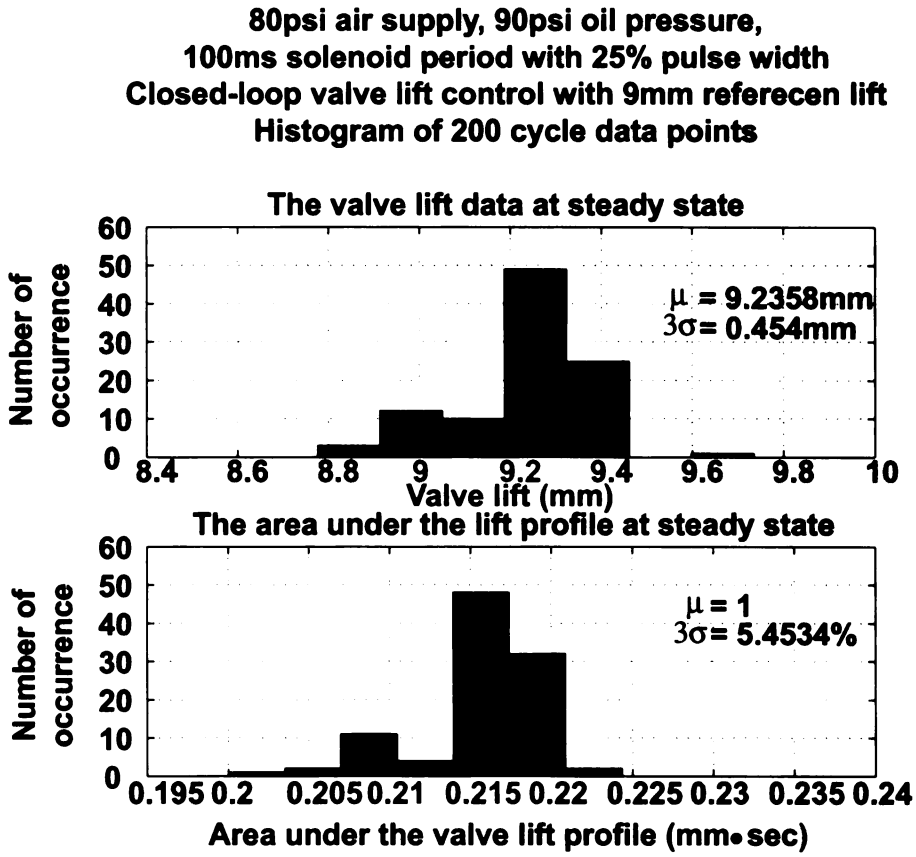

Figure 5.10. Histogram of closed-loop valve lift control test data points for $9mm$ reference lift at $1200rpm$ in 200 cycles

about one cycle for the valve to reach the reference valve lift with less than $0.5mm$ of lift error. This is critical for transient air charge control. The controlled input $\hat{\delta}_1$ is close to the nominal input $\hat{\delta}_{1_o}$ which is sufficiently accurate to bring the valve lift close to the reference valve lift in the first cycle. In all four cases, the actual valve lift is within $0.5mm$ lift error region of the reference lift in one cycle.

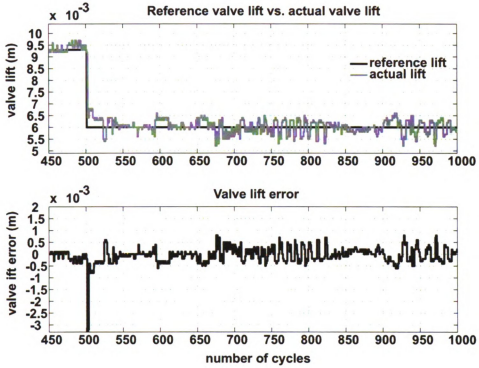

Figure 5.11. Steady state valve lift tracking responses from $9mm$ to $6mm$ lift at $1200rpm$

5.3.3 Experimental Results at High Engine Speed

The high speed closed-loop valve lift tracking results are presented and discussed in this subsection. Similar to the low speed case, 2500 cycles of valve responses were collected with multiple reference valve lift set points the same as these in the low engine speed case. The entire 2500 cycle lift tracking responses and two enlarged transient responses are shown in

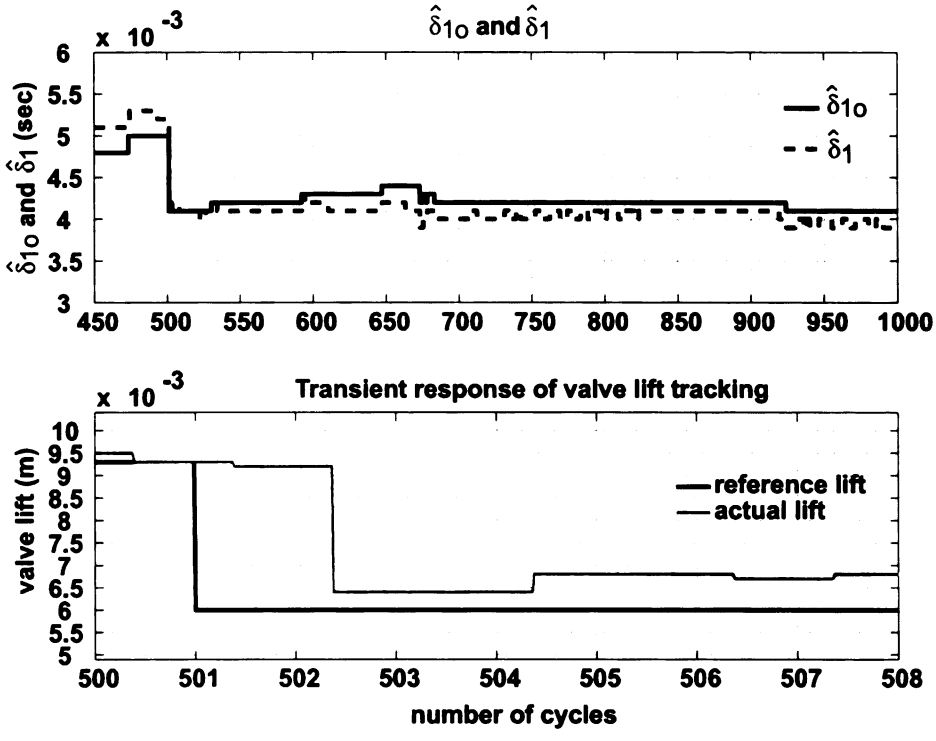

Figure 5.12. Controlled input and transient valve lift tracking responses from $9mm$ to $6mm$ lift at $1200rpm$

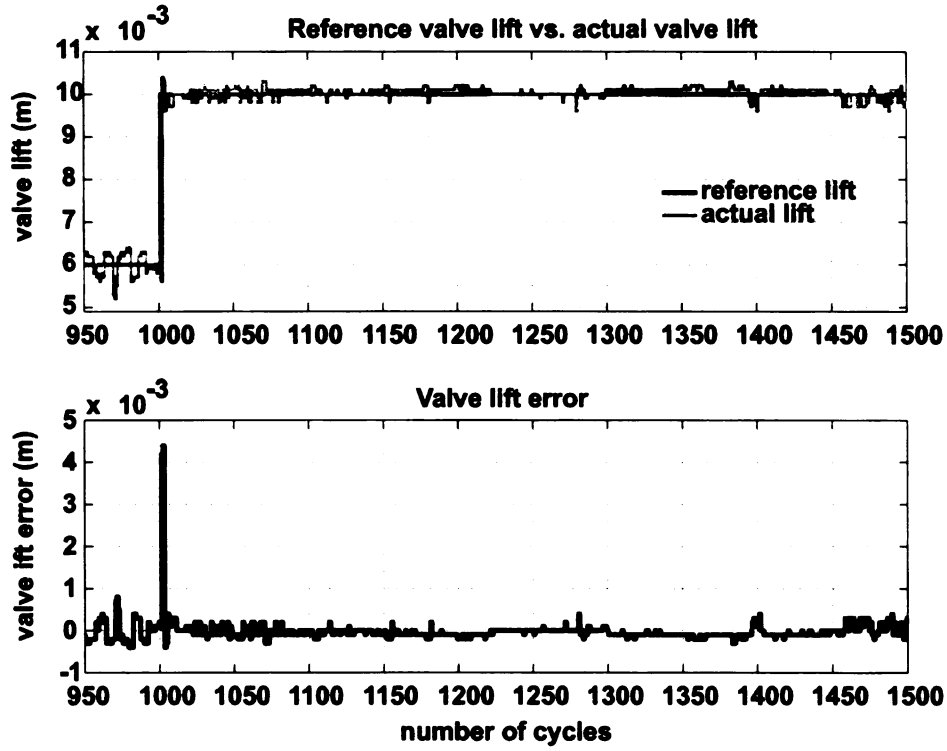

Figure 5.13. Steady state valve lift tracking responses from $6mm$ to $10mm$ lift at $1200rpm$

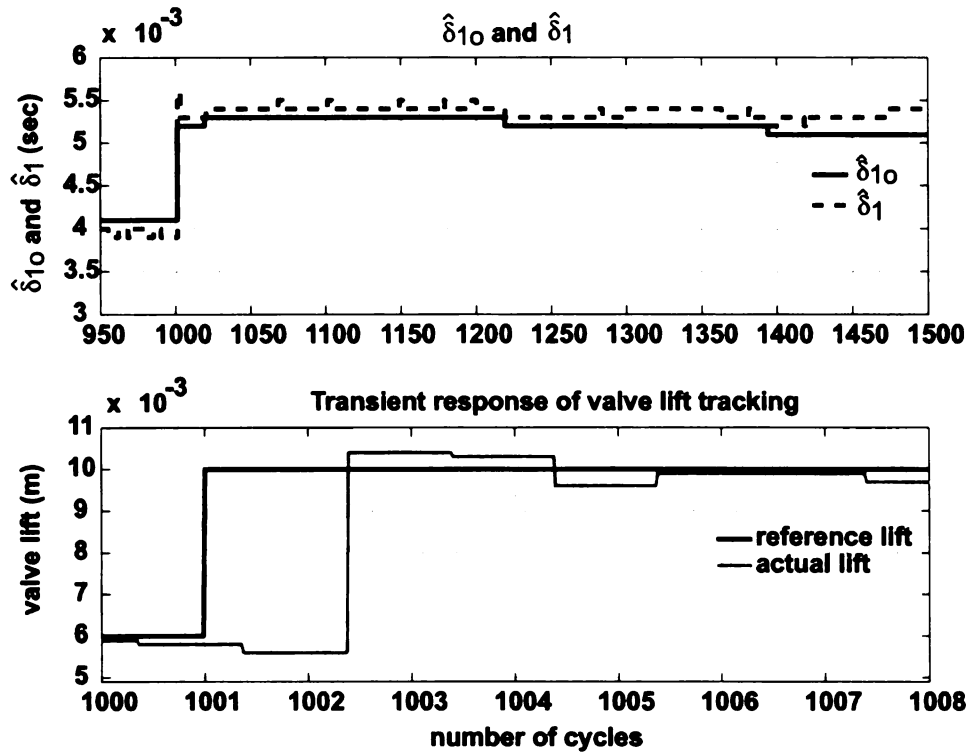

Figure 5.14. Controlled input and transient valve lift tracking responses from $6mm$ to $10mm$ lift at $1200rpm$

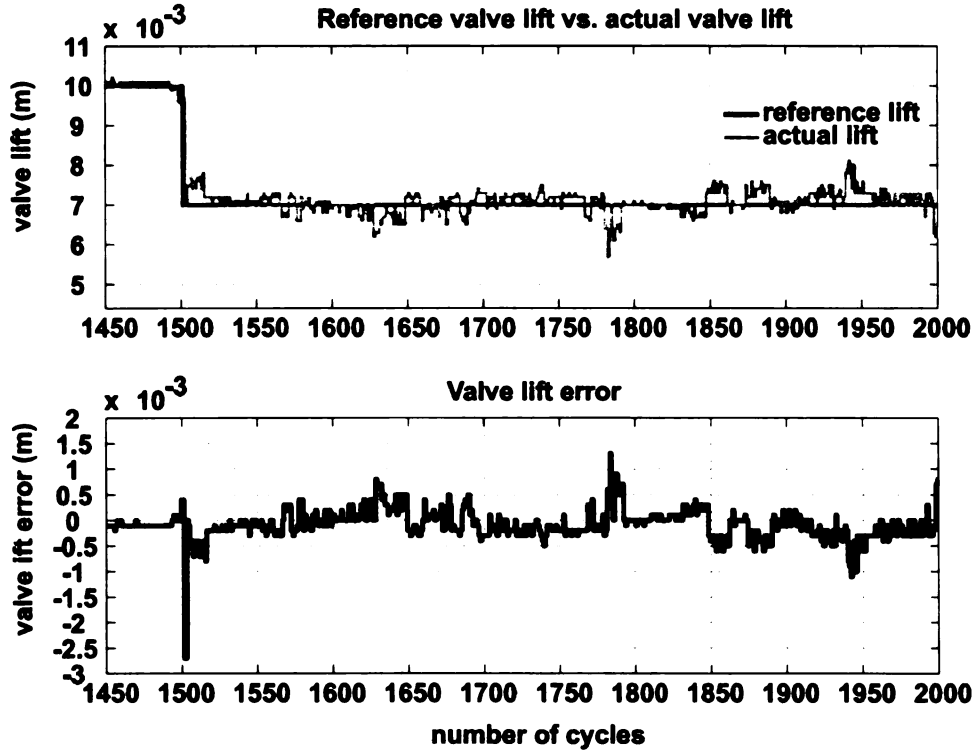

Figure 5.15. Steady state valve lift tracking responses from $10mm$ to $7mm$ lift at $1200rpm$

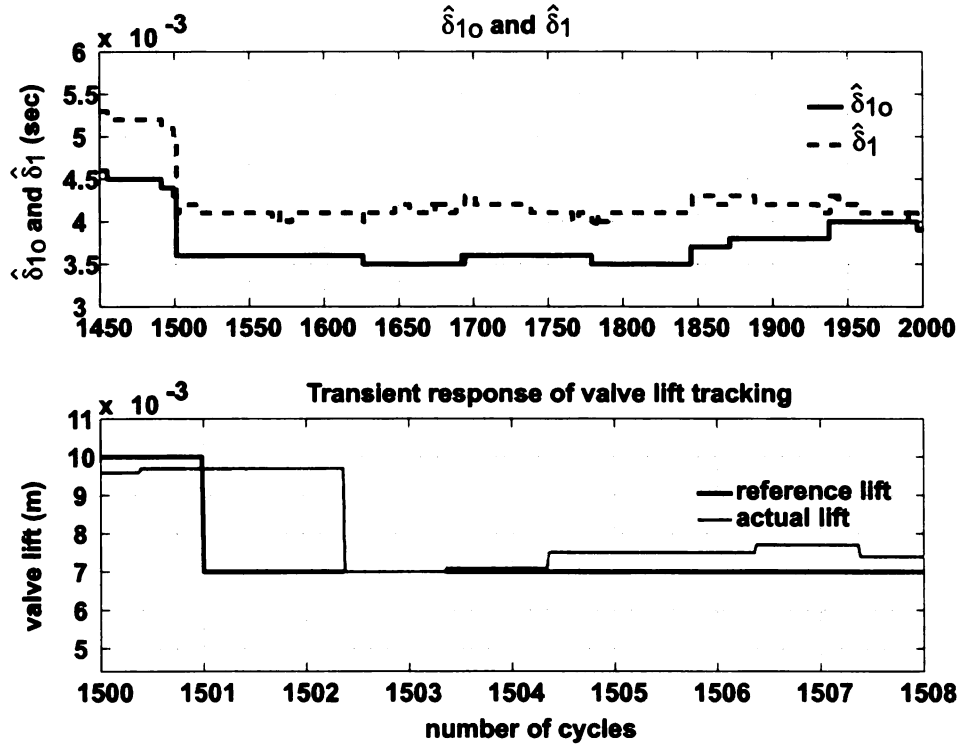

Figure 5.16. Controlled input and transient valve lift tracking responses from $10mm$ to $7mm$ lift at $1200rpm$

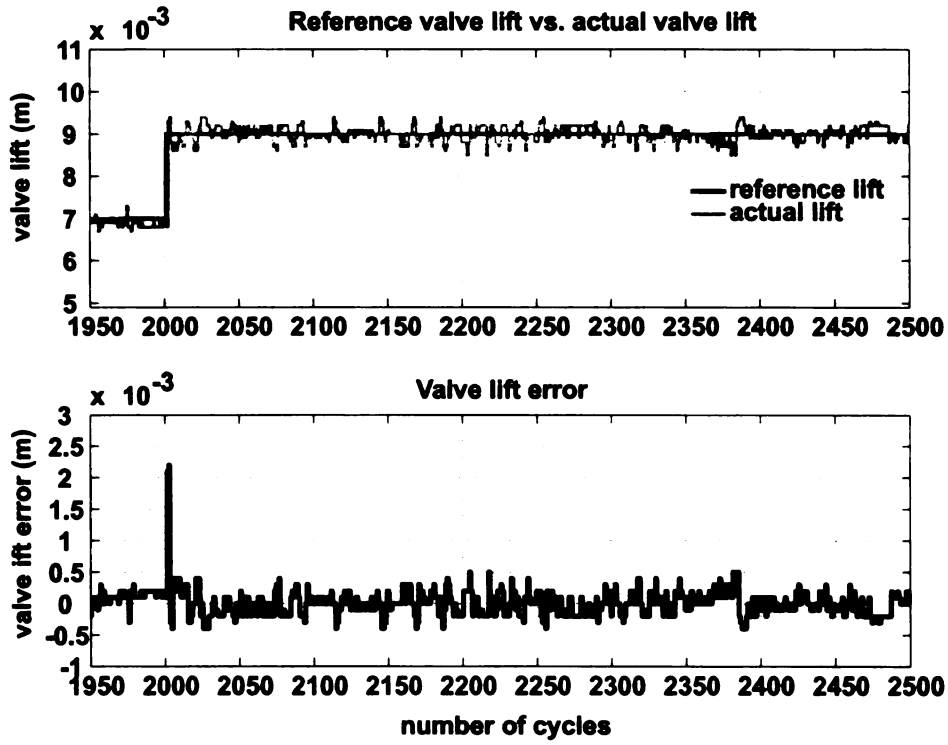

Figure 5.17. Steady state valve lift tracking responses from $7mm$ to $9mm$ lift at $1200rpm$

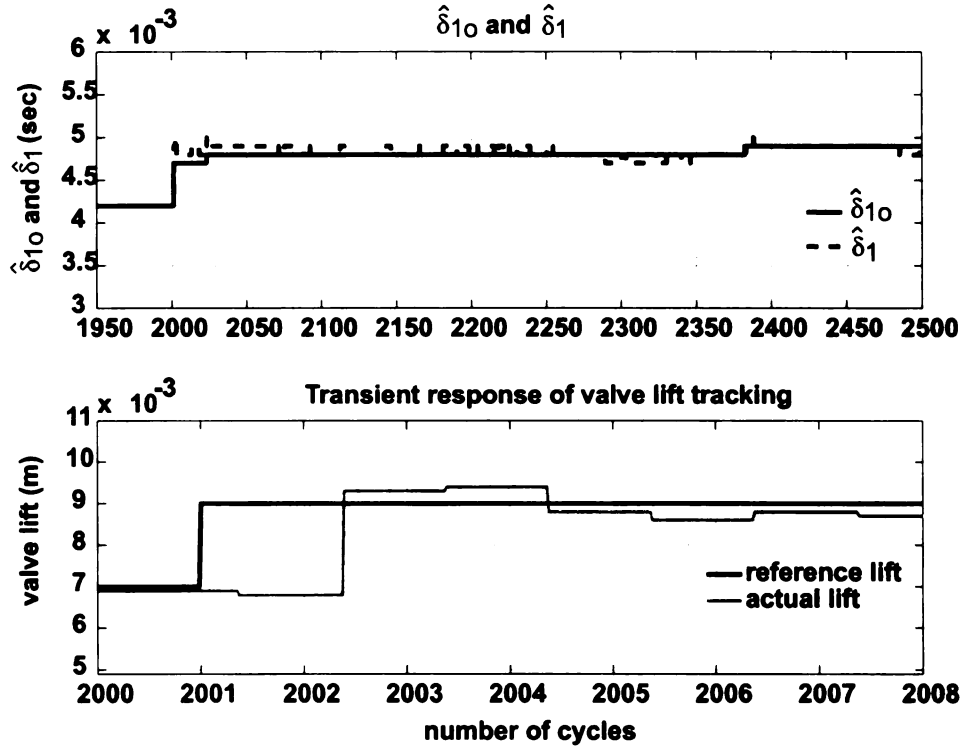

Figure 5.18. Controlled input and transient valve lift tracking responses from $7mm$ to $9mm$ lift at $1200rpm$

Figure 5.19. The top diagram displays the reference valve lift in black line, the actual valve lift in light grey and the lift error in dark grey; the middle diagram shows the transient response at the reference lift change from $10mm$ to $6mm$, and the bottom diagram shows the transient response at the reference lift change from $7mm$ to $9mm$. All the horizontal axes are the number of engine cycles. The vertical axes are the valve lifts in m. The estimated parameter was converged within 100 cycles (or $2.4ms$) which was indicated by a small jump on the reference valve lift on the top diagram. In most of cases, it takes about one cycle for the valve to reach the reference valve lift with less than $0.5mm$ of lift error. However, when the reference lift has a relatively large drop, the actual lift would have a big undershoot during the transient response (see the transient response from $10mm$ to $7mm$ in the top diagram of Figure 5.19). The undershoot is about $1.9mm$ in this case for the first step, and $0.5mm$ after the first step. This is partially due to the supply air pressure variations of different lift conditions at high engine speed. The high air flow requirement at high valve lift operational conditions reduces the actual supply air pressure close to the actuator, and supply air pressure increases as the valve lift reduces. When the valve is transient from high lift to low lift, the supply air pressure increases gradually, causing larger undershoot since the feedforward control assumes higher supply air pressure than actual one. This problem can be resolved by increasing the volume of the planum at the supply air manifold of the actuator cylinder.

The maximum absolute steady state error at these four set points are listed in Table 5.6. The steady state lift errors are less than $0.8mm$ at high valve lift and less than $1.1mm$ at low lift. The results of the valve lift statistical study at $5000rpm$ engine speed shown in

Table 5.6. Maximum SS absolute valve lift error ($5000rpm$)

Reference valve lifts (mm)	6	7	9	10
Max. absolute lift error (mm)	0.8	1.1	0.8	0.7

both Figure 5.8 and Table 5.2 provide the worst lift 3σ value at $0.63mm$ and the worst integral area 3σ value at 11.7% with the target lift at $9mm$ using five test data groups.

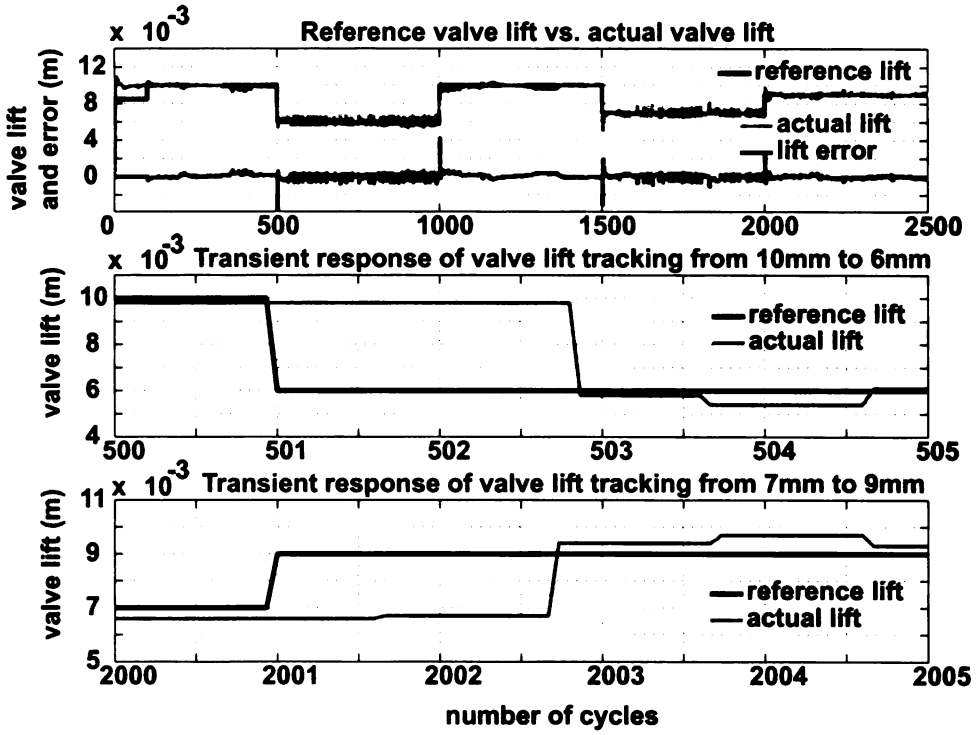

Figure 5.19. Valve lift tracking responses with multiple reference lift at $5000rpm$

Table 5.7. Statistical study of closed-loop valve actuation data at $5000rpm$

Engine configuration	Data group	y_{max} $= \mu \pm 3\sigma$ (mm)	y_{area} $= \mu \pm 3\sigma$
$80psi$ air supply pressure	#1	9.0439 ± 0.45208	$1 \pm 9.4497\%$
$90psi$ oil pressure	#2	9.0832 ± 0.28338	$1 \pm 5.1215\%$
$100ms$ valve operation period	#3	9.1641 ± 0.313	$1 \pm 7.4794\%$
$25ms$ valve opening duration	#4	8.9544 ± 0.24869	$1 \pm 6.69\%$
$9mm$ reference valve lift (without holding)	#5	9.091 ± 0.37342	$1 \pm 8.2682\%$

The same statistical analysis is performed for the closed-loop lift control. Five 200 cycle steady state valve responses at $9mm$ reference lift were used to calculate the means and standard deviations of the valve lift and its integral area. These results are compared with the open-loop results. The diagrams displayed in Figure 5.20 depict the histograms of the valve lift and integral area with the largest variations (data group #1 in Table 5.7). For easy comparison, the axes ranges and the bin width of the valve lift (top) and integral area (bottom) histograms in Figure 5.20 are the same as those in Figure 5.8. The five sets of means and 3σ values of valve lift and integral area were summarized in Table 5.7. The worst 3σ value of the valve lift reduced from the open-loop $0.63mm$ to the closed-loop $0.45mm$ which was reduced by about 29%. The worst integral area 3σ value reduced from 11.7% to 9.45% which was reduced by about 19% (see both Table 5.7 and Table 5.2). The low engine speed closed-loop lift control data showed a reduction of about 45% on both the 3σ values of the valve lift and integral area in their worst case. The reduction on the cycle to cycle lift variation at $5000rpm$ seems lower than that at $1200rpm$. We believe that low improvement at high engine speed is mainly due to the fixed control sample rate which reduces the valve control resolution as engine speed increases.

5.3.4 Concluding Remarks On Intake Valve Lift Control System

In chapter 2, A nonlinear mathematical model called the level one model was developed for the electro-pneumatic valve actuator based on Newton's law, mass conservation and thermodynamic principles. A control oriented model, called level two model, was established using the physics based nonlinear model for model reference parameter identification

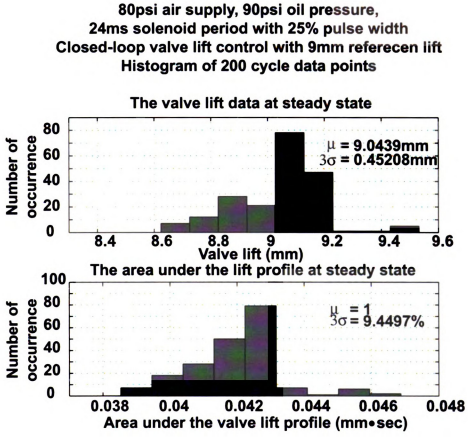

Figure 5.20. Histogram of closed-loop valve lift control test data points for $9mm$ reference lift at $5000rpm$ in 200 cycles

in chapter 3. This level two model reduces computational throughput and enables real time implementation. A model reference adaptive scheme was employed to identify two key nonlinear system parameters. The identified parameters are then used to construct the feedforward control as part of the closed-loop valve PI controller. The closed-loop valve lift tracking, and valve opening and closing timing control strategies were developed. In chapter 5, the lift control algorithm was validated on an electro-pneumatic valve actuator test bench. The test data covers multiple reference lift points at both $1200rpm$ and $5000rpm$ engine speeds for both steady state and transient operations. The experiment results showed that the actual valve lift reached the reference lift within $0.5mm$ of lift error in one cycle at $1200rpm$ and in two cycles at $5000rpm$. The maximum steady state lift errors are less than $0.4mm$ at high valve lift and less than $1.3mm$ at low valve lift. Furthermore, the closed-loop valve lift control improved valve lift repeatability with more than 30% reduction of standard deviation over the open-loop control.

5.4 Experimental Evaluation on Exhaust Valve Lift Control System

5.4.1 Experimental Results of Closed-Loop Exhaust Valve Lift Tracking

Finally, Figure 5.21 to 5.24 present the closed-loop lift tracking experimental results with the feedforward control. The purpose of the experiments were to evaluate the system feedforward input calculation. The PI gains were kept relatively low in the experiments to allow the feedforward response to be dominant. 150 cycles of valve responses were recorded with sequences assembled at three reference lift set points in Figure 5.21. The reference valve lift varies every 50 cycles from $8mm$ to $6mm$, $6mm$ to $10mm$, and $10mm$ to $8mm$. The complete sequences of lift tracking responses are presented in Figures (5.21). The responses at every set point were enlarged through Figure 5.22 to 5.24 to illustrate their

transient and steady state performance. On the top diagram of every figure, the black line is the reference valve lift, and the grey line is the actual valve lift. The bottom diagram shows the lift error between the reference and the actual valve lifts. Figure 5.22 shows that the exhaust valve follows the reference lift of $6mm$ in two engine cycles with the lift error less than $0.7mm$. Figure 5.23 and 5.24 show that the exhaust valve tracks the reference lift of $10mm$ and $8mm$ in one engine cycle with the lift error less than $0.7mm$. The enlarged responses display that the absolute steady state lift tracking error of all three set points is below $1mm$. Here, an accurate feedforward controlled input ensures a fast transient repones. The valve responses at low lift is more sensitive to the error in the calculated feedforward controlled input, which has relatively greater fraction in the entire input (the lag between the activation of solenoid #1 and #2). A slight error in the feedforward input calculation due to the model uncertainty, measurement inaccuracy or numerical error leads to a significant deviation of the actual valve lift from its desired lift in transition. Therefore, the valve at low reference lift exhibits a slower transient response than that at high reference lift.

5.4.2 Concluding Remarks On Exhaust Valve Lift Control System

A mathematical exhaust valve actuator model and an in-cylinder pressure model have been developed for a model based predictive lift control for the exhaust valve. The exhaust valve model was approximated by a partially linearized second order spring-mass-damper system. The in-cylinder pressure was modeled during the exhaust valve opening stage. This model was integrated with the exhaust valve actuator model for control development. The thermodynamics data used in this model was obtained with the WAVE^{TM} simulation which was calibrated using experimental in-cylinder pressure data. The in-cylinder pressure model was validated using experimental data and demonstrates satisfactory model accuracy.

A model based predictive control strategy was developed for feedforward control. This

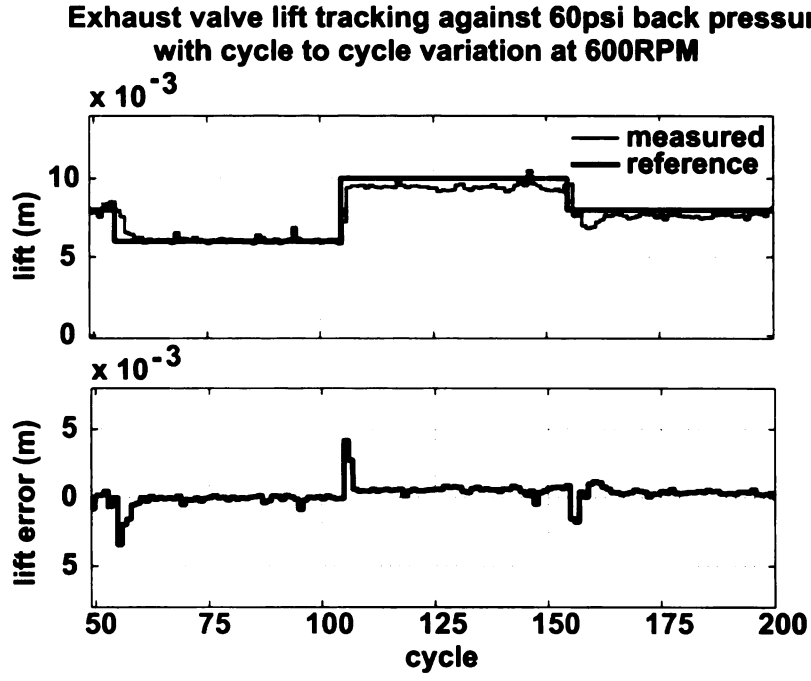

Figure 5.21. Experimental results of closed-loop exhaust valve lift tracking control system with three set points

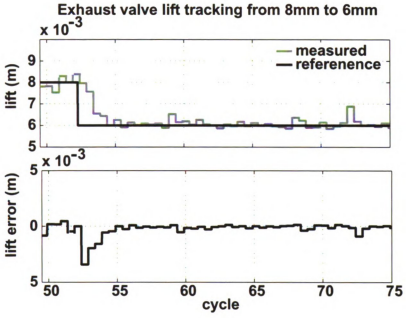

Figure 5.22. Enlarged experimental results of closed-loop exhaust valve lift tracking from set point of $8mm$ to $6mm$

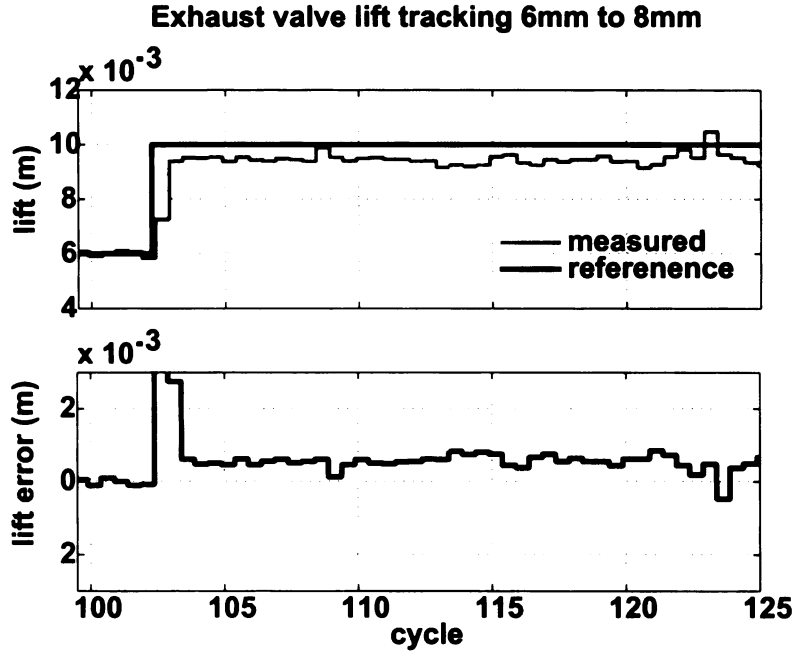

Figure 5.23. Enlarged experimental results of closed-loop exhaust valve lift tracking from set point of $6mm$ to $10mm$

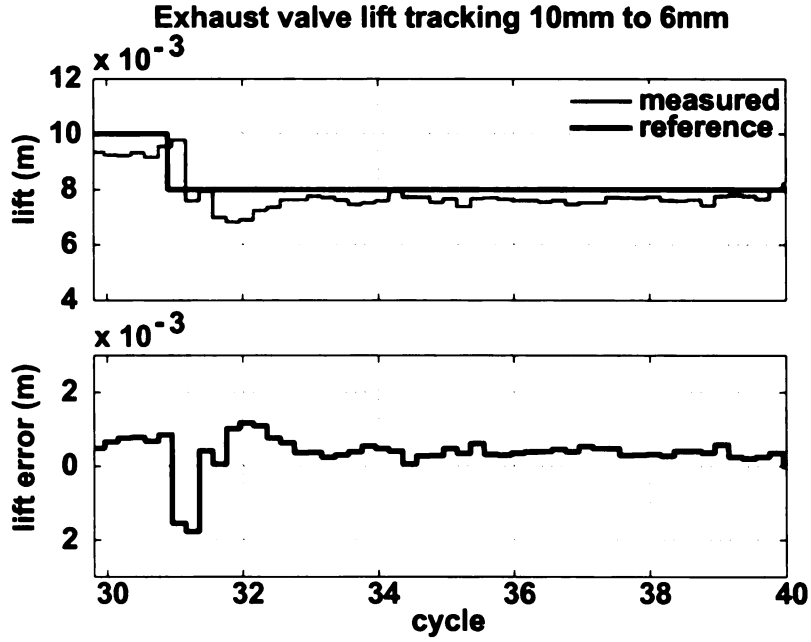

Figure 5.24. Enlarged experimental results of closed-loop exhaust valve lift tracking from set point of $10mm$ to $8mm$

strategy contains three segments; peak displacement calculation, model based initial condition prediction and Kalman state estimation. To reduce real time computational throughput, simulations were carried out to calculate the feedforward lift control inputs through the developed model based predictive control strategy for given reference lifts. In real time application, the acquired feedforward input combined with the feed back lift compensation generated from a proportional and integral controller forms the closed-loop lift control signal to accomplish the exhaust valve lift tracking. The exhaust valve model was identified and the measured exhaust valve back pressure was piecewisely linearized to obtain parameters required for the feedforward input calculation. Both of them were employed in the simulation. Experiments were conducted on a 5.4L 3 valve V8 engine head at $600RPM$ engine speed to evaluate the closed-loop lift control system. A pressurized chamber was installed under the test poppet valves, which imitates the in-cylinder pressure acting at the back of the exhaust valve. The experimental results containing three lift set points demonstrated that the steady state valve lift error is below $1mm$. The exhaust valve tracks the reference lift in a single engine cycle at high reference lift and two engine cycles at low reference lift having a lift error less than $0.7mm$.

BIBLIOGRAPHY

[1] Atsushi Umemoto Yasuo Shimizu Chihaya Sugimoto, Hisao Sakai and Hidetaka Ozawa. Study on variable valve timing system using electromagnetic mechanism. *SAE International 2004-01-1869*, April 2004.

[2] H. S. Hilbert D. L. Boggs and M. M. Schechter. The otto-atkinson cycle engine-fuel economy and emissions results and hardware design. *SAE 950089*, 1995.

[3] James E.Bobrow and Brian W.McDonell. Modeling and control of a variable valve timing engine. *Proceedings of the American Control Conference*, June 2000.

[4] F.Pischinger and Rassem P.Kreuter. Electromagnetically operating actuator. *U.S. Patent number 4,455,543*, June 1984.

[5] Klaus Wichart Hans Peter Lenz and Dusan Gruden. Variable valve timing - a possibility to control engine load without throttle. *SAE 880388*, 1988.

[6] B.Geringer H.P.Lenz and G.Smetana. Initial test results of an electro-hydraulic variable valve actuation system on a firing engine. *SAE 890678*, 1989.

[7] H.Kazerooni J.M.Tressler, T.Clement and M.Lim. Dynamic behavior of pneumatic systems for lower extremity extenders. *Proceedings of the 2002 IEEE International Conference on Robotics & Automation*, pages 416–425, May 2002.

[8] R.J.Pearson G.Pitcher J.W.G.Turner, M.D.Bassett and K.J.Douglas. New operating strategies afforded by fully variable valve trains. *SAE International 2004-01-1386*, April 2004.

[9] Bjorn Wittenmark Karl Johan Astrom. *Adaptive control.* Wesley Publishing Company, Boston, MA, 2 edition, 1995.

[10] Tim Lancefield. The influence of variable valve actuation on the part load fuel economy of a modern light-duty diesel engine. *SAE 2003-01-0028*, 2003.

[11] Bruno Lequesne Mark A.Theobald and Rassem R.Henry. Control of engine load via electromagnetic operating actuator. *SAE 940816*, 1994.

[12] Mohammad Haghgooie Thomas W. Megli Nate R. Trask, Mazen Hammoud and Wen Dai. Optimization techniques and results for the operating modes of a camless engine. *SAE 2003-01-0033*, 2003.

[13] Marcel Ginu Popa Nichulae Negurescu, Constantin Pana and Alexandru Racovitza. Variable valve - control systems for spark ignition engine. *SAE 2001-01-0671*, 2001.

[14] John P.Watson and Russell J.Wakeman. Simulation of a pneumatic valve actuation system for internal combustion engine. *SAE International 2005-01-0771*, April 2005.

[15] FWilliam T.Thomson. *Theory of vibration with applications.* Prentice Hall, Upper Saddle River, New Jersey, 5 edition, 1998.

[16] Edmond Richer Washington, D.C. and Yildirim Hurmuzlu. A high performance pneumatic force actuator system: Part i- nonlinear mathematical mode. *Transactions of the ASME*, 122:416–425, September 2000.

[17] W.E.Richeson and F.L.Erickson. Pneumatic actuator with permanent magnet control valve latching. *U. S. Patent number 4,852,528*, August 1989.

[18] Junichi Takanashi Takashi Kakinuma Takazou Hakozaki Yasuhiro Urata, Moriyoshi Awasaka and Atushi Umemoto. A study of gasoline-fuelled hcci engine equipped with an electromagnetic valve train. *SAE 2004-01-1898*, 2004.